

# Determination of the $^{24}\text{Mg}(p, \gamma)^{25}\text{Al}$ Reaction Rate at Low Stellar Temperatures

by

Denise Catherine Powell

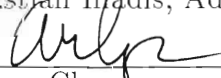
A dissertation submitted to the faculty of the University of North Carolina at Chapel Hill in partial fulfillment of the requirements for the degree of Doctor of Philosophy in the Department of Physics & Astronomy.

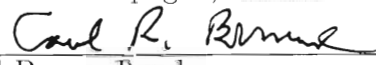
Chapel Hill

1999

Approved:

  
\_\_\_\_\_  
Christian Iliadis, Advisor

  
\_\_\_\_\_  
Arthur Champagne, Reader

  
\_\_\_\_\_  
Carl Brune, Reader



## ABSTRACT

DENISE CATHERINE POWELL: Determination of the  $^{24}\text{Mg}(p, \gamma)^{25}\text{Al}$  Reaction Rate at Low Stellar Temperatures  
(Under the Direction of Christian Iliadis)

Recent observations of isotopic abundances in the atmospheres of M13 red giant branch stars show an anticorrelation between Al and  $^{24}\text{Mg}$  abundances. These correlations are thought to be the result of deep mixing of material from the surface of the star into regions where the temperature is high enough to allow proton captures to take place. Production of Al and destruction of  $^{24}\text{Mg}$  depend on the  $^{24}\text{Mg}(p, \gamma)^{25}\text{Al}$  reaction rate at stellar temperatures  $T_9 \sim 0.04$  (where  $T_9$  denotes temperature in units of  $10^9$  K). However, the commonly used rate is too low to account for the observations within the present mixing models. There exists an uncertainty in the total width  $\Gamma$  of the  $E_R = 223$ -keV ( $E_x = 2485$  keV) resonance in the  $^{24}\text{Mg}(p, \gamma)^{25}\text{Al}$  reaction which could lead to enhancements in the reaction rate up to a factor of 32 at  $T_9 = 0.04$ . The main goal of this thesis is to accurately determine the properties of the  $E_R = 223$ -keV resonance in order to improve the reaction rate estimate for  $^{24}\text{Mg}(p, \gamma)^{25}\text{Al}$ .

Resonance strengths  $\omega\gamma$ ,  $\gamma$ -ray branching ratios  $\Gamma_\gamma/\Gamma$ , and mean lifetimes  $\tau$  were determined for the  $E_R = 223$ - and 419-keV resonances in  $^{24}\text{Mg}(p, \gamma)^{25}\text{Al}$ . These parameters allow for the determination of proton partial widths  $\Gamma_p$ ,  $\gamma$ -ray partial widths  $\Gamma_\gamma$ , and total widths  $\Gamma$  necessary for the calculation of the resonant cross section at  $E_p < 500$  keV. The rate for the  $^{24}\text{Mg}(p, \gamma)^{25}\text{Al}$  reaction for temperatures of  $T_9 = 0.02 - 2$  was calculated. The reaction rate deviates from the previous estimates by 18% to 45%, and therefore, the total width of the  $E_R = 223$ -keV resonance does not have a significant influence on the reaction rate.

In addition, branching ratios were determined for the 223-, 419-, 1616-, and 1654-keV resonances in  $^{24}\text{Mg}(p, \gamma)^{25}\text{Al}$ , and for the 406-keV resonance in

$^{27}\text{Al}(p, \gamma)^{28}\text{Si}$ . Spectroscopic factors were determined from the proton partial widths for the states corresponding to the  $E_R = 223$ - and 419-keV resonances. Resonance strength values were also determined for the 435-keV resonance in  $^{25}\text{Mg}(p, \gamma)^{26}\text{Al}$ , the 336- and 454-keV resonances in  $^{26}\text{Mg}(p, \gamma)^{27}\text{Al}$ , and the 406-keV resonance in  $^{27}\text{Al}(p, \gamma)^{28}\text{Si}$ .

# ACKNOWLEDGMENTS

There are a number of people who have contributed in different ways to making this journey a pleasure and a success. I would like to begin by thanking my Ph.D. advisor Christian Iliadis and my M.S. advisor Art Champagne for their constant encouragement, support, creative ideas, and faith in my abilities. It has been a pleasure to work with both of these gentlemen.

John Dunham, Richard O'Quinn, Paul Carter and Chris Westerfeldt are responsible for keeping the Triangle Universities Nuclear Laboratory (TUNL) standing and functional. I would like to thank them for their patience in teaching me the technical aspects of the lab and for their continual help and kindness throughout my years at TUNL. I would also like to thank Shane Canon, Sidney Edwards and Patrick Mulkey for their continual computer and electronic support.

My initiation to experimental nuclear astrophysics was led by Jeff Blackmon and Mariet Hoffstee. I would like to thank them for making the learning experience positive and for their patience in answering the strangest questions. As time progressed I benefited from the interaction with and enjoyed the wonderful friendships of several colleagues including Steve Hale, Kevin Veal, Bill Giest, Carl Brune, Becky Surman, Vera Hansper, and Peter Bertone.

My journey in physics began at St. Mary's College of Maryland. The enthusiasm, encouragement and high expectations of my advisor Teymour Darkhosh and faculty Katsunori Mita and David Humm made the experience challenging and exciting. I would also like to thank Joseph Machin (the other person in my classes of two) for his friendship, dedication, and motivation.

Most importantly I would like to thank my family. My mother, father, step-mother, sister and brother for their love and pride throughout the years. I would also like to thank my husbands family who have been a wonderful source of fun and support throughout our marriage. I need to thank my pets, especially Bonk, for their love. Lastly I would like to thank my husband and best-friend Devon, who beautifies every aspect of my life.

I would like to dedicate this thesis

in memory of  
JOSEPH EARL MACHIN IV  
June 16, 1971 – July 28, 1997

and to my child.





# CONTENTS

	Page
LIST OF TABLES . . . . .	xi
LIST OF FIGURES . . . . .	xiii
Chapter	
I. Motivation . . . . .	1
1.1 The Standard Model . . . . .	1
1.2 Observations and the Mixing Model . . . . .	3
1.3 Nuclear Physics . . . . .	7
II. Theory . . . . .	11
2.1 Capture Processes . . . . .	11
2.2 Reaction Rates . . . . .	14
III. Experimental Techniques . . . . .	19
3.1 Setup and Targets . . . . .	19
3.1.1 Branching Ratios . . . . .	19
3.1.2 Resonance Strengths . . . . .	20
3.1.3 Mean Lifetimes . . . . .	25
3.2 Detectors . . . . .	28
3.2.1 Efficiency . . . . .	28
3.2.2 Energy Calibration . . . . .	34
IV. Experimental Procedures and Results . . . . .	37
4.1 Branching Ratios . . . . .	37
4.2 Resonance Strengths . . . . .	43
4.3 Mean Lifetimes . . . . .	57

V.	Nuclear and Astrophysical Implications . . . . .	73
5.1	Nuclear Structure . . . . .	74
5.2	Determination of $S(E)$ . . . . .	76
5.3	Determination of $N_A \langle \sigma v \rangle$ . . . . .	80
5.4	Reaction Rate Uncertainties . . . . .	84
5.4.1	Statistical Uncertainties . . . . .	84
5.4.2	Systematic Uncertainties . . . . .	85
5.5	Implications of the Reaction Rate . . . . .	90
VI.	Appendix A: $F(\tau)$ Program . . . . .	95
A.1	Execution Commands . . . . .	95
A.2	Input Files . . . . .	97
VII.	REFERENCES . . . . .	101

# LIST OF TABLES

4.1	Angular distribution effects for the $E_R = 1654$ -keV resonance in $^{24}\text{Mg}(p, \gamma)^{25}\text{Al}$ . . . . .	41
4.2	$\Gamma_\gamma/\Gamma$ values for the 2485- and 2674-keV states in $^{25}\text{Al}$ . . . . .	42
4.3	Branching ratios for the $E_R = 1616$ - and 1654-keV resonances in $^{24}\text{Mg}(p, \gamma)^{25}\text{Al}$ . . . . .	43
4.4	Rutherford versus resonant scattering. . . . .	53
4.5	Branching ratios for the $E_R = 223$ - and 419-keV resonances in $^{24}\text{Mg}(p, \gamma)^{25}\text{Al}$ and the $E_R = 406$ -keV resonance in $^{27}\text{Al}(p, \gamma)^{28}\text{Si}$ . . . . .	55
4.6	A list of the $\gamma$ -ray transitions used to generate the yield curves for the determination of resonance strengths. . . . .	56
4.7	Values of resonance strengths. . . . .	57
4.8	Lifetime values of the 2485-, 2674-, 3823-, and 3859-keV states in $^{25}\text{Al}$ . . . . .	69
5.1	Summary of experimental results and individual $\Gamma$ values. . . . .	74
5.2	Proton, $\gamma$ -ray, and total widths for the $E_R = 223$ - and 419-keV resonances in $^{24}\text{Mg}(p, \gamma)^{25}\text{Al}$ . . . . .	74
5.3	Spectroscopic factors for the 2485-keV, 2674-keV, and bound states in $^{25}\text{Al}$ . . . . .	76
5.4	Input parameters for the calculation of the direct capture S-factor. . . . .	77
5.5	Input parameters for the calculation of the resonance capture S-factor. . . . .	78
5.6	List of narrow-resonance parameters used for the determination of the reaction rate. . . . .	81
5.7	Reaction rate in $\text{cm}^3/(\text{mole s})$ for $T_9 = 0.02 - 2$ . . . . .	83
5.8	Reaction rate fit parameters for $T_9 = 0.02 - 2$ . . . . .	85



# LIST OF FIGURES

1.1	HR diagram for globular cluster M15 [Bri94]. . . . .	2
1.2	Oxygen versus $M_{bol}$ for M13 red giants [Kra93]. . . . .	4
1.3	The Mg and Al observations of Shetrone [She96]. . . . .	5
1.4	The MgAl mass region. . . . .	6
1.5	Enhancement in the $^{24}\text{Mg}(p, \gamma)^{25}\text{Al}$ reaction rate resulting from different total widths [Zai97]. . . . .	8
2.1	S-factor for the $E_R = 223\text{-keV}$ resonance in $^{24}\text{Mg}(p, \gamma)^{25}\text{Al}$ for $\Gamma = 32\text{ eV}$ and $75\text{ meV}$ . . . . .	17
3.1	Diagram of the High Resolution Laboratory. . . . .	20
3.2	Energy level diagram for $^{25}\text{Al}$ . . . . .	21
3.3	$(p, \gamma)$ chambers. . . . .	22
3.4	Low-energy beam line. . . . .	23
3.5	Resonance strength experimental setup. . . . .	24
3.6	Lifetime experimental setup. . . . .	26
3.7	Ion implanter. . . . .	26
3.8	Yield curve at $E_R = 419\text{ keV}$ for the MgTa target. . . . .	27
3.9	Relative photopeak efficiency of the 140% HPGe detector. . . . .	29
3.10	Simple decay scheme to demonstrate summing. . . . .	29
3.11	Relative photopeak efficiencies of the 128% and 140% HPGe detectors. . . . .	31
3.12	Energy level diagram for the $^{19}\text{F}(p, \alpha_2\gamma)^{16}\text{O}$ reaction. . . . .	32
3.13	Angular distribution of $\alpha_2$ -particles emitted in the $^{19}\text{F}(p, \alpha_2\gamma)^{16}\text{O}$ reaction. . . . .	33
3.14	Gain shift test. . . . .	35
3.15	Residuals of the $\gamma$ -ray energy calibration. . . . .	36
4.1	$\gamma$ -ray spectrum for the determination of $\Gamma_\gamma/\Gamma$ of the $E_x =$ $2485\text{-keV}$ state. . . . .	38
4.2	Yield curves of the $E_R = 1616\text{-}$ and $1654\text{-keV}$ resonances in $^{24}\text{Mg}(p, \gamma)^{25}\text{Al}$ . . . . .	39

4.3	Least-squares fits to selected yield curve data. . . . .	40
4.4	$\gamma$ -ray and proton backscattering spectra for $E_p = 223$ keV in $^{24}\text{Mg}(p, \gamma)^{25}\text{Al}$ . . . . .	47
4.5	Elastic scattering spectra from Mg and Al targets. . . . .	48
4.6	$^{26}\text{Mg}(p, \gamma)^{27}\text{Al}$ yield curve and effect of carbon build-up. . . . .	49
4.7	$^{27}\text{Al}(p, \gamma)^{28}\text{Si}$ yield curve and effect of carbon build-up. . . . .	49
4.8	Elastic scattering of protons from Mg and Al. . . . .	51
4.9	Elastic scattering of protons from Mg and Al at the resonance energies. . . . .	52
4.10	Yield curves and fits. . . . .	58
4.11	Doppler-shifted $\gamma$ -ray spectra. . . . .	63
4.12	60% HPGe detector efficiency across the front face of the HPGe detector. . . . .	64
4.13	Stopping power of Al in the MgTa target. . . . .	66
4.14	Components of $F(\tau)$ for $\tau = 5$ fs. . . . .	67
4.15	$Q \cos \theta$ vs. $E_\gamma^{obs}$ for the $E_x = 2485$ -keV state in $^{25}\text{Al}$ . . . . .	68
4.16	$Q \cos \theta$ vs. $E_\gamma^{obs}$ for the $E_x = 2674$ -keV state in $^{25}\text{Al}$ . . . . .	69
4.17	$F(\tau)$ curve at $E_p = 1620$ keV. . . . .	70
4.18	$F(\tau)$ curve at $E_p = 1654$ keV. . . . .	71
5.1	S-factor for $^{24}\text{Mg}(p, \gamma)^{25}\text{Al}$ direct capture. . . . .	78
5.2	S-factor for the $E_R = 223$ -keV resonance in $^{24}\text{Mg}(p, \gamma)^{25}\text{Al}$ . . . . .	79
5.3	S-factor for the $E_R = 223$ -keV resonance and direct capture in the $^{24}\text{Mg}(p, \gamma)^{25}\text{Al}$ reaction. . . . .	80
5.4	Total reaction rate. . . . .	82
5.5	Present reaction rate relative to [Cau88]. . . . .	84
5.6	Numerical integration versus narrow-resonance approxima- tion for the $E_R = 223$ -keV resonance in $^{24}\text{Mg}(p, \gamma)^{25}\text{Al}$ . . . . .	88
5.7	Reaction rate enhancement resulting from an undetected resonance. . . . .	91
5.8	Abundance profiles of the NeNa and MgAl mass region for $Z$ $= 0.0004$ [Cav98]. . . . .	92
A.1	Outline of the FITFTAU program. . . . .	96

# Chapter 1

## Motivation

### 1.1 The Standard Model

Globular clusters, found in the halo of the Galaxy, are comprised of hundreds of thousands of stars gravitationally bound to one another. In the standard model, the stars in a cluster are assumed to be of the same age (co-eval) and formed from chemically homogeneous material. This material is the ash of different nucleosynthetic processes. Since globular clusters contain some of the oldest stars in our Galaxy, studies of the chemical composition of these stars can yield information about galactic chemical evolution and galaxy formation. Since the stars within a cluster are the same age and composition, the rate of evolution of a star is a function of its mass. Consequently, the study of globular cluster stars can shed light on the course of stellar evolution [Kra94].

The stage of evolution of a star can be identified by plotting its surface temperature versus luminosity, *i.e.* a Hertzsprung-Russel (HR) diagram. Figure 1.1 shows the HR diagram of globular cluster M15. The first stage of evolution is referred to as the main sequence. The nucleosynthesis of a main sequence star takes place in the core, where hydrogen is converted into helium, predominantly via the  $p + p \rightarrow {}^4\text{He}$  chain (pp chain). A star will spend the majority of its life on the main sequence, until the hydrogen in the core becomes depleted. As a

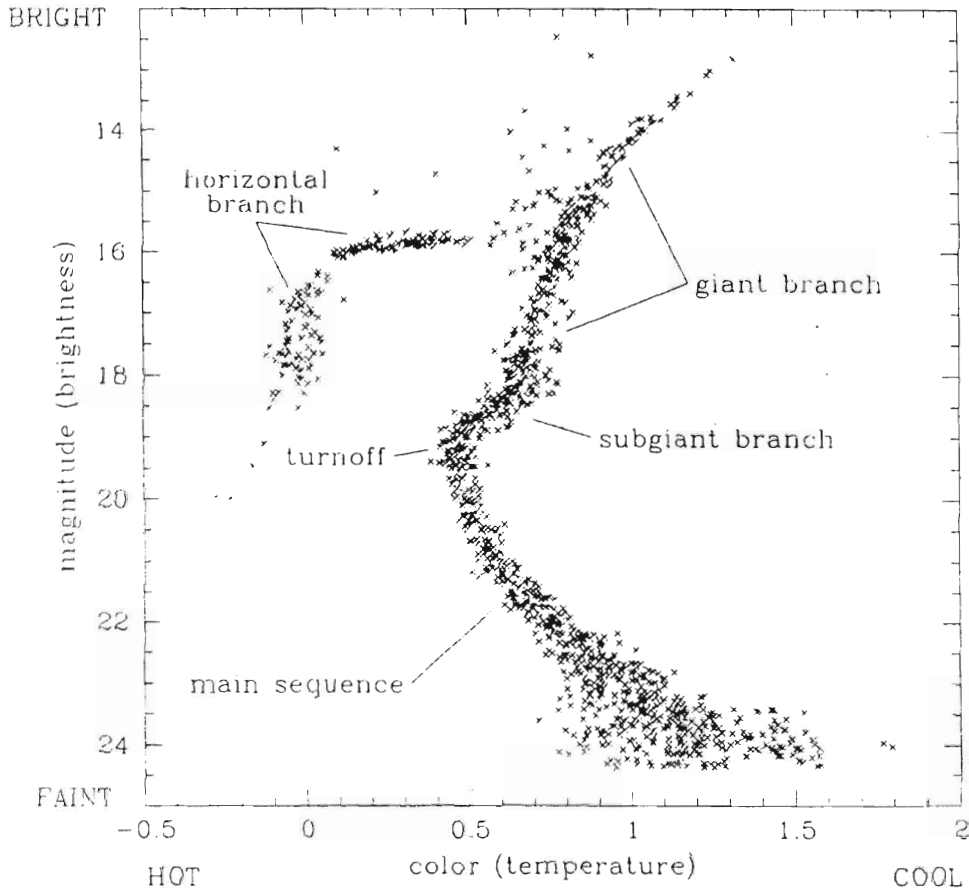


Figure 1.1: HR diagram for globular cluster M15 taken from [Bri94].

result, the star turns off the main sequence and a dredge-up of elements, previously involved in hydrogen burning, transports the material to the surface of the star. Small changes in the surface abundances of nitrogen and the  $^{12}\text{C}/^{13}\text{C}$  ratio are expected as a result of the dredge-up process. As hydrogen starts to burn in a shell surrounding the core, the dredge up process ceases, and the star evolves up the giant branch.

A red giant branch star is comprised of a number of shells. The core of the red giant consists of the ash of hydrogen burning, *i.e.* helium. The shell that surrounds the core is the location of nucleosynthesis and consists of the processing of hydrogen into helium via the CNO cycle and the pp chain. The next shell consists of a radiative zone, surrounded by the outermost shell, commonly



referred to as the envelope. The surface of the envelope is the region from which observations of the stars are made. As the star evolves, or ascends the red giant branch, the temperature in the hydrogen burning shell increases, increasing the luminosity of the star [Ibe70].

As a consequence of the standard model, the abundance of materials on the surface of red giant branch stars should be similar within a given cluster, since all of the stars have undergone the same processing, originated from the same material, and have approximately the same mass (if they are in close proximity on the red giant branch).

## 1.2 Observations and the Mixing Model

Observations generally take place near the top of the red giant branch since these are the most luminous and therefore, the most visible stars. Variations are seen in the abundances of many elements within a cluster of red giant branch stars, in contradiction with the standard model. For example, the  $^{12}\text{C}/^{13}\text{C}$  ratio ranges from 4 up to factors of 10, outside the range allowed by the standard evolutionary theory. In addition, anticorrelations between the abundances of C and O with N are seen on the surface of red giant branch stars. There exist two common explanations for the source of these observations. The first explanation is that abundance variations exist in the material from which the stars are formed. The second is that there exist some evolutionary process that allows for the nucleosynthesis of envelope material in the hydrogen burning shell, changing the abundances of surface elements [Kra94]. Although the primordial scenario has not been ruled out, a number of abundance observations on red giant branch stars support the evolutionary theory. Of particular interest for the present work are observations of M13 red giant branch stars, which lend confidence to the mixing model of Sweigart and Mengel [Swe79], but raise questions regarding the  $^{24}\text{Mg}(p, \gamma)^{25}\text{Al}$  reaction rate.

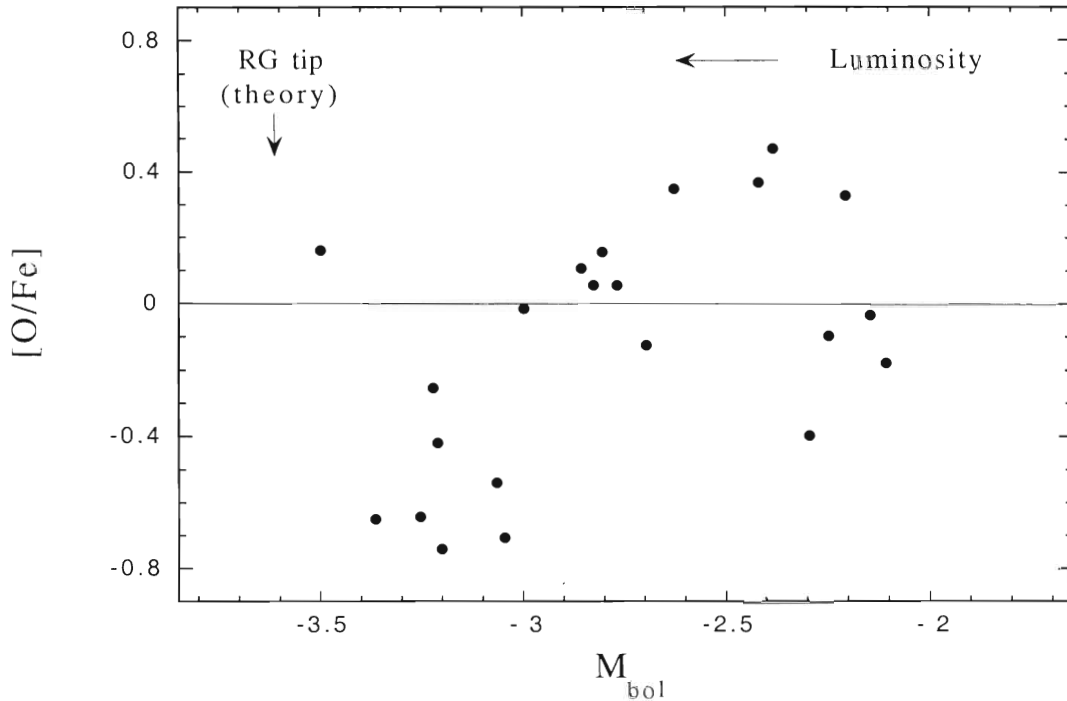


Figure 1.2: The observations of [Kra93] on M13 red giant branch stars. The oxygen depletion as a function of evolution up the red giant branch supports the Sweigart and Mengel evolutionary model [Swe79].

The mixing model of Sweigart and Mengel [Swe79] originated in an attempt to explain the anticorrelations seen between the elements C, N, and O found on the surface of the red giant branch stars. The mixing model allows circulation, driven by rotation, within the radiative zone to mix material in the envelope of the star to regions where hydrogen burning can occur [Swe79]. The net effect of the CNO cycle is to deplete C and O while enhancing N. In addition, the  $^{12}\text{C}/^{13}\text{C}$  ratio can decrease until an equilibrium value of about 4 is reached. The nuclear processing of C, N, and O via the CNO cycle is generally consistent with the observations.

Kraft *et al.* [Kra93] observed the oxygen abundance  $[\text{O}/\text{Fe}]^1$  in M13 red giant branch stars as a function of the bolometric magnitude  $M_{bol}$  (see figure 1.2), or the stage of evolution of the star on the red giant branch. The M13 red giant

<sup>1</sup> $[\text{O}/\text{Fe}] \equiv \log[(\text{O}/\text{Fe})/(\text{O}/\text{Fe})_{\odot}]$  where  $\odot$  represents the solar value.

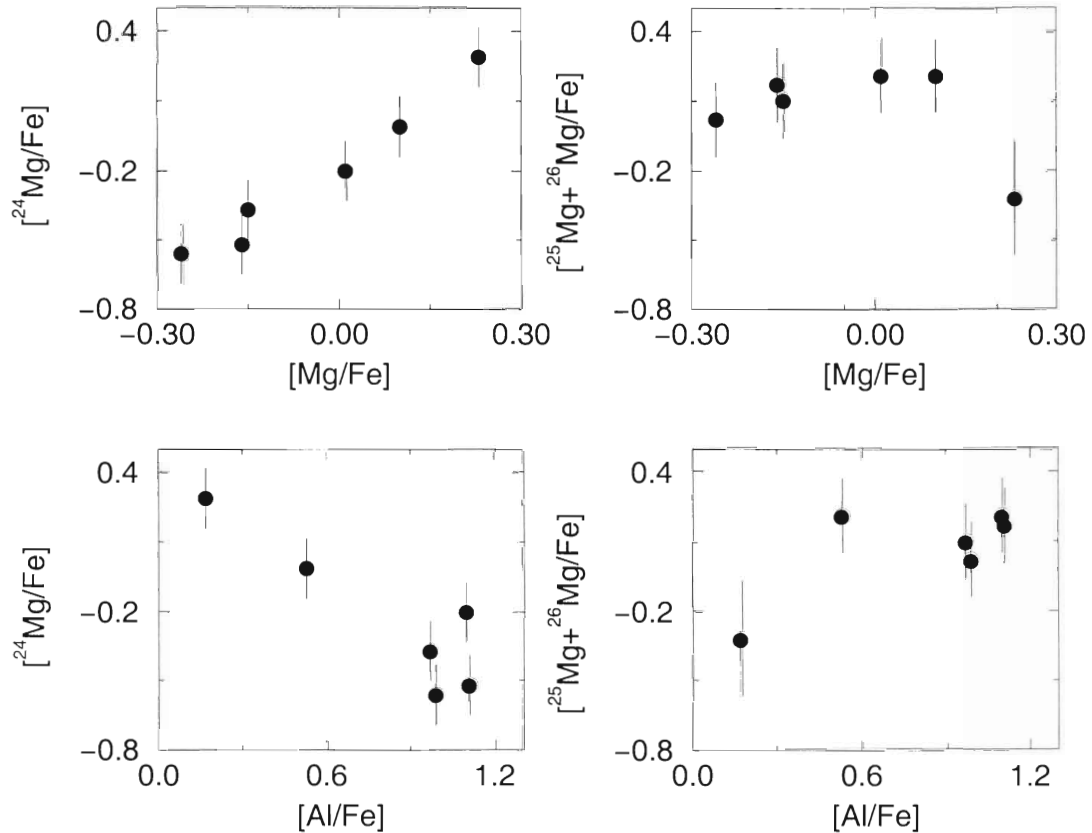


Figure 1.3: The observations of Shetrone [She96] on M13 red giant branch stars showing the  $^{24}\text{Mg}$  isotopic abundance (*left*) and the  $^{25}\text{Mg} + ^{26}\text{Mg}$  isotopic abundance (*right*) as a function of the total Mg abundance (*top*) and the total Al abundance (*bottom*).

branch stars showed an anticorrelation between the oxygen abundance and the evolutionary stage, supporting the idea that nucleosynthesis via the CNO cycle occurs as the star ascends the red giant branch.

Shetrone observed  $^{24}\text{Mg}$ ,  $^{25}\text{Mg} + ^{26}\text{Mg}$ , and Al on the surface of six M13 red giant branch stars (see figure 1.3) [She96]. Although variations in Al have been seen on the surface of a number of red giant branch stars, Shetrone is the first to actually observe the isotope  $^{24}\text{Mg}$  in red giants. The correlation between  $^{24}\text{Mg}$  and Mg as well as the anticorrelation of  $^{24}\text{Mg}$  with Al suggest that stars enhanced in Al are enhanced as a result of  $^{24}\text{Mg}(p, \gamma)^{25}\text{Al}$ . The  $^{25}\text{Mg}$  and  $^{26}\text{Mg}$  isotopes could not be resolved from one another, so the abundance sum is plotted

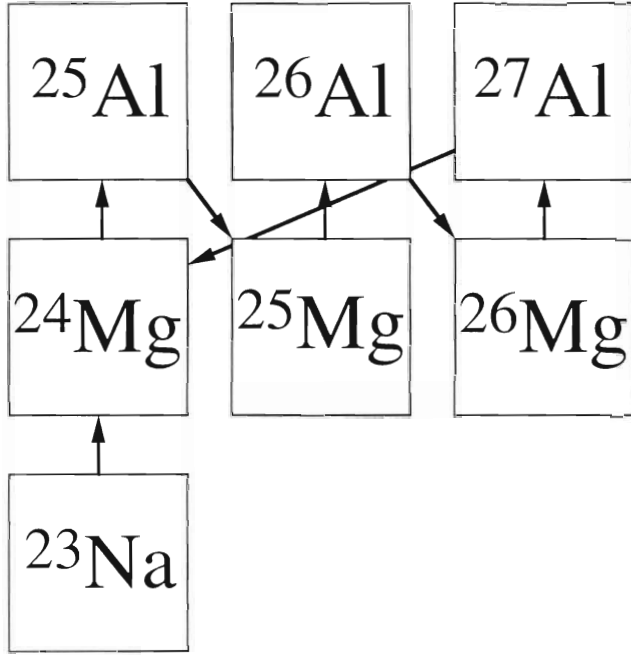


Figure 1.4: The MgAl mass region.

as a function of Mg and Al. The  $[(^{25}\text{Mg} + ^{26}\text{Mg})/^{24}\text{Mg}]$  ratio is approximately 0.79, whereas the solar ratio is 0.28. The abundance of  $^{25}\text{Mg} + ^{26}\text{Mg}$  is roughly constant for variations of Al, and therefore  $^{25}\text{Mg} + p$  and  $^{26}\text{Mg} + p$  are not believed to be the source of the production of Al in stars near the tip of the red giant branch.

Figure 1.4 is a diagram of the magnesium-aluminum mass region (MgAl region). The flow of nuclear reactions is depicted by arrows, where an arrow pointing vertically up indicates a  $(p, \gamma)$  reaction, diagonally between adjoining columns indicates  $\beta$ -decay and a long diagonal arrow represents a  $(p, \alpha)$  reaction. The reactions are thought to take place in red giant branch stars at temperatures below  $T_9 \sim 0.055$  or  $0.055 \times 10^9$  K. A stellar model code was used by Langer *et al.* to monitor the flow of reactions in figure 1.4 for  $T_9 = 0.04$  and  $\rho = 44.7 \text{ g/cm}^3$  [Lan93], using the most up-to-date reaction rates. The production of Al results from  $^{25}\text{Mg} + p$  and  $^{26}\text{Mg} + p$ , and the flow from  $^{24}\text{Mg}$  to  $^{25}\text{Al}$  is suppressed due to the much slower  $^{24}\text{Mg}(p, \gamma)^{25}\text{Al}$  reaction rate relative to the  $^{25}\text{Mg}(p, \gamma)^{26}\text{Al}$ .

and  $^{26}\text{Mg}(p, \gamma)^{27}\text{Al}$  reactions [Lan93].

Stellar modelers have attempted to match the observed Al enhancements and/or  $^{24}\text{Mg}$  depletions by a number of methods, for example, by increasing the initial abundances of  $^{25}\text{Mg}$  and  $^{26}\text{Mg}$  [Lan95], by increasing the burning temperature to  $T_9 = 0.07$  [Lan97], and by varying the  $^{24}\text{Mg}(p, \gamma)^{25}\text{Al}$  reaction rate [Cav98]. Increasing the initial abundances of  $^{25}\text{Mg}$  and  $^{26}\text{Mg}$  ( $\sim 4$  times the solar values) could lead to a significant depletion in the total Mg abundance and an increase in Al, but this would be inconsistent with the  $^{24}\text{Mg}$  depletions observed by Shetrone [She96]. Increasing the temperature of the star to  $T_9 = 0.07$  would allow for the processing of  $^{24}\text{Mg}$  into Al, but would require thermal instabilities in the star [Lan97]. In order to reproduce the observations by varying the  $^{24}\text{Mg}(p, \gamma)^{25}\text{Al}$  reaction rate, the rate would need to be increased by a factor of 35 [Cav98] above the presently assumed rate [Cau88].

### 1.3 Nuclear Physics

In the temperature range of interest, the  $^{24}\text{Mg}(p, \gamma)^{25}\text{Al}$  reaction rate is determined by direct capture to the bound states in  $^{25}\text{Al}$  and capture into the lowest lying resonance at  $E_R = 223$  keV (see chapter 2 and figure 3.2). Zaidins and Langer explored the  $^{24}\text{Mg}(p, \gamma)^{25}\text{Al}$  reaction and suggested that an increase in the total width  $\Gamma$  of the  $E_x = 2485$ -keV state (corresponding to the  $E_R = 223$ -keV resonance) could lead to enhancements up to a factor of 32 in the reaction rate at  $T_9 = 0.04$  [Zai97] (see figure 1.5). An increase in the total width would mean that the tail of the  $E_R = 223$ -keV resonance could dominate the cross section at the energies of interest, leading to an enhancement in the total reaction rate. The total width of the  $E_x = 2485$ -keV state is presently assumed to be 75 meV, resulting from a figure in a direct capture paper of Trautvetter and Rolfs [Tra75a]. This value presumably comes from the unpublished thesis work of Dworkin-Charlesworth [Dwo74]. The procedure and results of reference [Dwo74]

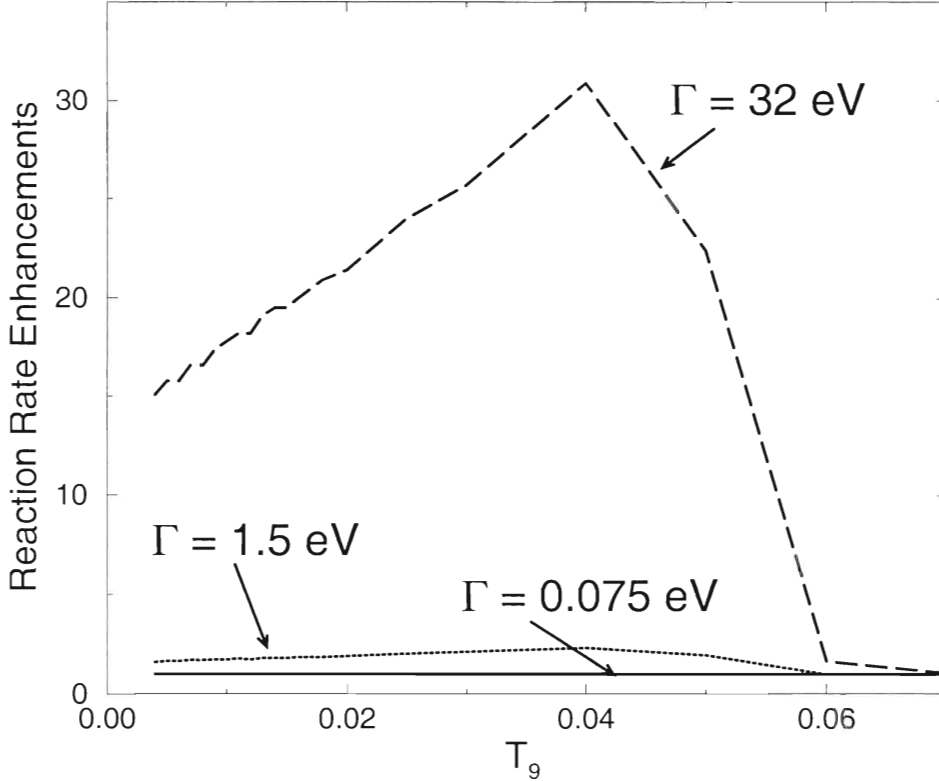


Figure 1.5: The enhancements of the  $^{24}\text{Mg}(p, \gamma)^{25}\text{Al}$  reaction rate as a result of increasing the total width of the  $E_x = 2485\text{-keV}$  state [Zai97].

are discussed in detail in section 4.3. In the published literature, an experimental upper limit of 32 eV is set on the total width of the  $E_x = 2485\text{-keV}$  state from the shape of the front edge of a thick-target yield curve [Uhr85].

In the present thesis, the total width of the  $E_x = 2485\text{-}$  and  $2674\text{-keV}$  states were determined experimentally by two independent methods. The first method requires measuring the  $\gamma$ -ray branching ratio  $\Gamma_\gamma/\Gamma$  and the resonance strength  $\omega\gamma$ . These quantities not only allow for the determination of the total width, but also the values for the proton partial width and the  $\gamma$ -ray partial width, necessary for the proper calculation of the resonance tail. The second determination involves the measurement of the mean lifetime  $\tau$  of the  $E_x = 2485\text{-}$  and  $2674\text{-keV}$  states.

A state in a nucleus can often be formed or can decay through the capture

or emission of a particle or  $\gamma$ -ray. The probability for the formation or decay of a state can be written in terms of  $\Gamma_i$ , the partial width for decay in channel  $i$ , in energy units. The sum of all the partial widths of a state represents the total width  $\Gamma$  of that state. The states of interest can only decay via proton or  $\gamma$ -ray emission and hence  $\Gamma = \Gamma_p + \Gamma_\gamma$ .

The strength of a  $(p, \gamma)$  resonance is defined as [Rol88]

$$\omega\gamma = \frac{2J + 1}{(2J_p + 1)(2J_t + 1)} \frac{\Gamma_p \Gamma_\gamma}{\Gamma} \quad (1.1)$$

where  $J$ ,  $J_p$ , and  $J_t$  are the spins of the compound nuclear state, projectile, and target, respectively,  $\Gamma_p$  is the proton partial width,  $\Gamma_\gamma$  is the  $\gamma$ -ray partial width and  $\Gamma$  is the total width.

The second method used for the determination of the total width  $\Gamma$  of the  $E_x = 2485$ - and  $2674$ -keV states is the measurement of the mean lifetime  $\tau$ . This is accomplished via the Doppler-shift-attenuation method (DSAM), as discussed in section 4.3. This completely independent determination of the total width acts as a check of internal consistency, leading to a greater confidence in the final result.

In nuclear astrophysics, the reaction rate is commonly determined with the narrow-resonance formalism which is proportional to the resonance strength. The present procedure used to determine absolute resonance strengths produced more precise values than could be found in the literature. Therefore, a number of strength values were also determined for resonances in  $^{25}\text{Mg}(p, \gamma)^{26}\text{Al}$ ,  $^{26}\text{Mg}(p, \gamma)^{27}\text{Al}$  and  $^{27}\text{Al}(p, \gamma)^{28}\text{Si}$  in order to extend the set of standard  $(p, \gamma)$  resonance strengths in the sd-shell [Sar82] to energies below  $E_R = 0.5$  MeV. Astrophysically relevant strengths can be determined relative to these standard strengths. The resonance strength determinations resulting from the present work are also described in [Pow98].

The resonance parameters determined throughout this work can also shed light in several subfields of nuclear physics. The quantities  $\Gamma_\gamma/\Gamma$ ,  $\omega\gamma$  and  $\tau$  can

be used in order to determine nuclear properties such as total widths, partial widths, and spectroscopic factors. For example, the knowledge of spectroscopic factors is used in chapter 2 to test the predictions of direct capture models.

An outline of the present work is as follows. Chapter 2 describes the two capture processes, direct capture and resonance capture, and gives an introduction to reaction rates. Chapter 3 describes the experimental setup, including targets and detectors, used for the determination of  $\Gamma_\gamma/\Gamma$ ,  $\omega\gamma$ , and  $\tau$ . Chapter 4 describes the approach used for each of the measurements and the results. Finally, chapter 5 presents total widths,  $\gamma$ -ray partial widths, proton partial widths, and spectroscopic factors of the  $E_x = 2485$ - and  $2674$ -keV states in  $^{25}\text{Al}$ . Chapter 5 also presents the reaction rate for temperatures of  $T_9 = 0.02 - 2$  using the presently determined resonance properties and the rate is compared to the previous values of [Cau88]. Implications of the new reaction rate and associated statistical and systematic uncertainties are also discussed.

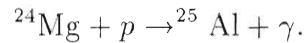


# Chapter 2

## Theory

### 2.1 Capture Processes

There exist two types of capture processes relevant to the  $^{24}\text{Mg}(p, \gamma)^{25}\text{Al}$  reaction. One process is direct capture whereby the proton is captured and the  $\gamma$ -ray is emitted in a single step, as indicated by



The second capture process is referred to as resonance capture, since the reaction proceeds through an excited state in the compound nucleus, *i.e.*



The different capture processes contribute to the total cross section.

The direct capture process, or single step process, occurs at all incident particle energies. The direct capture contribution to a cross section,  $\sigma_D(E)$ , is a smoothly varying function of the incident particle energy and describes the formation of a final state from two free particles via their interaction with the electromagnetic field. A single-particle potential model [Rol73] is used throughout this thesis to determine the energy dependence of the direct capture cross section (TEDCA) [Moh93], and is normalized to the experimentally determined cross sections for direct capture to bound states in  $^{25}\text{Al}$  [Tra75a].

The theoretical expression for the cross section resulting from direct capture for an E1  $\gamma$ -ray decay has been calculated by [Rol73] and is given by

$$\sigma_D(E) = 0.0716\mu^{3/2} \left( \frac{Z_1}{M_1} - \frac{Z_2}{M_2} \right)^2 \frac{E_\gamma^3}{E^{3/2}} \frac{(2J_f + 1)(2l_i + 1)}{(2J_p + 1)(2J_t + 1)(2l_f + 1)} \times (l_i 0 1 0 | l_f 0)^2 R_{l_i l_f}^2 \quad (2.1)$$

in units of  $\mu b$ , where  $\mu$  is the reduced mass in amu,  $Z_1$  ( $Z_2$ ) is the charge of the projectile (target),  $M_1$  ( $M_2$ ) is the mass of the projectile (target),  $E_\gamma$  is the  $\gamma$ -ray energy,  $E$  is the incident projectile energy,  $J_f$ ,  $J_p$ , and  $J_t$  are the spins of the final state, projectile, and target, respectively,  $l_i$  ( $l_f$ ) is the initial (final) state orbital angular momentum and  $(l_i 0 1 0 | l_f 0)$  is a Clebsch-Gordan coefficient. The radial integral  $R_{l_i l_f}$  is given by

$$R_{l_i l_f} = \int u_c(r) \theta_{E1}(r) u_b(r) r^2 dr \quad (2.2)$$

where  $u_c(r)$  and  $u_b(r)$  are the continuum and bound-state wave functions, respectively, and  $\theta_{E1}(r)$  is the radial part of the E1 electromagnetic operator. Only E1  $\gamma$ -ray transitions were considered because contributions from other transitions proved to be negligible in comparison. The calculation of  $R_{l_i l_f}$  is performed assuming the same Wood-Saxon potential for both the continuum and bound state, with radius parameter  $r_0 = 1.25$  fm and diffuseness  $a = 0.65$  fm, and a potential depth chosen to reproduce the binding energy of the final state. In addition, the final-state wave function was constrained to contain the proper number of nodes.

Resonance capture occurs when an excited state in a nucleus is formed, followed by the de-excitation of that state through the emission of a  $\gamma$ -ray. The cross section resulting from resonance capture is maximal at the resonance energy and falls off at energies far from the resonance. The rate of decrease of the resonant cross section depends on  $\Gamma$ , the width of the state. When a capture proceeds via a single resonance, the cross section can be approximated by the Breit-Wigner formula [Bre36] written as

$$\sigma_R(E) = \frac{\pi}{k^2} \frac{2J + 1}{(2J_p + 1)(2J_t + 1)} \frac{\Gamma_p \Gamma_\gamma}{(E - E_R)^2 + (\Gamma/2)^2} \quad (2.3)$$

where  $k$  ( $= 2\pi/\lambda$ ) is the wavenumber of the incident particle,  $\Gamma_p$  is the proton partial width,  $\Gamma_\gamma$  is the  $\gamma$ -ray partial width,  $\Gamma$  is the total width,  $J$  is the spin of the compound nuclear state and  $E_R$  is the energy of the incident particle at which the resonance is formed.

Interference between direct capture and a resonance may play a role in determining the energy dependence of the cross section. The cross section  $\sigma(E, \theta)$  for an incident particle of energy  $E$  measured at an angle  $\theta$  resulting from direct and resonance capture, including interference effects, is given by [Rol73]

$$\begin{aligned} \sigma(E, \theta) &= \sigma_R(E)W_R(\theta) + \sigma_D(E)W_D(\theta) \\ &\pm 2\sqrt{\sigma_R(E)\sigma_D(E)}\cos(\varphi_R - \varphi_D)W_{R,D}^{int}(\theta). \end{aligned} \quad (2.4)$$

$W_R(\theta)$ ,  $W_D(\theta)$ , and  $W_{R,D}^{int}(\theta)$  are the angular distributions of the resonance capture, direct capture, and interference terms in the cross section, respectively, and  $\varphi_R$  and  $\varphi_D$  are the direct and resonant capture phase shifts [Fer65].

The angular distribution of the resonance capture and direct capture processes can be written as

$$W(\theta) = \sum_m a_m P_m(\cos \theta) \quad (2.5)$$

where  $a_m$  is a coefficients and  $P_m$  is a Legendre polynomial of order  $m$ , of which the most significant are

$$\begin{aligned} P_0(\cos \theta) &= 1 \\ P_2(\cos \theta) &= \frac{1}{2}[3 \cos^2(\theta) - 1] \\ \text{and } P_4(\cos \theta) &= \frac{1}{8}[35 \cos^4(\theta) - 30 \cos^2(\theta) + 3]. \end{aligned} \quad (2.6)$$

The highest order Legendre polynomial that may contribute to the angular distribution in the resonance cross section is determined by [Bie53]

$$m \leq \min(2J, 2l_i, 2L) \quad (2.7)$$

where  $m$  is an even integer and  $L$  is the multipolarity of the emitted  $\gamma$ -ray. The direct capture angular distribution was also measured by [Tra75a], yielding at most a  $P_2(\cos \theta)$  component for each of the final states.

The angular distribution of the interference term is given by [Rol73]

$$W_{R,D}^{int}(\theta) = (-1)^P \hat{J}_2 \hat{l}_f W(l_R L_R J_1 J_3; l_f J_2) \sum_m (l_R 0 l_D 0 | m 0) \bar{Z}(l_R L_R l_D L_D; l_f m) P_m(\theta) \quad (2.8)$$

where  $P$  is a constant [Rol73],  $\hat{J} \equiv \sqrt{2J+1}$ ,  $l_R$  ( $l_D$ ),  $L_R$  ( $L_D$ ),  $J_1$ ,  $J_2$ ,  $J_3$ , and  $l_f$  are the initial state resonance (direct capture) orbital angular momentum, the multipolarity of the resonance (direct capture)  $\gamma$ -ray, the channel spin of the initial state ( $\vec{J}_p + \vec{J}_t$ ), resonance, and final state, and the final-state orbital angular momentum for direct capture, respectively.  $W(l_R L_R J_1 J_3; l_f J_2)$  is a Racah coefficient and  $\bar{Z}(l_R L_R l_D L_D; l_f m)$  is a combination of a Clebsch-Gordan coefficient and a Racah coefficient.

The astrophysical S-factor  $S(E)$  is given by [Bur57]

$$S(E) = \sigma(E) E e^{2\pi\eta} \quad (2.9)$$

where  $\sigma(E)$  is the cross section,  $E$  is the incident projectile energy, and  $\eta$  is the Sommerfeld parameter given by

$$2\pi\eta = 31.29 Z_1 Z_2 \left( \frac{\mu}{E} \right)^{1/2}. \quad (2.10)$$

$\mu$  and  $E$  in equation 2.10 are in units of amu and keV, respectively. Commonly, the energy range of interest is below the experimentally obtainable region, requiring an extrapolation of the cross section to the lower energies of interest. Since the cross section for charged particle capture reactions decreases strongly at the lower energies, the extrapolation is more straightforward when made with the less energy-dependent S-factor.

## 2.2 Reaction Rates

The reaction rate per particle pair is given by [Rol88]

$$\langle \sigma v \rangle = \left( \frac{8}{\pi \mu} \right)^{1/2} \frac{1}{(k_b T)^{3/2}} \int_0^\infty S(E) \exp\left( -\frac{E}{k_b T} - \frac{b}{E^{1/2}} \right) dE \quad (2.11)$$

where  $k_b$  is the Boltzmann constant,  $T$  is the stellar temperature in Kelvin and  $b$  is given by

$$b = 0.989 Z_1 Z_2 \mu^{1/2} (\text{MeV})^{1/2}. \quad (2.12)$$

The energies at which the nuclear reactions take place in a stellar environment result from a product of the energy distribution of nuclei in the star, described by the Maxwell-Boltzmann distribution, and the probability of tunneling through the Coulomb barrier. Assuming a constant S-factor the calculation of the probability distribution as a function of energy can be determined. The distribution, or Gamow peak, has a maximum at an energy  $E_0$  and a full-width-half-maximum (FWHM)  $\Delta$ , given by [Bur57]

$$\begin{aligned} E_0 &= 1.22(Z_1^2 Z_2^2 \mu T_6^2)^{1/3} \text{ keV} \\ \text{and } \Delta &= 0.749(Z_1^2 Z_2^2 \mu T_6^5)^{1/6} \text{ keV}. \end{aligned} \quad (2.13)$$

For example, at  $T_9 = 0.04$  we are interested in determining the S-factor for  $E_0 \sim 75 \pm 40$  keV. This energy region of the S-factor as shown in figure 2.1 is dominated by direct capture (DC) and possibly the tail of the  $E_R = 223$ -keV resonance.

For determination of the reaction rate per particle pair, a numerical integration of equation 2.11 is performed once the astrophysical S-factor has been determined. For the direct capture component, the S-factor is determined via the single particle potential model described in section 2.1. For the resonance contribution, the S-factor results from the Breit-Wigner cross section (equation 2.3 and 2.9). If the direct capture and resonance capture processes interfere, the total S-factor calculated via equation 2.4 must be determined and incorporated into equation 2.11.

For determination of the reaction rate for a broad resonance, the energy dependent quantities in the Breit-Wigner cross section (the de-Broglie wavelength and the partial and total widths) must be calculated. The proton partial width  $\Gamma_p(E)$  can be written in terms of the proton partial width at the resonance

$\Gamma_p(E_R)$  (given in chapter 5) as

$$\Gamma_p(E) = \Gamma_p(E_R) \frac{P_l(E)}{P_l(E_R)} \frac{\theta_{sp}^2(E)}{\theta_{sp}^2(E_R)} \quad (2.14)$$

where the penetration factor  $P_l(E)$  is determined from a computation of the regular ( $F_l$ ) and irregular ( $G_l$ ) Coulomb wave functions at the interaction radius  $a$ , given by

$$P_l = \left( \frac{kr}{F_l^2 + G_l^2} \right)_{r=a} \quad (2.15)$$

where  $a$  is usually written as  $a = a_0(A_t^{1/3} + A_p^{1/3})$ ,  $A_t$  and  $A_p$  are the mass of the target and projectile, respectively, and  $k$  is the channel wave number. The dimensionless single-particle reduced width  $\theta_{sp}^2$  is calculated using the formalism of Iliadis [Ili97].

The  $\gamma$ -ray partial width,  $\Gamma_\gamma(E)$ , can be written in terms of the  $\gamma$ -ray partial width at the resonance energy  $\Gamma_\gamma(E_R)$  (given in chapter 5) as

$$\Gamma_\gamma(E) = \Gamma_\gamma(E_R) \left[ \frac{E + Q_{p\gamma} - E_{xf}}{E_R + Q_{p\gamma} - E_{xf}} \right]^{2L+1} \quad (2.16)$$

where  $Q_{p\gamma}$  is the Q-value of the reaction ( $Q_{p\gamma} = 2271.33 \pm 0.67$  keV [Aud95] for the  $^{24}\text{Mg}(p, \gamma)^{25}\text{Al}$  reaction),  $E_{xf}$  is the energy of the final state, and  $L$  is the multipolarity of the  $\gamma$ -ray emitted in the decay.

A resonance is considered narrow if  $\Gamma \ll E_R$ , and therefore the energy dependence of the incident particles and the partial widths are negligible, and can be removed from the integrand of equation 2.11. If the resonance is within the range  $E_0 \pm 2\Delta$  [Bur57] the reaction rate per particle pair can be approximated by

$$\langle \sigma v \rangle = \left( \frac{2\pi}{\mu k_b T} \right)^{3/2} \hbar^2 (\omega\gamma)_R \exp\left(-\frac{E_R}{k_b T}\right) \quad (2.17)$$

where  $(\omega\gamma)_R$  is the resonance strength at the resonance energy.

The enhancement in the reaction rate resulting from variations in the total width of the  $E_x = 2485$ -keV state in  $^{25}\text{Al}$  can be understood by looking at the astrophysical S-factor (see figure 2.1) at the energies of interest. If the width of

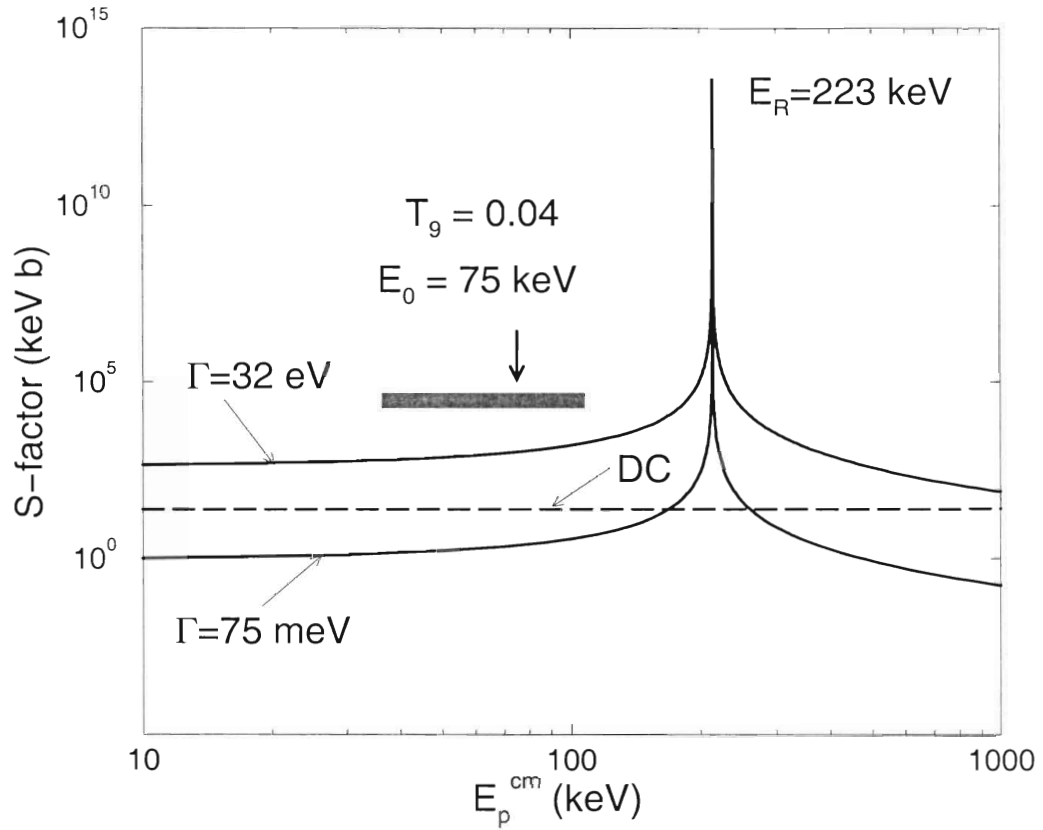


Figure 2.1: The S-factor for the  $E_R = 223$ -keV resonance in  $^{24}\text{Mg}(p, \gamma)^{25}\text{Al}$  for  $\Gamma = 32$  eV and 75 meV and direct capture contribution (DC) at the energy range of interest (the black bar) for  $T_9 = 0.04$ .

the  $E_x = 2485$ -keV state is  $\Gamma = 75$  meV, the S-factor is dominated by the direct capture (DC) component at  $E_0 = 75$  keV. If the width of the  $E_x = 2485$ -keV state is increased to  $\Gamma = 32$  eV (and  $\omega\gamma$  is kept constant), the S-factor is dominated by the tail of the  $E_x = 2485$ -keV state, which implies that the reaction rate would be enhanced relative to the case of  $\Gamma = 75$  meV, as demonstrated by [Zai97] and shown in figure 1.5.





# Chapter 3

## Experimental Techniques

### 3.1 Setup and Targets

#### 3.1.1 Branching Ratios

The data needed to determine  $\Gamma_\gamma/\Gamma$  for the  $E_x = 2485$ - and  $2674$ -keV states<sup>2</sup> were taken at the High-Resolution Laboratory (HRL) at the Triangle Universities Nuclear Laboratory (TUNL) located on the Duke University campus. The HRL consists of a modified 4-MV KN Van de Graff accelerator, from which protons are extracted, bent through an analyzing magnet and directed to the target (see figure 3.1) [Wes87, Wes88]. In order to determine the value  $\Gamma_\gamma/\Gamma$  for the 2485-keV state, a  $10\text{-}\mu\text{A}$  proton beam at an energy of  $E_p = 1620$  keV (populating the  $E_x = 3823$ -keV state) was incident on a  $^{24}\text{Mg}$  target (see figure 3.2). The target was fabricated by reducing  $^{24}\text{MgO}$  with Zr [Tak66] and evaporating the  $^{24}\text{Mg}$  onto a 0.25-mm-thick Ta backing [Max67, Mug79]. The chambers shown in figure 3.3 were constructed such that the target could be positioned normal to and  $45^\circ$  with respect to the incident beam. The  $45^\circ$  chamber was used for the determination of the  $\gamma$ -ray branching ratios. A cold trap helped reduce carbon

---

<sup>2</sup> $E_R$  and  $E_p$  values are given in the lab frame, whereas all measured and calculated quantities are given in the c.m. frame. All resonance and excitation energies are adopted from [End98].

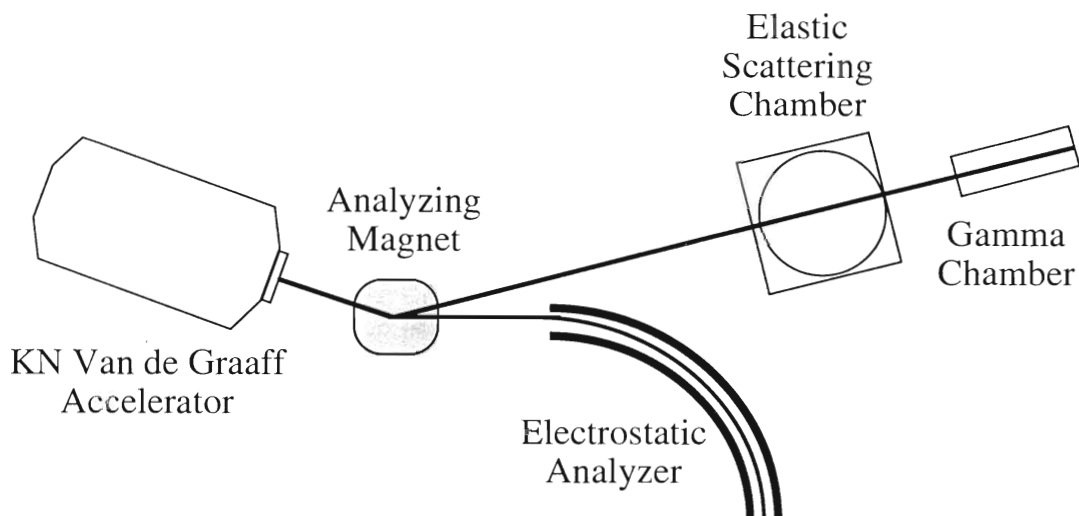


Figure 3.1: Diagram of the High Resolution Laboratory.

buildup and direct water cooling prevented target deterioration. A 140% high purity germanium (HPGe) detector was placed at an angle of  $55^\circ$  with respect to the incident beam and located at a distance of 6 cm from the target center to the front face of the detector. The absolute proton energy calibration was determined from yield curves over the  $E_R = 1654$ -keV resonance in  $^{24}\text{Mg}(p, \gamma)^{25}\text{Al}$  and the  $E_R = 992$ - and  $1317$ -keV resonances in  $^{27}\text{Al}(p, \gamma)^{28}\text{Si}$ . The uncertainty in the calibration was less than 1 keV. Additional data were taken at the  $E_R = 1654$ -keV resonance to determine  $\Gamma_\gamma/\Gamma$  for the  $E_x = 2674$ -keV state. A total charge of 320 mC were accumulated on target at  $E_p = 1616$  keV and 50 mC at  $E_p = 1654$  keV.

### 3.1.2 Resonance Strengths

The resonance strength measurement took place at TUNL, utilizing unpolarized  $\text{H}^-$  extracted from the Atomic Beam Polarized Ion Source at an energy of 75 keV. The  $\text{H}^-$  were bent through an inflection magnet and accelerated through the minitandem [Bla93]. The electrons were stripped from the  $\text{H}^-$  at the center of the minitandem and, after bending through a second magnet, the protons

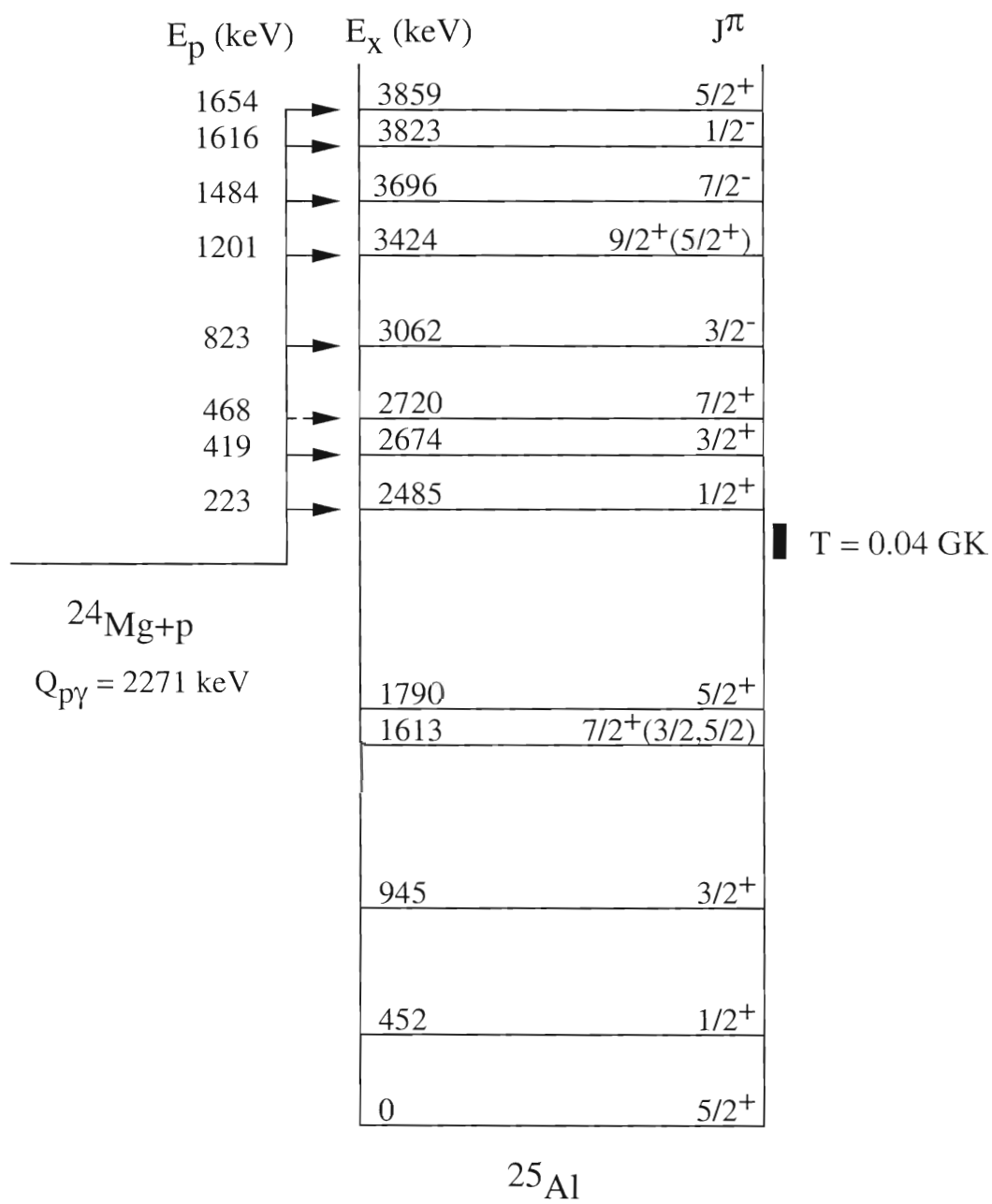


Figure 3.2: Energy level diagram for  $^{25}\text{Al}$ .

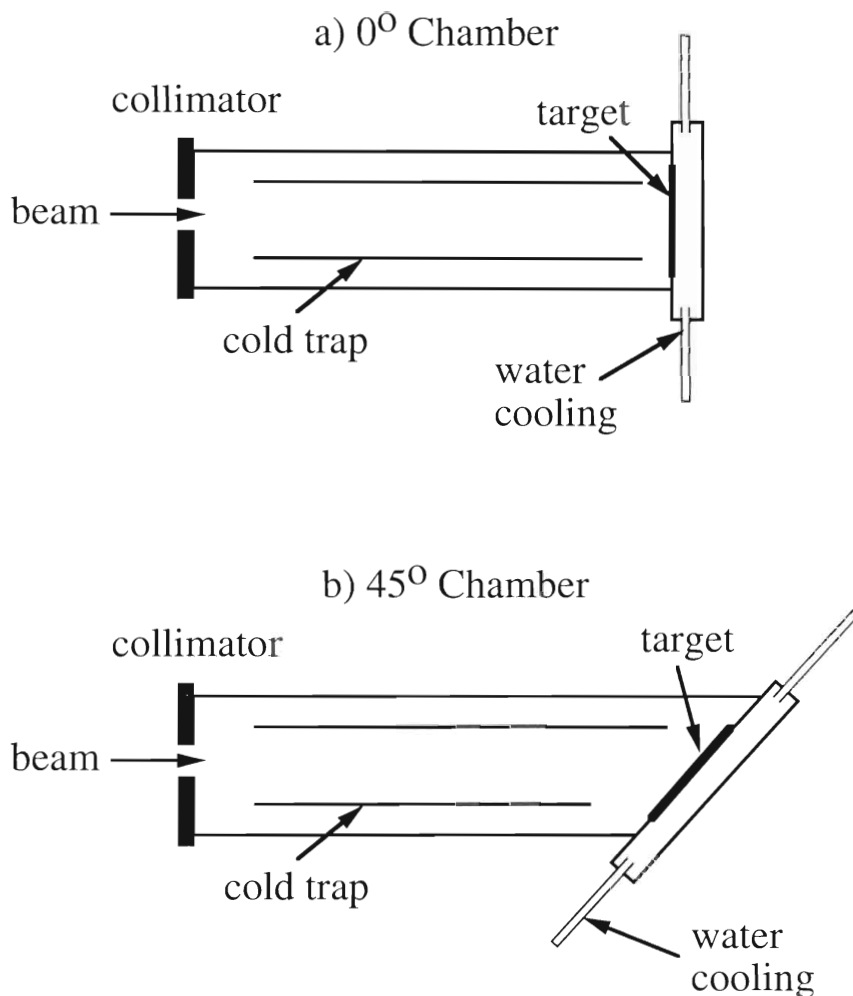


Figure 3.3: The  $0^\circ$  and  $45^\circ$  chambers used for a) determination of the mean lifetime (section 4.3) and b) determination of branching ratios.

were incident on the target (see figure 3.4). The experimental setup for the resonance strength measurement is shown in figure 3.5. The proton beam entered the chamber through a 3-mm-diameter collimator, passed through the transmission target and was incident on the opposite side of the chamber. A 100- $\mu\text{m}$ -thick ion-implanted charged-particle detector was placed at a distance of 7.8 cm with a 0.8-mm-diameter aperture and was used to measure the yield of backscattered protons. The angle of the charged-particle detector was changed from  $160^\circ$  to  $125^\circ$  for proton- and alpha-particle angular distribution measurements, but otherwise was fixed at  $155^\circ$ . A 128% or a 140% HPGe detector was placed in a close

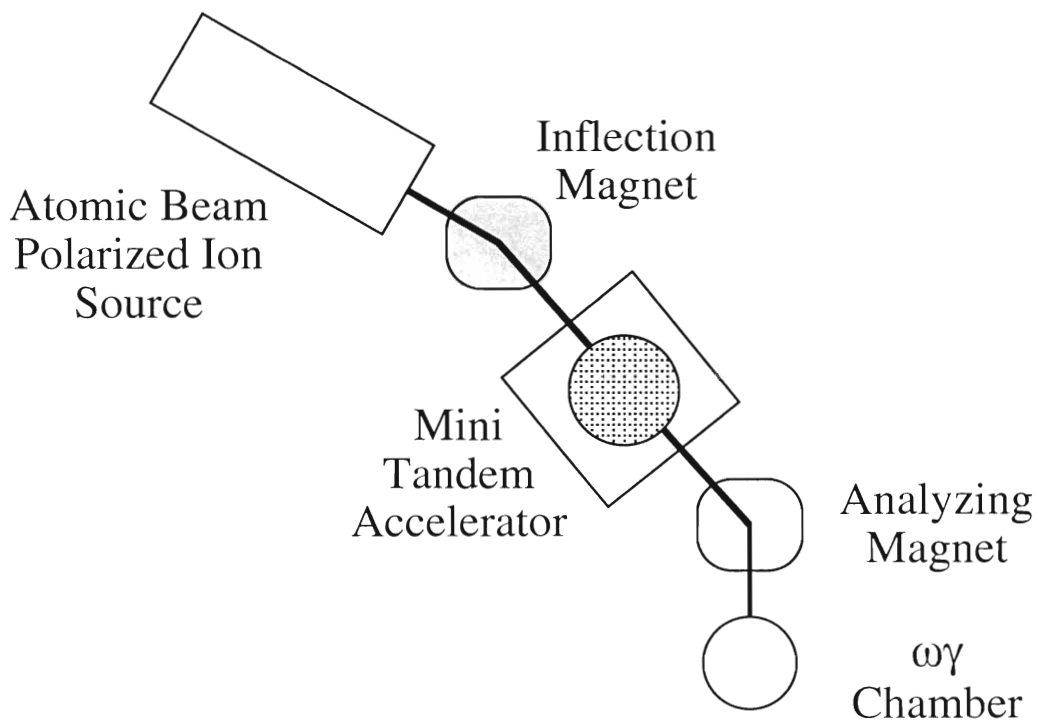


Figure 3.4: Diagram of the beam line used in the resonance strength determinations.

geometry and at an angle of  $125^\circ$ . The intensities of the protons were kept below 700 nA to prevent target deterioration and were typically  $> 200$  nA. The energy of the incident protons ranged from 200 to 480 keV.

On-line calibration of the incident proton energy was determined from the known source, minitandem, the Cs oven voltages, and from the thickness of the minitandem foils using the following expression

$$E_{final} = 2V_{mini} + V_{frame} + 2V_{Cs} - \Delta E_C \quad (3.1)$$

where  $E_{final}$  is the final energy of the protons,  $V_{mini}$  is the voltage of the minitandem,  $V_{frame}$  is the voltage on the frame of the source,  $V_{Cs}$  is the voltage of the cesium oven, and  $\Delta E_C$  is the energy loss of the protons through the minitandem carbon foils. Off-line, the energies of the incident protons were determined from well established  $(p, \gamma)$  yield curves and expressed in terms of the location of the backscattered proton peaks in the charged-particle detector. Gain stability was

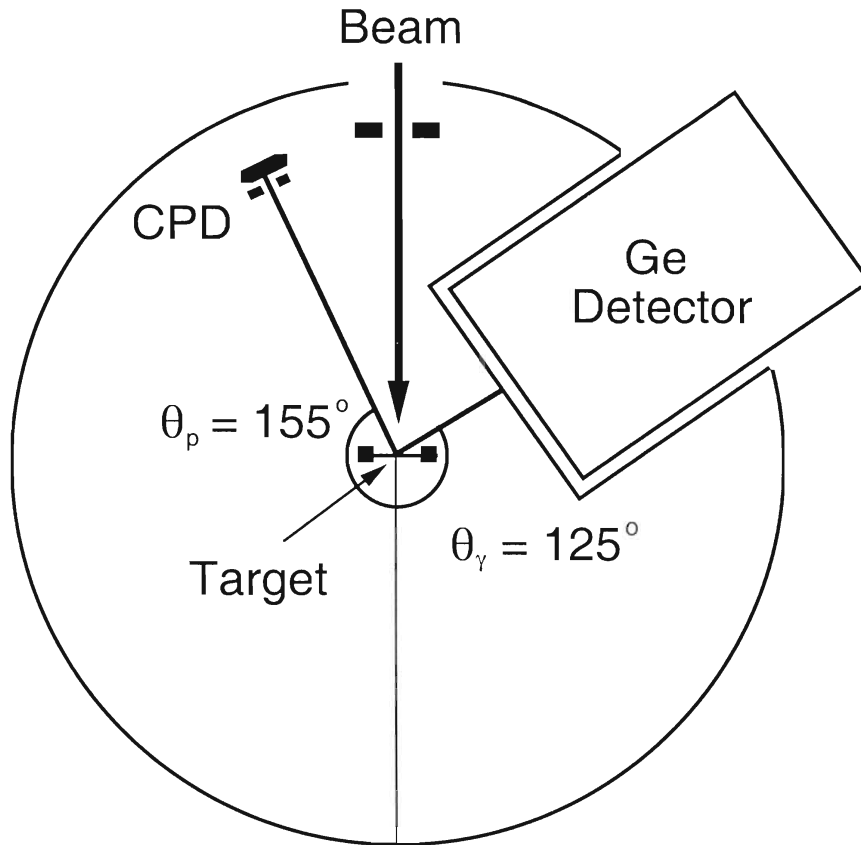


Figure 3.5: Schematic of the scattering chamber used in the determination of the resonance strengths.

monitored using a precision pulse generator and no significant excursions were observed.

The Mg targets were fabricated by evaporating Mg metal onto the underside of  $20\text{-}\mu\text{g}/\text{cm}^2$  carbon foils. The Mg would rarely adhere to the top of the foils during evaporation, and presumably stuck to the underside of the foils owing to the presence of leftover detergents used to release the carbon from its glass slide. The Al targets were fabricated by evaporation of Al metal onto  $20\text{-}\mu\text{g}/\text{cm}^2$  carbon foils. The targets were typically  $\approx 4\text{-}6$  keV thick at beam energies of  $E_p = 400$  keV. The thickness was chosen so that the energy loss through the target was larger than the resolution of the beam and that the Rutherford cross section and effective stopping power varied little over the thickness of the target.

For the determination of resonant branching ratios, a setup similar to the one described in section 3.1.1 (using the chamber shown in figure 3.3 b) was used. Protons passing through the minitandem were incident on a Mg or Al target evaporated onto a 0.5-mm-thick Ta backing. A 7-mm-diameter collimator was used to limit the size of the beam spot on target. A 140% HPGe detector was placed  $\sim 5$  cm from the target location at an angle of  $125^\circ$  with respect to the incident proton beam direction. Beam intensities were typically less than  $6 \mu\text{A}$  and the targets were less than 20 keV thick at  $E_p = 400$  keV.

### 3.1.3 Mean Lifetimes

The lifetime measurement also took place at the High Resolution Laboratory (HRL) at the Triangle Universities Nuclear Laboratory with the chamber shown in figure 3.3 a. For the lifetime measurement, protons at an energy of 1620 keV and 1654 keV were incident on the target with an intensity of approximately  $7 \mu\text{A}$  and a total charge of 1.0 C and 0.48 C, respectively. The beam was collimated to a 4 mm diameter spot on the target.

Three 60% HPGe detectors were placed at angles of  $2 \pm 3^\circ$ ,  $90 \pm 3^\circ$  and  $141 \pm 3^\circ$  with respect to the incident beam direction (see figure 3.6). The angles of the detectors were determined from the location of the detector and the small offset of the beam spot from the center of the target. The distances of the detectors were 8.1 cm, 7.8 cm and 10.1 cm from the target, respectively.

The target used in the lifetime measurement was fabricated using the ion implanter located at the University of North Carolina at Chapel Hill (see figure 3.7). Natural Mg metal was evaporated in the source of the ion implanter and mass selected for  $A=24$  ions. The  $^{24}\text{Mg}^+$  ions were accelerated to 100 keV and rastered to uniformly distribute the  $^{24}\text{Mg}^+$  ions on an etched [Gie92] 0.5-mm-thick Ta backing (see figure 3.7). The chamber shown in figure 3.3 a was used for the implantation of the Mg ions into Ta. A dose of 1.62 C of  $^{24}\text{Mg}^+$  ions was accumulated over an area of  $3.8 \text{ cm}^2$  in the backing.

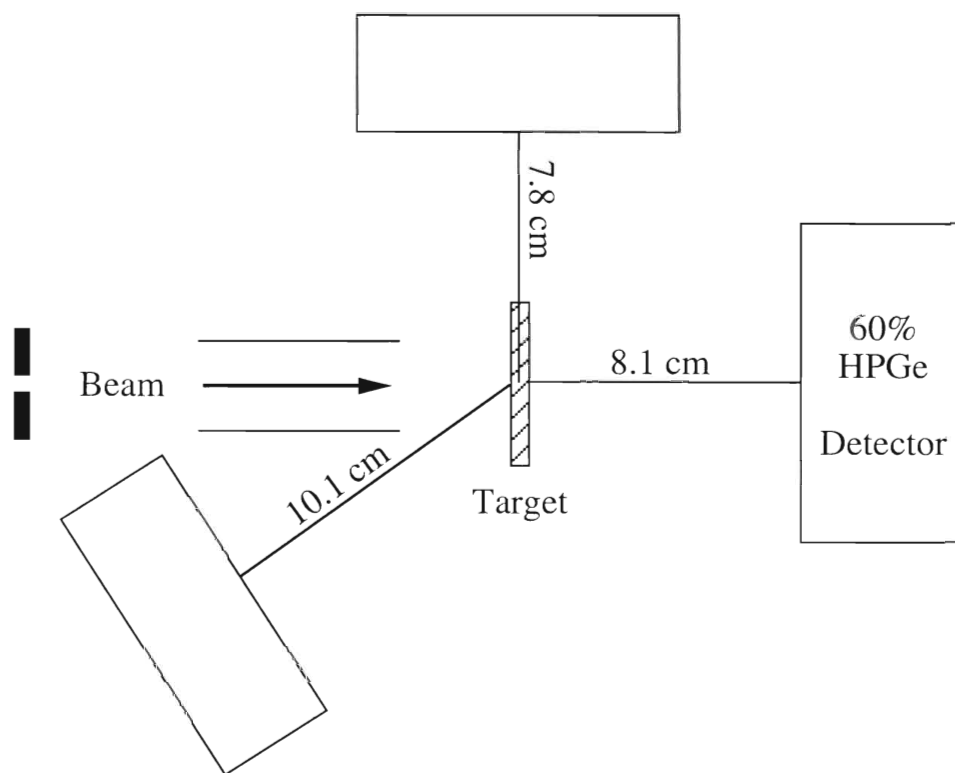


Figure 3.6: The experimental setup used for the determination of the lifetimes of the  $E_x = 2485$ - and  $2674$ -keV states.

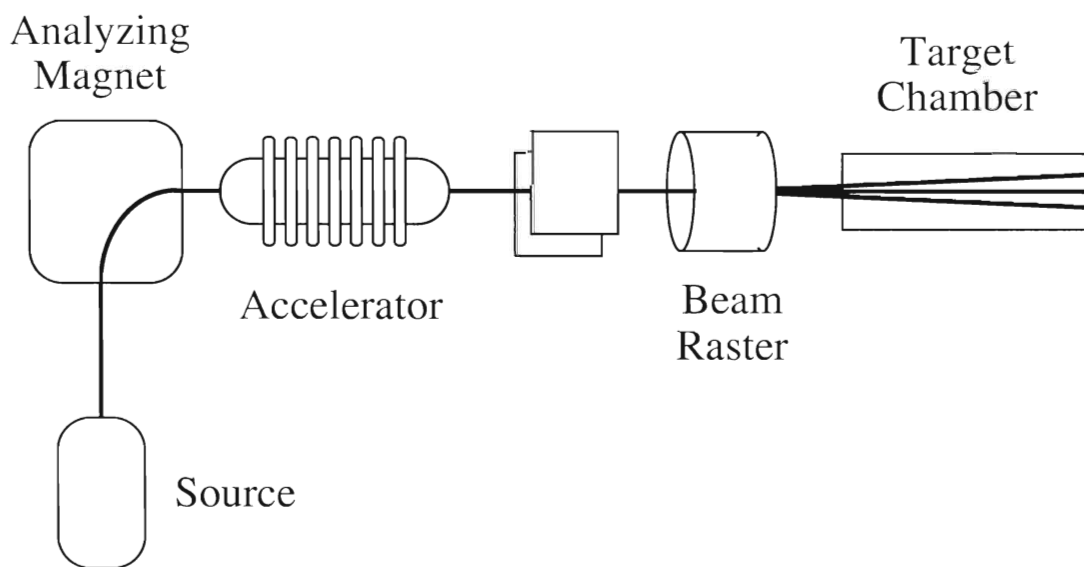


Figure 3.7: Schematic of the ion implanter located at the University of North Carolina at Chapel Hill, used to make the Mg implanted into Ta targets for the lifetime determinations.



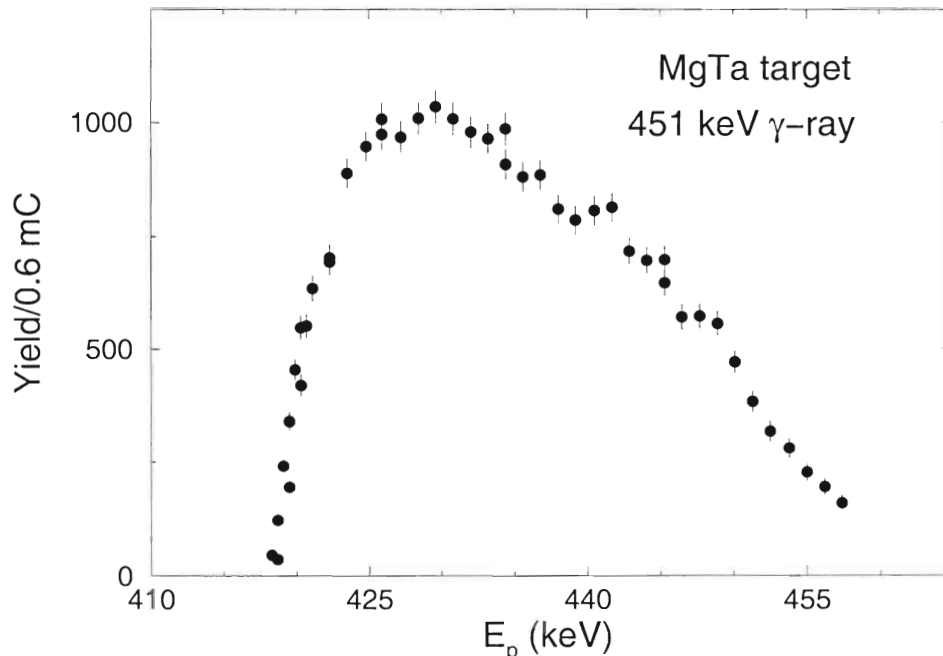


Figure 3.8: The yield curve taken at the  $E_R = 419$ -keV resonance in the  $^{24}\text{Mg}(p, \gamma)^{25}\text{Al}$  reaction, from which the stoichiometry of the target is determined.

The etching process was performed to remove surface contaminants from the Ta backing (such as boron or carbon). A recipe of 50 ml of 95%  $\text{H}_2\text{SO}_4$ , 20 ml of 70%  $\text{HNO}_3$  and 20 ml of 48% HF in a plastic beaker (glass will also be etched by this) was used to etch the Ta. The Ta backings were submerged for approximately 60 seconds in the solution, rinsed in distilled water, and resubmerged if desired. The etching process was continued until the Ta surfaces were smooth and highly reflective. Finally the Ta blanks were cleaned with alcohol and outgassed via resistive heating in an evaporator until they were red hot.

The stoichiometry of the target was determined from resonance strength measurements (see chapter 4.2) using the  $E_R = 419$ - and 1654-keV resonances in the  $^{24}\text{Mg}(p, \gamma)^{25}\text{Al}$  reaction. The effective stopping power can be determined from the maximum height of the yield curve (see figure 3.8 and equation 4.4). For this

target the effective stopping power is given by [Rol88]

$$\epsilon = \epsilon_{Mg} + \frac{N_{Ta}}{N_{Mg}} \epsilon_{Ta}, \quad (3.2)$$

where  $\epsilon_{Mg}$  is the stopping power of protons in Mg,  $\epsilon_{Ta}$  is the stopping power of protons in Ta, and  $N_{Ta}/N_{Mg}$  is the ratio of Ta to Mg atoms in the target. The resonance strength value for the  $E_R = 419$ -keV resonance was taken from table 4.7 and a value of  $\omega\gamma = 190 \pm 30$  meV from [Tra75b] was used for the  $E_R = 1654$ -keV resonance<sup>3</sup>. The stopping powers of protons in Mg and Ta were calculated with the program TRIM [Zie80]. The ratio  $N_{Ta}/N_{Mg}$  was determined to be  $0.3 \pm 0.1$ . The effective density of the target was calculated from the measured stoichiometry, the density of Ta, and the density of Mg, assuming the Mg atoms replaced Ta atoms in the target [Kei83] one-for-one, and yielded a value of  $\rho = 4.6$  g/cm<sup>3</sup>.

## 3.2 Detectors

### 3.2.1 Efficiency

Summing corrections to the intensities of the observed peaks were necessary for the branching ratio and resonance strength measurements as a result of the close proximity of the HPGe detector to the target. Summing effects result when two sequential  $\gamma$ -rays in a decay are detected within the time resolution of the detector, and are therefore processed as one  $\gamma$ -ray with an energy equivalent to the sum of the two original  $\gamma$ -rays [Deb88]. This effect can lead to increases (summing in) or decreases (summing out) in the observed intensity.

Summing corrections are dependent on the photopeak efficiency and the total efficiency of the detector. The photopeak efficiency  $\epsilon$  represents the probability

---

<sup>3</sup>A renormalization of the results of [Tra75b] was made in chapter 5 to match the presently determined values. The values quoted in [Tra75b] are consistent within errors with the renormalized values.

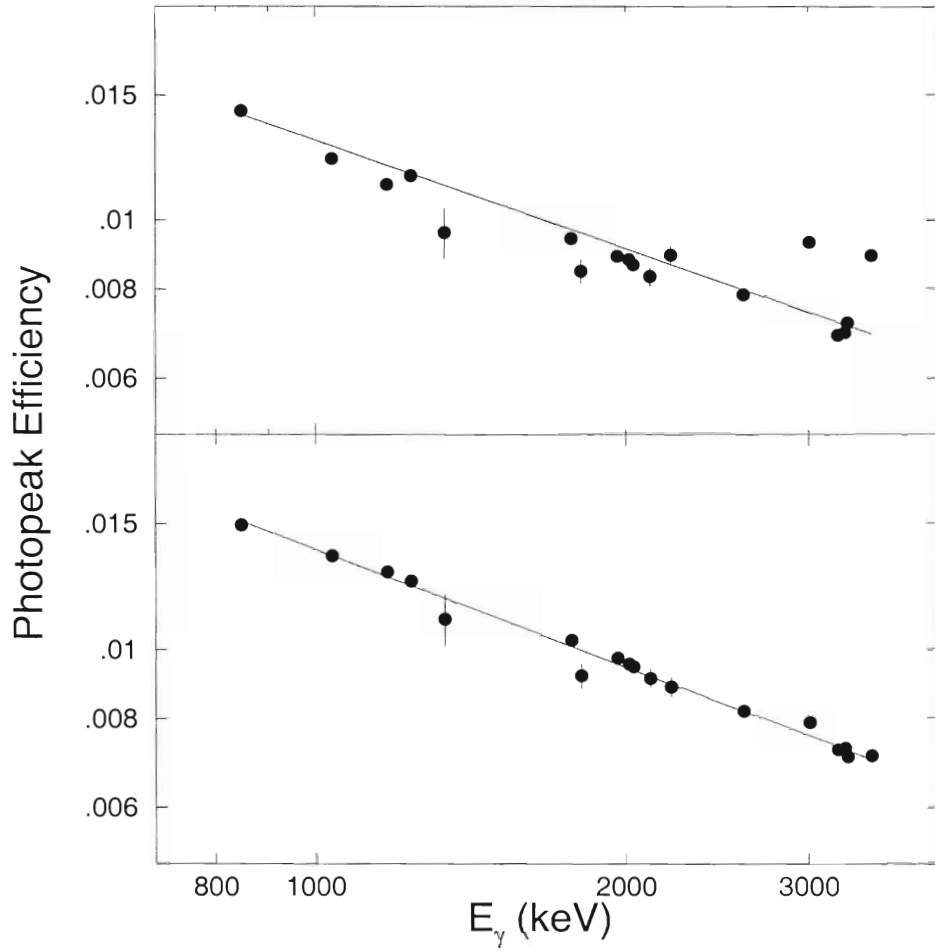


Figure 3.9: The relative photopeak efficiency of the 140% detector before summing corrections were applied (*top*) and after (*bottom*).

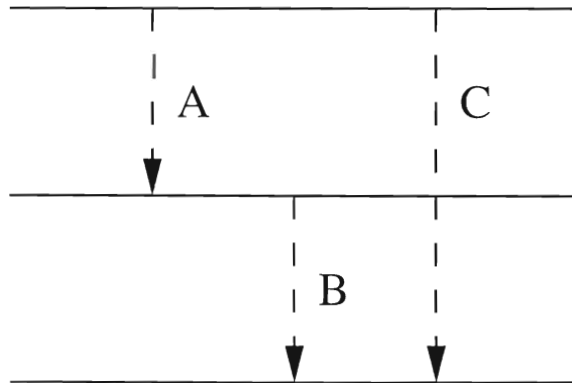


Figure 3.10: A simple decay scheme of a nucleus that emits  $\gamma$ -rays A, B, and C.

that an incident  $\gamma$ -ray will be fully absorbed in the detector. The total efficiency  $\varepsilon_t$  represents the probability that an incident  $\gamma$ -ray will be detected via the photoelectric effect, Compton effect, pair production, or scattering of the  $\gamma$ -ray into the detector. By placing calibrated  $^{60}\text{Co}$  and  $^{137}\text{Cs}$  sources at the target location (at a detector-to-target distance of  $\sim 6$  cm) the total efficiency was measured to be  $\varepsilon_t = 3.59 \times 10^{-2}$  at  $E_\gamma = 1253$  keV and  $\varepsilon_t = 6.25 \times 10^{-2}$  at  $E_\gamma = 662$  keV.

To determine the photopeak efficiency a calibrated  $^{56}\text{Co}$  source, which emits a multitude of low-energy  $\gamma$ -rays, was placed at the target location. The number of  $\gamma$ -rays observed in the photopeak relative to the number of emitted  $\gamma$ -rays [Wan88] is shown in figure 3.9 (*top*). The curve fit to the data uses the expected energy dependence of the photopeak efficiency [Deb88] and yields a photopeak efficiency of  $\varepsilon = 0.427E^{-0.506}$  where  $E$  is the  $\gamma$ -ray energy in keV. The scatter of the data points about the solid line is a consequence of summing.

For the simple decay scheme shown in figure 3.10, corrections ( $C$ ) to the intensities of the three peaks would proceed as follows:

$$C(A) = \frac{1}{1 - \varepsilon_t(B)}, \quad C(B) = \frac{1}{1 - \varepsilon_t(A)}, \quad \text{and} \quad C(C) = \frac{1}{1 + \varepsilon(A)\varepsilon(B)}. \quad (3.3)$$

The photopeak efficiency and the total efficiency (with 5% and 16% errors respectively) were used to correct the  $^{56}\text{Co}$  data for summing and the results are shown in figure 3.9 (*bottom*). The fit to the sum-corrected data yields a photopeak efficiency of  $\varepsilon = 0.604E^{-0.547}$ . Summing corrections have been applied to all branching ratio and resonance strength data.

An accurate knowledge of the ratio of the charged-particle detector to the HPGe detector efficiencies,  $\Omega_{cm}/\varepsilon_\gamma$ , is essential to the accurate determination of resonance strengths. Two HPGe detectors were used during these runs. For the  $^{24}\text{Mg}(p, \gamma)^{25}\text{Al}$  runs the large 140% HPGe detector was placed at a distance of 13 cm and an angle of  $125^\circ$ . Because of geometric constraints, the 140% detector could not be moved any closer to the target. The resonance strength runs for

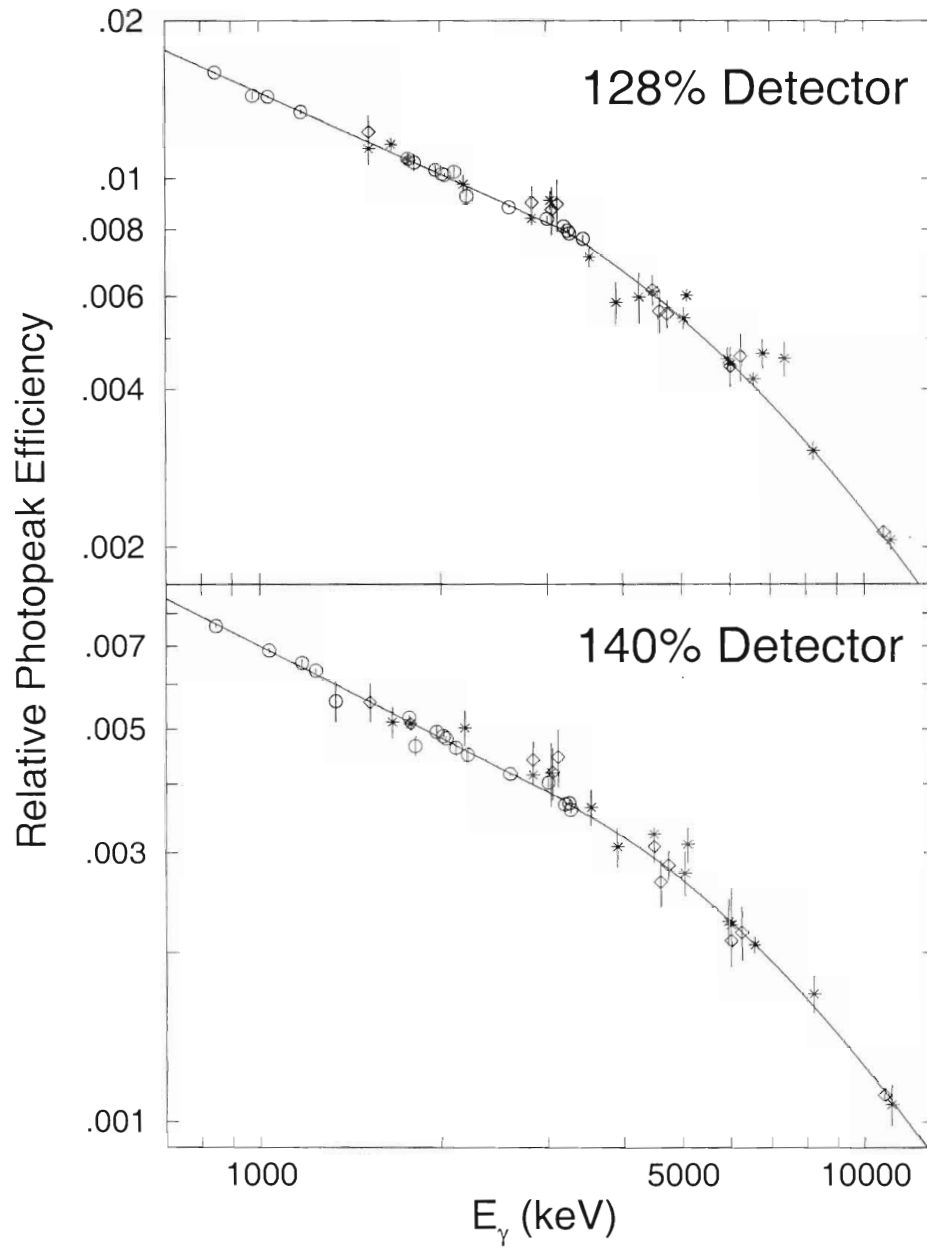


Figure 3.11: The relative photopeak efficiencies of the two HPGe detectors. The open circles correspond to data from the decay of  $^{56}\text{Co}$  and the stars and diamonds correspond to the  $E_R = 1317$ - and  $992$ -keV resonances in the  $^{27}\text{Al}(p, \gamma)^{28}\text{Si}$  reaction, respectively.

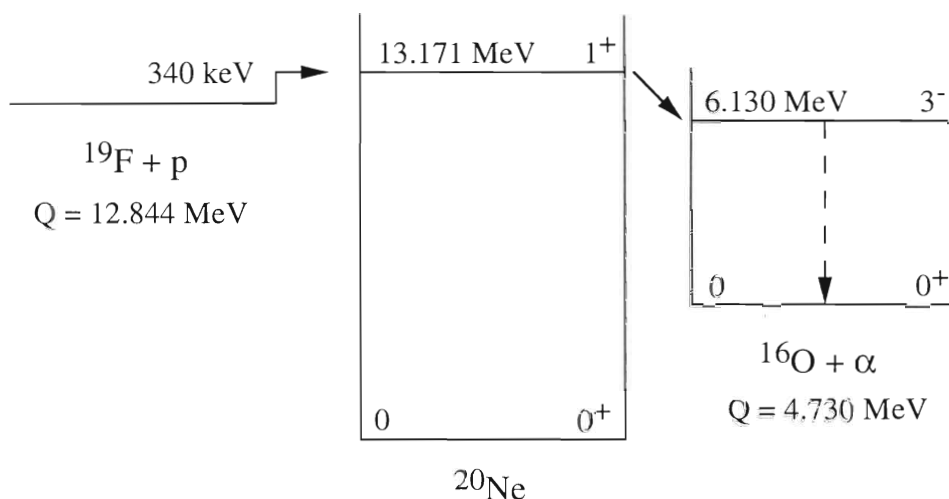


Figure 3.12: The energy level diagram for the  $^{19}\text{F}(p, \alpha_2 \gamma)^{16}\text{O}$  reaction with only the states of interest shown.

the other Mg isotopes and the Al run took place with a smaller 128% HPGe detector located at a distance of 7 cm and an angle of  $125^\circ$ . The smaller detector was chosen because it could be moved closer to the target, resulting in a larger efficiency. The relative photopeak efficiency for both detectors was determined at the lower  $\gamma$ -ray energies with a  $^{56}\text{Co}$  source and at higher  $\gamma$ -ray energies with the  $E_R = 992$ - and  $1317$ -keV resonances in the  $^{27}\text{Al}(p, \gamma)^{28}\text{Si}$  reaction (see figure 3.11). The relative photopeak efficiencies of the two detectors were determined from the data and are given below.

128% detector :

$$\log(\varepsilon) = -0.30 - 0.519(\log E_\gamma) \text{ for } E_\gamma \leq 2370 \text{ keV}$$

$$\log(\varepsilon) = -3.6 + 0.21(\log E_\gamma) + 0.48(\log E_\gamma)^2 - 0.12(\log E_\gamma)^3 \text{ for } E_\gamma \geq 2370 \text{ keV}$$

140% detector :

$$\log(\varepsilon) = -0.55 - 0.540(\log E_\gamma) \text{ for } E_\gamma \leq 2800 \text{ keV}$$

$$\log(\varepsilon) = -3.6 - 0.07(\log E_\gamma) + 0.53(\log E_\gamma)^2 - 0.12(\log E_\gamma)^3 \text{ for } E_\gamma \geq 2800 \text{ keV}$$

Owing to the large systematic uncertainties that could arise from the determination of the absolute charged-particle detector solid angle relative to the

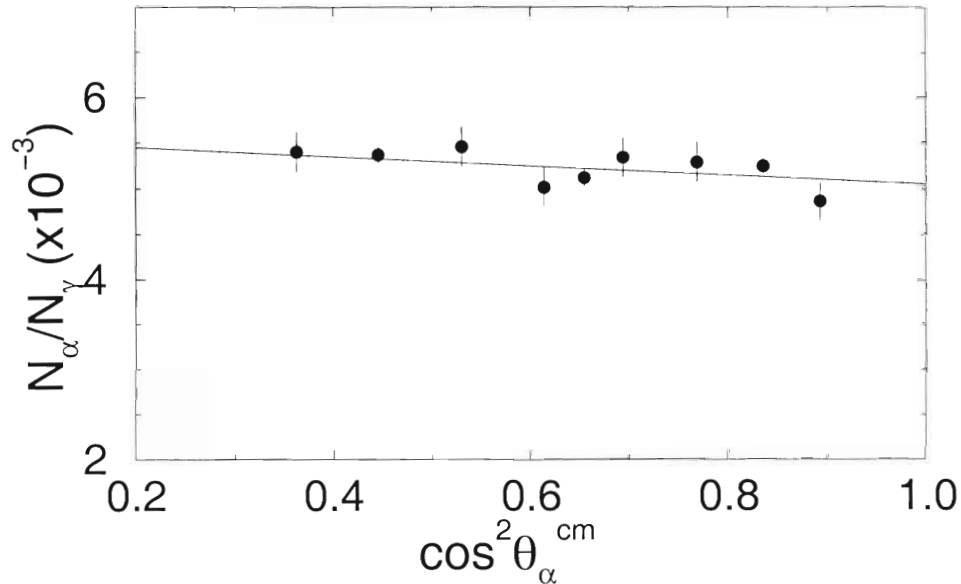


Figure 3.13: The angular distribution of  $\alpha_2$ -particles emitted in the  $^{19}\text{F}(p, \alpha_2\gamma)^{16}\text{O}$  reaction. The intensity of  $\alpha_2$ 's (cm) normalized to the intensity of 6.13-MeV  $\gamma$ -rays observed at  $125^\circ$  are plotted as a function of the charged-particle detector angle (cm). The angular distribution corresponds to a coefficient of  $a_2 = -0.06 \pm 0.03$ .

absolute HPGe detector efficiency, the  $^{19}\text{F}(p, \alpha_2\gamma)^{16}\text{O}$  reaction (see figure 3.12) was chosen to determine the ratio of the two detector efficiencies. At an incident proton energy of  $E_p = 340$  keV, this reaction produces one  $\alpha_2$ -particle for every 6130-keV  $\gamma$ -ray. In addition, the angular distribution of  $\alpha_2$ -particles was determined by varying the angle of the charged particle detector from  $125^\circ$  to  $160^\circ$  and normalizing the number of observed  $\alpha_2$ 's to the number of  $\gamma$ -rays detected at  $125^\circ$ . The angular distribution of  $\gamma$ -rays emitted from the  $^{19}\text{F}(p, \alpha_2\gamma)^{16}\text{O}$  reaction is isotropic [Dev49, Bec82, Cro91]. The angular distribution of  $\alpha_2$ -particles has the form  $1 + a_2 P_2 \cos \theta$  and a value of  $a_2$  was measured to be  $a_2 = -0.06 \pm 0.03$  as shown in figure 3.13<sup>4</sup>. Previous determinations of the angular distribution of  $\alpha_2$ -particles from the  $^{19}\text{F}(p, \alpha_2\gamma)^{16}\text{O}$  reaction are inconsistent. The angular distribution reported by [Van41] claimed an isotropic distribution, whereas [Bec82]

<sup>4</sup>The isotropy of the system was checked with an  $\alpha$ -particle emitting  $^{241}\text{Am}$  source placed at the target position

claim anisotropy with  $a_2 = 0.13 \pm 0.05$ . Note that the later study reports fewer data points than the present work. The present result was determined from  $\alpha_2$  intensities measured at nine angles with high precision and is therefore used in the determination of the relative detection efficiencies. The resulting efficiency ratios for the different geometries of the two HPGe detectors are  $\Omega_{lab}/\epsilon_\gamma$  (128% detector) =  $(2.346 \pm 0.062) \times 10^{-2}$  sr and  $\Omega_{lab}/\epsilon_\gamma$  (140% detector) =  $(4.255 \pm 0.201) \times 10^{-2}$  sr.

### 3.2.2 Energy Calibration

In order to determine the mean lifetime  $\tau$  of a state by the Doppler-shift-attenuation method, the energy of the observed  $\gamma$ -ray at each detector angle must be accurately measured. Consequently, gain shifts during the beam-on-target runs and calibration runs cannot be tolerated. The centroids of the K and Tl room background lines were monitored as a function of run number during the beam-on-target runs (shown in figure 3.14). The shifts in gain are negligible for our purposes. Small gain shifts were found between the calibration runs and the beam-on-target runs, but these were corrected off-line using the well-known room background lines. A  $^{56}\text{Co}$  calibration source was placed near the detectors before and after the data were taken, yielding a number of  $\gamma$ -rays in the energy region of interest. Figure 3.15 demonstrates the quality of a linear energy calibration during a  $^{56}\text{Co}$  run using the well known  $\gamma$ -ray energies from the decay of  $^{56}\text{Co}$  [Wan88]. The vertical axis is the ratio of the energies from the calibration divided by the quoted  $\gamma$ -ray energies. Included in the figure are the K and Tl room background  $\gamma$ -rays. The effect of scatter about the value of unity is negligible for our purposes.



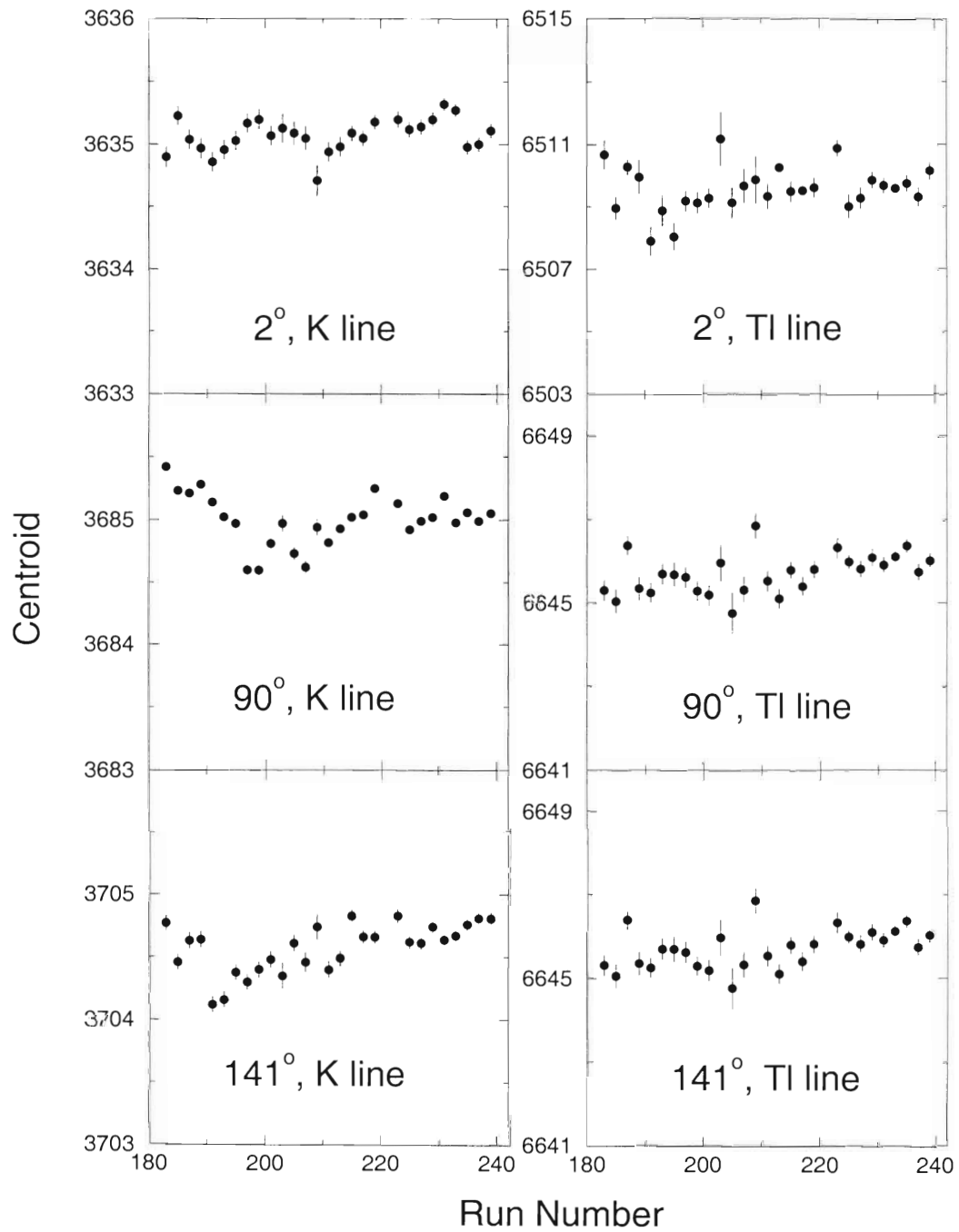


Figure 3.14: Centroid of the K and Tl lines as a function of run number for the runs summed to determine the Doppler shifted  $\gamma$ -rays of the  $E_x \approx 2485$ -keV state.

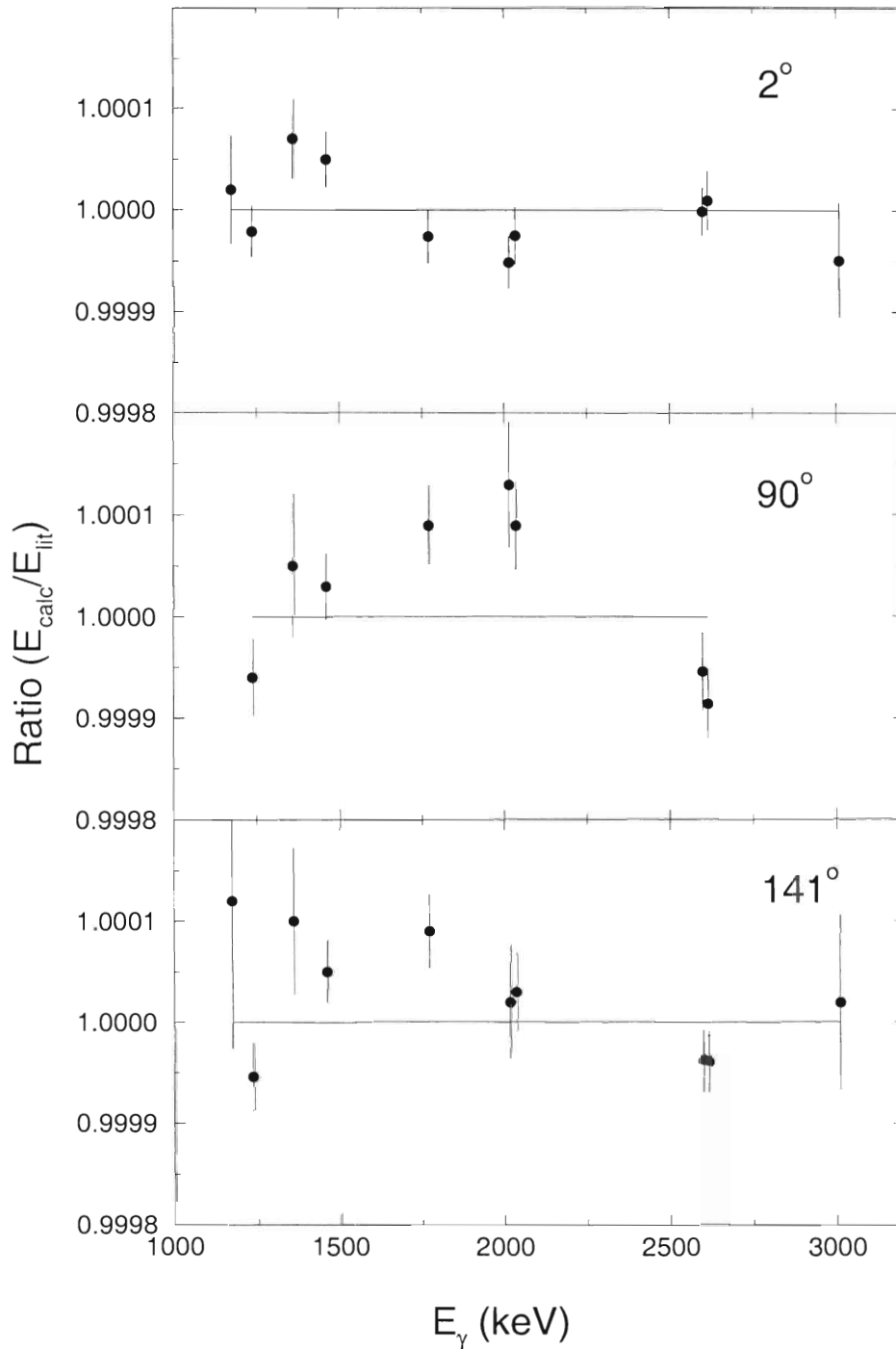


Figure 3.15: The ratio of the calculated  $\gamma$ -ray energy using a linear fit to the lines produced in the decay of  $^{56}\text{Co}$  and room background lines from K and Tl normalized to the quoted  $\gamma$ -ray energies for detectors at  $2^\circ$  (top),  $90^\circ$  (center) and  $141^\circ$  (bottom).

# Chapter 4

## Experimental Procedures and Results

### 4.1 Branching Ratios

The branching ratio measurement for the  $E_x = 2485$ -keV state took place with a proton energy of  $E_p = 1616$  keV. The  $E_R = 1616$ -keV resonance in  $^{24}\text{Mg}(p, \gamma)^{25}\text{Al}$  decays to the  $E_x = 2485$ -keV state in  $^{25}\text{Al}$  (see figure 3.2) and the value for  $\Gamma_\gamma/\Gamma$  was determined by monitoring the number of times the state of interest decayed via  $\gamma$ -emission ( $\sum_i I_{\gamma,i}^{decay}$ ) with respect to the total number of  $\gamma$ -rays that populated ( $I_\gamma^{feeding}$ ) the state of interest, i.e.

$$\frac{\Gamma_\gamma}{\Gamma} = \frac{\sum_i I_{\gamma,i}^{decay}}{I_\gamma^{feeding}}. \quad (4.1)$$

Similarly, the value for  $\Gamma_\gamma/\Gamma$  for the  $E_x = 2674$ -keV state was determined from populating the  $E_R = 1654$ -keV resonance. Figure 4.1 shows a section of the  $\gamma$ -ray spectrum used to determine the value  $\Gamma_\gamma/\Gamma$  for the 2485-keV state. Labeled are the  $\gamma$ -rays that populated and decayed from the  $E_x = 2485$ -keV state ( $3823 \rightarrow 2485$  keV and  $2485 \rightarrow 945$  and  $451$  keV, respectively). In order to determine the value of  $\Gamma_\gamma/\Gamma$  for the  $E_x = 2485$ - and  $2674$ -keV states as well as resonant  $\gamma$ -ray branching ratios, the intensities of the peaks were corrected for the photopeak

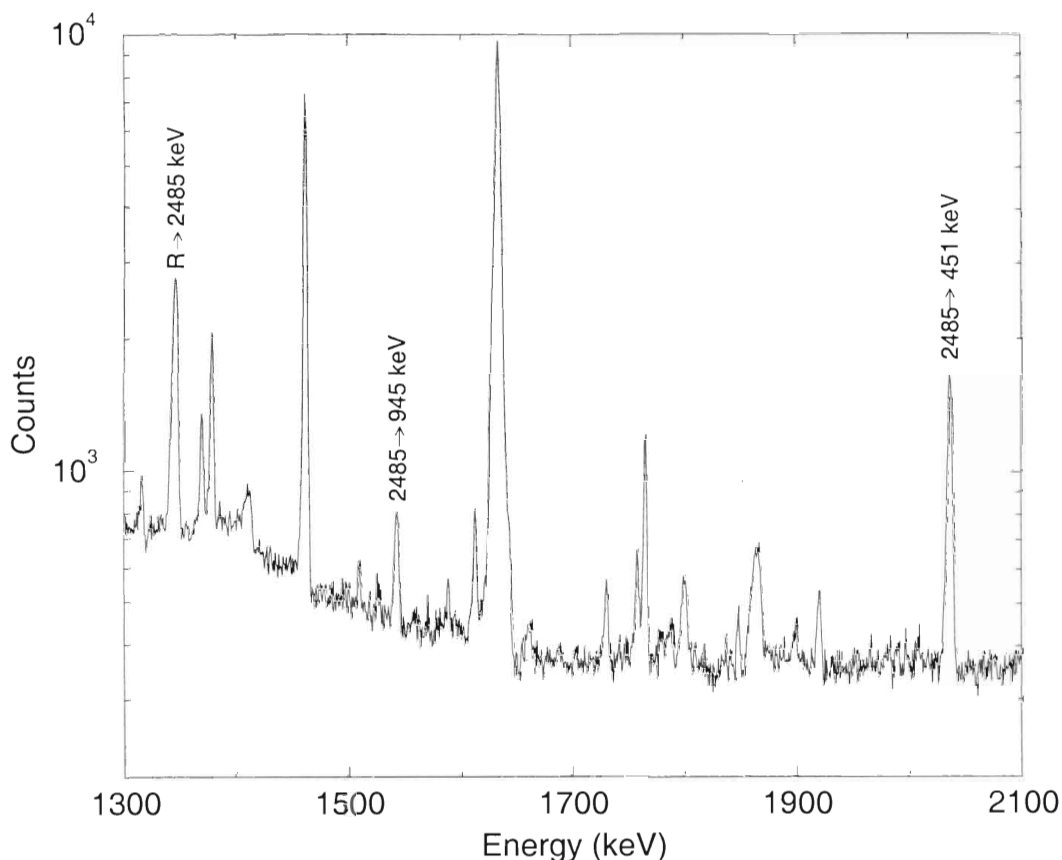


Figure 4.1:  $\gamma$ -ray spectrum highlighting the  $\gamma$ -rays of interest used to determine the value  $\Gamma_\gamma/\Gamma$  for the  $E_x = 2485$ -keV state.

efficiency of the detector (section 3.2.1), for summing effects (section 3.2.1), and for possible angular distribution effects (section 2.1).

The areas of the  $\gamma$ -ray peaks were determined with the peak fitting program GELIFT [Rad89]. A linear background was determined in the energy range of interest and peaks were assumed to have a Gaussian shape. When peaks overlapped with other peaks, the widths of the peaks were assumed to be equal. The GELIFT program returned values for the centroid, area, and width (and the corresponding errors) of the peaks as output.

The resonance  $\gamma$ -ray branching ratio resulting from the decay of a compound nuclear state is determined from the yield of  $\gamma$ -rays emitted for the particular transition of interest relative to the total number of  $\gamma$ -rays emitted from the

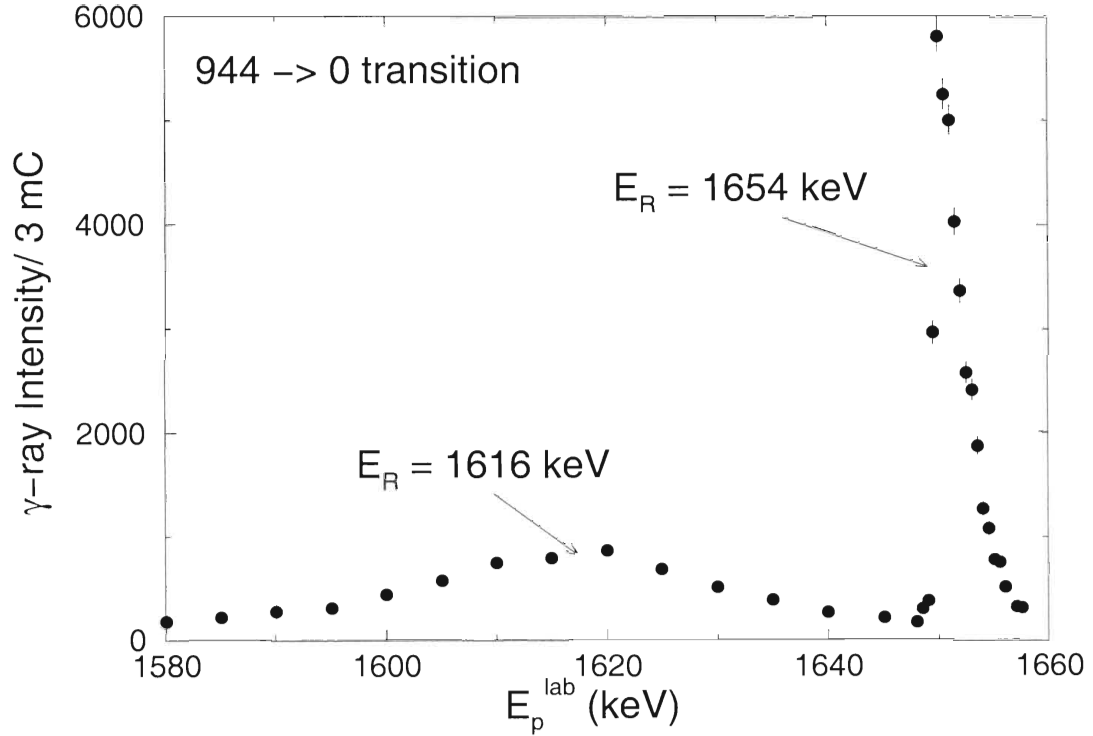


Figure 4.2: Yield curves of the  $E_R = 1616$ - and  $1654$ -keV resonances in  $^{24}\text{Mg}(p, \gamma)^{25}\text{Al}$ .

initial state. Therefore, the sum of all the  $\gamma$ -ray branching ratios for a particular state must be equal to 100%. In addition to the corrections mentioned previously, the intensities must also be corrected for contributions from direct capture and capture from other resonances.

Yield curves, or intensities of  $\gamma$ -rays as a function of the incident proton energy, were determined for both the  $E_R = 1616$ -keV and the  $E_R = 1654$ -keV resonances (see figure 4.2). The  $E_R = 1654$ -keV yield curve contains information about the target and beam [Gov59] since the target is much thicker than the width of the resonance ( $\sim 0.1$  keV [End90]). The target thickness as determined by the FWHM of the yield curve is approximately  $\xi = 3$  keV at  $E_p = 1654$  keV. The beam spread as determined by the 20-80% change in energy on the front edge of the yield curve [Gov59] corresponds to a width in the incident beam energy of approximately 0.5 keV. As seen in figure 4.2, there can exist contributions

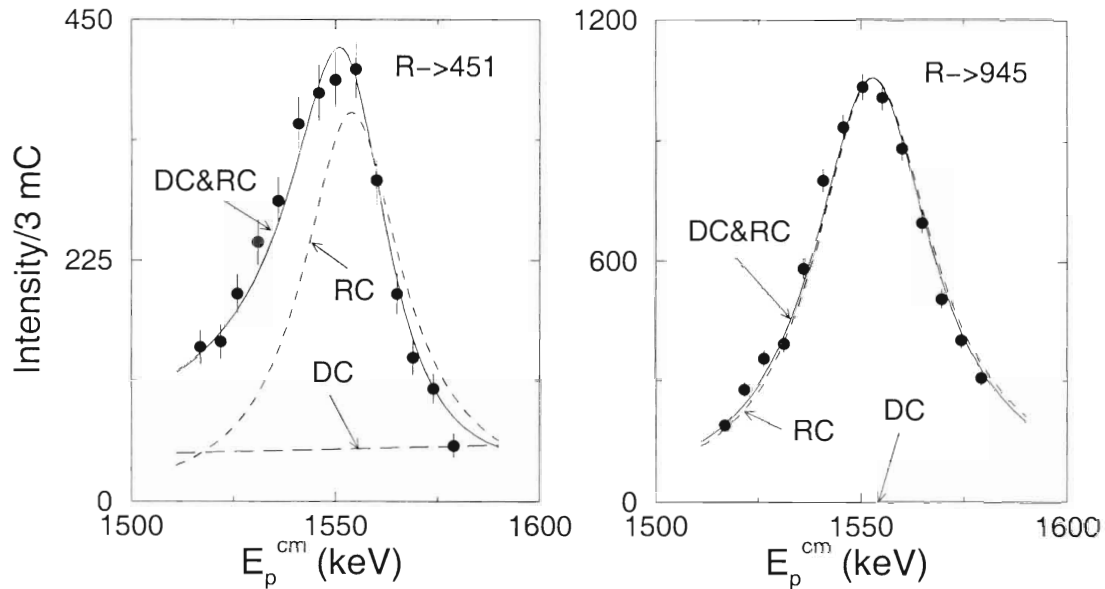


Figure 4.3: The yield curve data taken across the broad  $E_R = 1616$ -keV resonance for the transition to the first excited state (*left*) and to the second excited state (*right*) in  $^{25}\text{Al}$ . The long dashed curve is the direct capture component (negligible for the  $R \rightarrow 945$  transition), the short dashed curve is the resonance capture component, and the solid curve is the fit to the data resulting from the coherent superposition of the two capture processes.

to the  $\gamma$ -ray intensity observed at the  $E_R = 1654$ -keV resonance from the  $E_R = 1616$ -keV resonance. In addition, the direct capture contributes to the  $\gamma$ -ray yield for selected transitions to final states in  $^{25}\text{Al}$  [Tra75a], and therefore must be considered for the determination of primary  $\gamma$ -ray branching ratios.

The width of the  $E_R = 1616$ -keV resonance,  $\sim 36 \pm 7$  keV [End90], is much larger than the thickness of the target, therefore the shape of the yield curve is primarily determined by the cross section. Direct capture contributes to the  $\gamma$ -ray yield at the  $E_R = 1616$ -keV resonance for all of the primary decays [Tra75a]. A fit to the yield curve data for the  $E_R = 1616$ -keV resonance was performed using equation 2.4. The best fit was determined using a  $\chi^2$  minimization routine. The  $\chi^2$  is defined as follows [Bev92]

$$\chi^2 = \sum_{j=1}^n \frac{[Y(x_j) - Z(x_j)]^2}{\sigma_j(Z)^2} \quad (4.2)$$

where  $Y(x_j)$  is the fit to the data at  $x_j$ ,  $Z(x_j)$  is the value of the data at  $x_j$

Angular Distribution Effects

Transition	$a_4$ [Pii72]	$\sim  a_4 P_4 Q_4 $
3859 $\rightarrow$ 0 keV	-0.03	0.006
3859 $\rightarrow$ 945 keV	0.00	0.00
3859 $\rightarrow$ 1790 keV	-0.06	0.01
3859 $\rightarrow$ 2674 keV	0.10	0.02
3859 $\rightarrow$ 2720 keV	0.03	0.006

Table 4.1: Angular distribution effects for the  $E_R = 1654$ -keV resonance in  $^{24}\text{Mg}(p, \gamma)^{25}\text{Al}$ .

with an uncertainty of  $\sigma_j(Z)$ . The free parameters in the fit are the resonance energy (determined to be  $E_R = 1616.5 \pm 0.6$  keV), the width of the resonance (determined to be  $\Gamma = 35.8 \pm 0.8$  keV), and the normalizations of the two capture cross sections. Figure 4.3 shows the fit to the  $R \rightarrow 451$ -keV and the  $R \rightarrow 945$ -keV transitions and highlights the direct capture (DC) and resonance capture (RC) components. The direct capture contribution to the intensity of the  $R \rightarrow 945$  transition is negligible relative to resonance capture. As mentioned above, the  $\gamma$ -ray yield at the  $E_R = 1654$ -keV resonance also has contributions from direct capture and from the tail of the  $E_R = 1616$ -keV resonance. Therefore, the proper determination of the  $\gamma$ -ray branching ratios for the  $E_R = 1654$ -keV resonance requires a subtraction of these extraneous contributions.

Angular distribution effects must also be considered when determining  $\Gamma_\gamma/\Gamma$  and resonant  $\gamma$ -ray branching ratios (see equations 2.5 and 2.7). The resonance capture cross section is isotropic for capture to a  $J = 1/2$  state (i.e. the  $E_R = 1616$ -keV resonance). The direct capture angular distribution was determined by [Tra75a] and resulted in at most a  $P_2(\cos\theta)$  component. The detector was placed at  $55^\circ$  where  $P_2(\cos\theta) = 0$ , ensuring that no corrections were needed for direct capture angular distributions. The angular distribution for the  $\gamma$ -ray resulting from the  $3859 \rightarrow 2674$  keV transition was also considered. The  $J^\pi$

$\Gamma_\gamma/\Gamma$ values in $^{25}\text{Al}$		
$E_x$ (keV)	Present	Previous
2485 keV	$0.91 \pm 0.03$	
2674 keV	$0.125 \pm 0.008$	$0.12 \pm 0.02$ [Dwo72]

Table 4.2:  $\Gamma_\gamma/\Gamma$  values for the  $E_x = 2485$ -,  $2674$ - and  $2720$ -keV states in  $^{25}\text{Al}$ .

value of the  $E_x = 3859$ -keV feeding state is  $5/2^+$ . The detector was placed at  $55^\circ$  to eliminate the contributions from possible  $P_2(\cos\theta)$  terms in the angular distribution of the cross section. Contributions to the overall intensity resulting from  $P_4(\cos\theta)$  terms in the cross section were estimated from the  $a_4$  term given in reference [Pii72], and are listed in table 4.1. The contribution was corrected for the attenuation of the  $P_4(\cos\theta)$  component ( $Q_4 < 0.5$ ) caused by the large solid angle subtended by the HPGe detector.

After correcting for the photopeak efficiency and summing effects, a value of  $\Gamma_\gamma/\Gamma = 0.91 \pm 0.03$  was determined for the  $E_x = 2485$ -keV state and a value of  $\Gamma_\gamma/\Gamma = 0.125 \pm 0.008$  was determined for the  $E_x = 2674$ -keV state. The maximum effect resulting from an anisotropy of the uncorrected angular distribution on the yield for the  $3859 \rightarrow 2674$ -keV transition is 2% (see table 4.1). The  $\gamma$ -rays emitted from the decay of the  $E_x = 2674$ -keV state do not contain  $P_4(\cos\theta)$  terms, and therefore do not require angular distribution corrections. The final results are presented in table 4.2.

The branching ratios for the  $E_R = 1616$ - and  $1654$ -keV resonances are shown in table 4.3 for the present experiment and compared to the results in the literature. The maximum effect of the angular distribution on the yield (or branching ratios) of the  $E_R = 1654$ -keV resonance is  $\leq 2\%$ , and is therefore not reflected in the final results. The errors in the branching ratios result from the subtraction of the direct and resonance capture components to the yield ( $\leq 4\%$ ), the statistical uncertainty of the counts in the spectra ( $\leq 2\%$ ), the relative photopeak efficiency of the HPGe detector ( $\leq 2\%$ ), and summing corrections to the intensities ( $\leq 2\%$ ).



Branching Ratios in  $^{24}\text{Mg}(p, \gamma)^{25}\text{Al}$  (in %)

$E_R$ (keV)	Transition	Present	[Tik91]	[Ree69]	[Pii72]
1616 keV	R $\rightarrow$ 2485	$5.7 \pm 0.2$	$7 \pm 1$	$5 \pm 1$	$8 \pm 5$
	R $\rightarrow$ 945	$69.8 \pm 0.7$	$68 \pm 3$	$32 \pm 5$	$61 \pm 5$
	R $\rightarrow$ 451	$24.5 \pm 0.7$	$25 \pm 2$	$20 \pm 3$	$31 \pm 5$
1654 keV	R $\rightarrow$ 3062	$0.36 \pm 0.04$	$0.7 \pm 0.1$	$4.0 \pm 0.5$	
	R $\rightarrow$ 2720	$9.41 \pm 0.23$	$9.6 \pm 0.7$	$8 \pm 1$	$8 \pm 3$
	R $\rightarrow$ 2674	$7.90 \pm 0.12$	$9.0 \pm 0.7$	$10 \pm 1$	$9 \pm 3$
	R $\rightarrow$ 2485	$< 0.2$	$< 0.4$	$18 \pm 3$	
	R $\rightarrow$ 1790	$6.09 \pm 0.15$	$5.1 \pm 0.4$	$4.0 \pm 0.5$	$6 \pm 3$
	R $\rightarrow$ 1613	$1.93 \pm 0.06$	$2.4 \pm 0.3$	$8 \pm 1$	$2 \pm 2$
	R $\rightarrow$ 945	$63.8 \pm 1.3$	$66.8 \pm 3.5$	$28 \pm 4$	$63 \pm 4$
	R $\rightarrow$ 451	$0.40 \pm 0.04$		$2 \pm 0.3$	
	R $\rightarrow$ 0	$9.91 \pm 0.16$	$6.4 \pm 1.0$	$10 \pm 2$	$12 \pm 3$

Table 4.3: The branching ratios for the  $E_R = 1616$ - and  $1654$ -keV resonances in  $^{24}\text{Mg}(p, \gamma)^{25}\text{Al}$  for the present work and from the literature. Some states from the previous branching ratios are not listed because they resulted from other resonances. The present branching ratios were corrected for contributions resulting from direct capture or other resonances.

The final results are generally in agreement with the previous data.

## 4.2 Resonance Strengths

The discrepancies of factors of two or more in the literature values for resonance strengths motivated the use of a method whereby the systematic uncertainties would be reduced. Determinations of resonance strengths are generally carried out by either measuring the resonance strength *relative* to a known resonance or determining them *absolutely*. In most methods, absolute resonance strength determinations require knowledge of the target stoichiometry, the stop-

ping powers of the different target nuclei, total charge accumulated on target, and the absolute detector efficiency. These quantities are potential sources of systematic errors. The method outlined later in this section for the determination of absolute resonance strengths eliminated the above mentioned systematic uncertainties, yielding results that are more reliable.

The definition of a resonance strength was given in equation 1.1. The integral over the Breit-Wigner cross section (see equation 2.3) for a narrow resonance is proportional to the resonance strength

$$\int_0^{\infty} \sigma_{BW}(E) dE = 2\pi^2 \lambda_R^2 (\omega\gamma)_R \quad (4.3)$$

where  $\lambda_R$  is the wavelength of the incident particle at the resonance energy and  $(\omega\gamma)_R$  is the resonance strength at the resonance energy. The first step in obtaining a value for the resonance strength is a measurement of the  $(p, \gamma)$  yield curve. The height of the thick target yield curve is proportional to the strength of the resonance. The width of the yield curve is approximately equal to the thickness  $\xi$  of the target (since the resonance width is much smaller than the target thickness). The spread in the incident beam energy produces a sloped front edge to the yield curve and the straggling of the incident particles through the target and of the target nuclei into the backing are the predominate cause of the sloped back edge.

If the thickness of the target ( $\sim$  keV) is large compared to the width of the resonance ( $\sim$  eV) the  $\gamma$ -ray yield is directly proportional to  $\omega\gamma$  [Gov59]. Then

$$\omega\gamma = \frac{2Y_\gamma}{\lambda^2} \epsilon = \frac{2}{\lambda^2} \frac{Y_\gamma \xi}{n_t} = \frac{2}{\lambda^2} \frac{A}{n_t}, \quad (4.4)$$

where  $Y_\gamma$  is the maximum  $\gamma$ -ray yield,  $n_t$  is the number of target nuclei, and  $\epsilon$  is the effective stopping power of the target.  $A (= Y_\gamma \xi)$  is the integrated area under the  $(p, \gamma)$  yield curve.

The yield of elastically scattered protons for an incident bombarding energy  $E_b$  is given by

$$Y_{Ruth} = \int_{E_b-\xi}^{E_b} \frac{\sigma_{Ruth}(E)}{\epsilon(E)} dE \approx \sigma_{Ruth}(E_b) n_t, \quad (4.5)$$

when the Rutherford cross section  $\sigma_{Ruth}$  relative to the effective stopping power  $\epsilon$  changes little over the energy loss of the projectile in the target. Substitution of equation 4.5 into 4.4 leads to

$$\omega\gamma = \frac{2}{\lambda^2} A \frac{\sigma_{Ruth}}{Y_{Ruth}}, \quad (4.6)$$

which is independent of stopping powers, target stoichiometries, target uniformities and beam straggling [Gov59].

The area  $A$  under the  $(p, \gamma)$  yield curve is given experimentally as

$$A = \frac{1}{B_\gamma \epsilon_\gamma W_\gamma(\theta)} \int_0^\infty \frac{N_\gamma(E)}{N_p(E)} dE, \quad (4.7)$$

where  $N_\gamma$  is the number of observed  $\gamma$ -rays,  $B_\gamma$  is the branching ratio of the observed  $\gamma$ -ray,  $\epsilon_\gamma$  is the absolute photopeak efficiency of the HPGe detector,  $W_\gamma$  is the angular distribution of the emitted  $\gamma$ -rays, and  $N_p$  is the number of particles incident on the target. The Rutherford yield is written experimentally as

$$Y_{Ruth}(E) = \frac{N'_p(E)}{N_p(E) \Omega_{cm}}, \quad (4.8)$$

with  $N'_p$  the number of elastically scattered protons and  $\Omega_{cm}$  the solid angle of the charged-particle detector. Because the incident bombarding energy is much smaller than the Coulomb barrier, the yield of backscattered protons can properly be described by Rutherford scattering even at the resonance energies (as shown later in this chapter), which allows for the determination of the resonance strength relative to Rutherford scattering. Incorporating equations 4.7 and 4.8 into 4.6 yields

$$\omega\gamma = \frac{2}{\lambda^2} \frac{\Omega_{cm}}{B_\gamma \epsilon_\gamma W_\gamma(\theta)} \int \frac{N_\gamma(E)}{N'_p(E)} \sigma_{Ruth}(E) dE. \quad (4.9)$$

The determination of the different components of equation 4.9 and the resulting resonance strength values for the  $E_R = 223$ - and  $419$ -keV resonances in  $^{24}\text{Mg}(p, \gamma)^{25}\text{Al}$ ,  $E_R = 435$ -keV resonance in  $^{25}\text{Mg}(p, \gamma)^{26}\text{Al}$ ,  $E_R = 338$ - and  $454$ -keV resonances in  $^{26}\text{Mg}(p, \gamma)^{27}\text{Al}$ , and the  $E_R = 406$ -keV resonance in  $^{27}\text{Al}(p, \gamma)^{28}\text{Si}$  are discussed in this chapter.

Sample spectra for the  $^{24}\text{Mg}(p, \gamma)^{25}\text{Al}$  and the  $^{24}\text{Mg}(p, p)^{24}\text{Mg}$  reaction at  $E_p = 223$  keV are shown in figure 4.4. The strongest primary  $\gamma$ -ray used for the determination of the resonance strength and the fit to the charged-particle spectrum for the different target nuclei are indicated. Peaks in the charged-particle spectrum were fit using the GELIFT program assuming a Gaussian distribution. The Mg, O, and C peaks were easy to distinguish at the higher energies around  $E_p = 400$  keV (see figure 4.5) and calibrations regarding the location of the O peak and its width were determined and fixed at the lower energies. The quality of the fit to the low energy peaks was indicated by the close correspondence of the observed yield to that describing the Rutherford scattering. The  $\gamma$ -ray peaks were assigned a linear background fit with the XSYS data analysis routine [Sod87] and gates set around the region of interest determined the area of the peak. Only when  $\gamma$ -ray peaks overlapped were they fit using GELIFT.

Since the energy calibration of the incident particles was determined as a function of the peak location of the backscattered particles in the detector (see section 3.1.2), the carbon buildup on the front of the target created some difficulties. Incident protons would have to travel through the carbon layer after interacting with the target, resulting in a lower measured energy. This effect was noticed in the  $^{26}\text{Mg}(p, \gamma)^{27}\text{Al}$  reaction at  $E_R = 454$  keV as demonstrated in figure 4.6 (*left*). The data represented by the solid points were taken early in the experiment. After an additional 27 mC of beam was accumulated on target the front edge of the yield curve was reproduced yielding the open points. The observed shift in energy resulting from the carbon buildup was determined as a function of the charge accumulated on target and from the stopping powers of protons in carbon. Corrections for carbon buildup as a function of the beam accumulated on target were applied to all yield curves (see figure 4.6 (*right*)). The correction for the  $^{27}\text{Al}(p, \gamma)^{28}\text{Si}$  reaction is shown in figure 4.7, demonstrating that the source of the shift was correctly identified.

Since the spin  $J$  of the compound nuclear states in the  $E_R = 223$ -keV res-

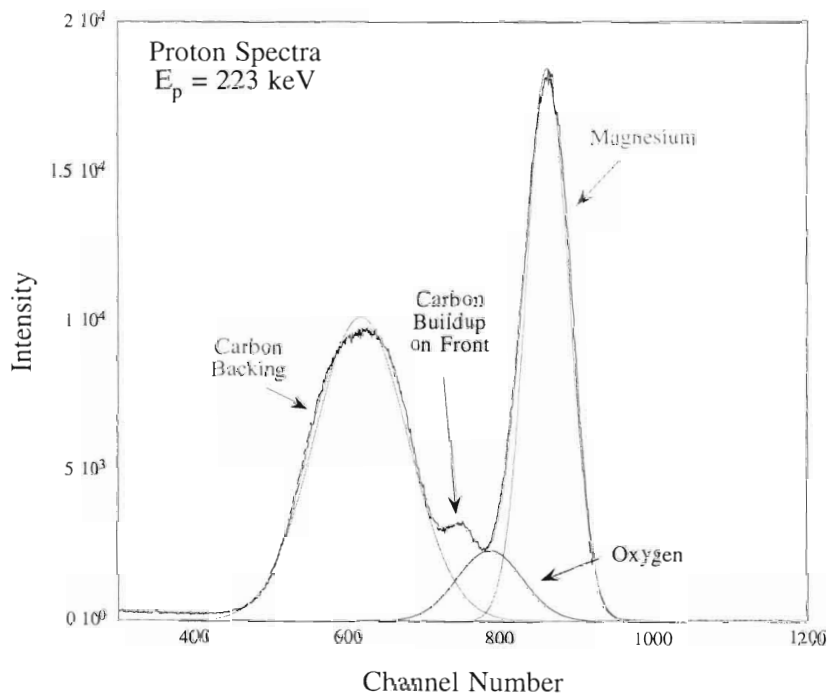
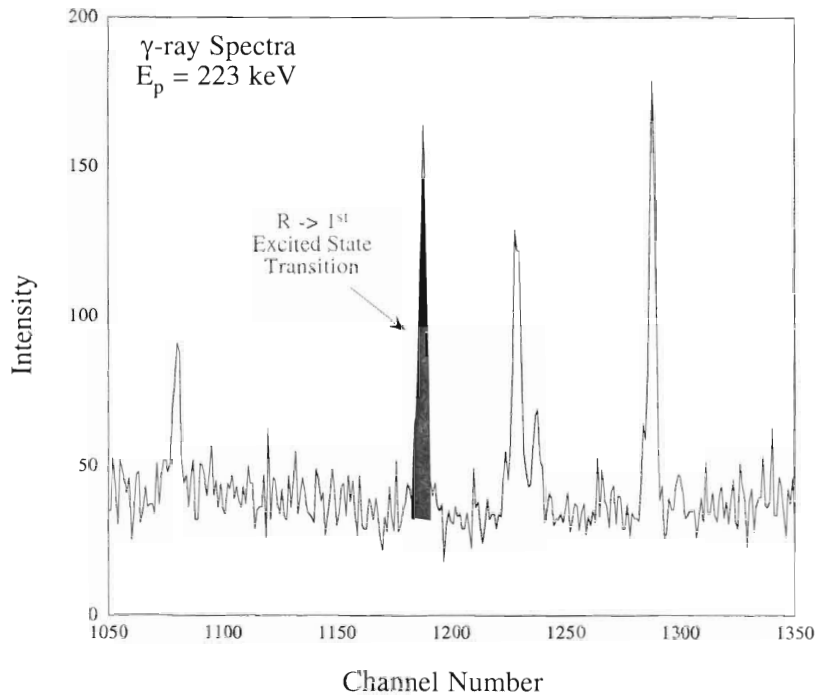


Figure 4.4:  $\gamma$ -ray spectrum highlighting the  $\gamma$ -ray used to create the yield curve and the backscattered proton spectrum showing the fits determined for separate target elements.

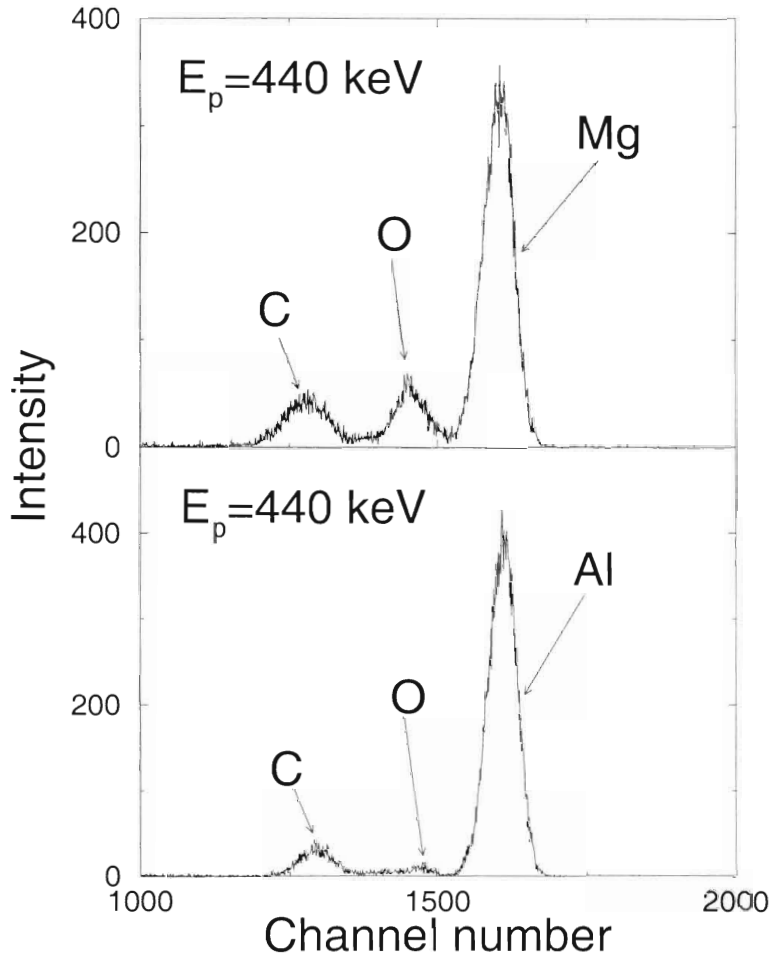


Figure 4.5: Elastically scattered protons from a Mg (*top*) and an Al (*bottom*) target.

onance in the  $^{24}\text{Mg}(p, \gamma)^{25}\text{Al}$  reaction and the  $E_R = 454\text{-keV}$  resonance in the  $^{26}\text{Mg}(p, \gamma)^{27}\text{Al}$  reaction are both  $1/2$ , the cross sections are isotropic, and no angular distribution effects need to be considered (refer to equations 2.5 and 2.7). The  $J$  of compound nuclear states corresponding to the  $E_R = 419\text{-keV}$  resonance in the  $^{24}\text{Mg}(p, \gamma)^{25}\text{Al}$  reaction and the  $E_R = 338\text{-keV}$  resonance in the  $^{26}\text{Mg}(p, \gamma)^{27}\text{Al}$  reaction are both  $3/2$ , having at most a  $P_2(\cos \theta)$  component in the angular distribution. Therefore, in order to reduce the angular distribution effects, the detector was placed at  $\theta = 125^\circ$ , where  $P_2(\cos \theta) = 0$ . The  $E_R = 435\text{-keV}$  resonance in the  $^{25}\text{Mg}(p, \gamma)^{26}\text{Al}$  reaction and the  $E_R = 406\text{-keV}$  res-

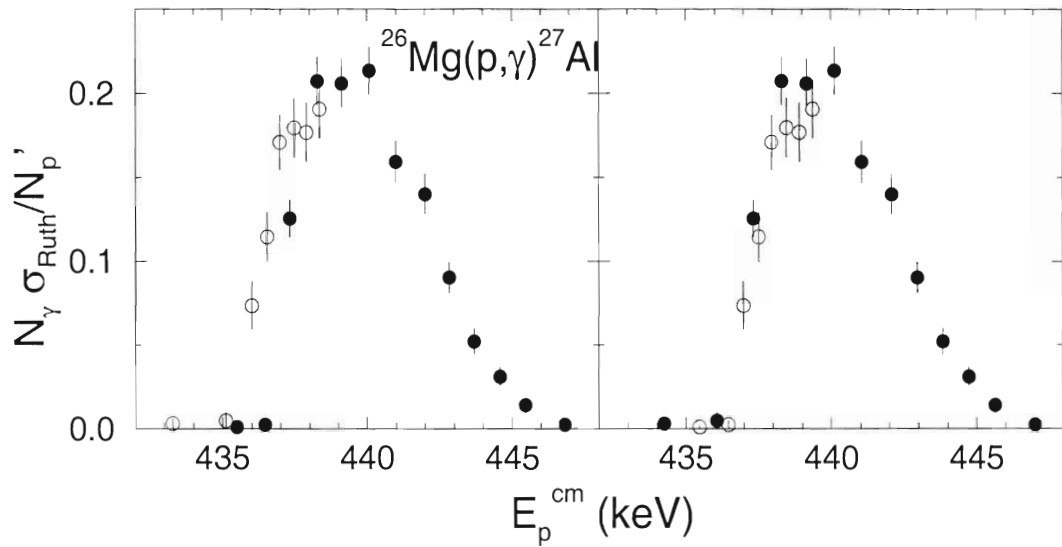


Figure 4.6: The solid points in the left plot are the yield curve data taken early in the experiment. After 27 mC of charge were accumulated on the target, the front edge of the yield curve was reproduced, yielding the open points. The observed shift was attributed to carbon buildup on the surface of the target. The resultant yield curve after correcting for the effect is shown to the right.

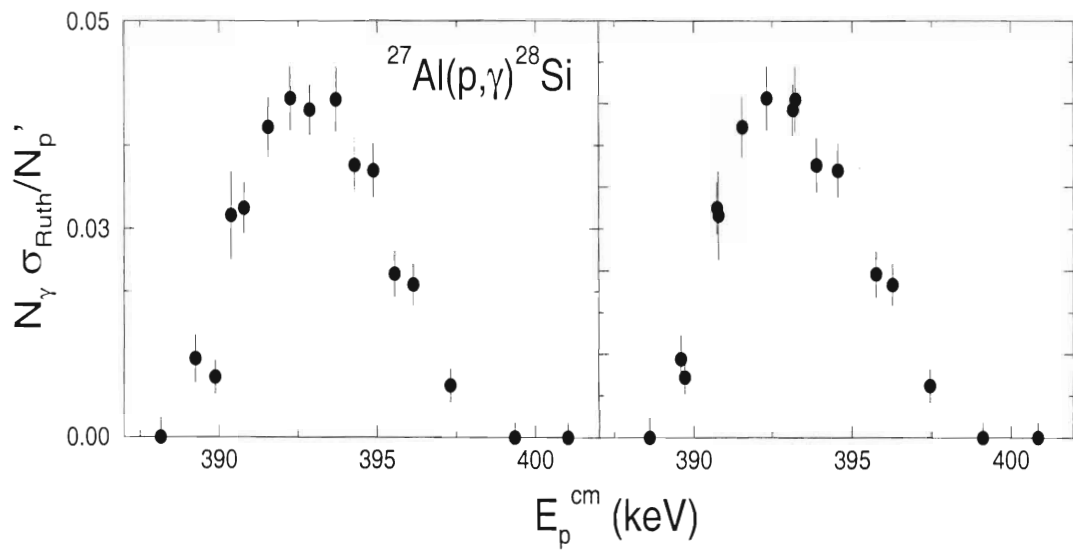


Figure 4.7: The yield curve of  $^{27}\text{Al}(p,\gamma)^{28}\text{Si}$  before correcting for carbon buildup (left) and after corrections were made (right).

onance in the  $^{27}\text{Al}(p, \gamma)^{28}\text{Si}$  reaction will predominantly proceed through  $l_i = 1$ , inferring an angular distribution up to  $P_2(\cos \theta)$ . The possible contributions resulting from  $P_4(\cos \theta)$  terms for the last two reactions are expected to be less than a few percent [Ili90], and are therefore not considered in the determination of the resonance strengths or  $\gamma$ -ray branching ratios.

In addition to  $(p, p)$  and  $(p, \gamma)$  data taken at the resonance energies for the determination of the yield curves, elastic scattering data were also taken at energies far from the resonances. At the low-bombarding energies the backscattered protons follow the Rutherford cross section, given as [Chu78]

$$\left(\frac{d\sigma}{d\Omega}\right)_R = \left(\frac{Z_1 Z_2 e^2}{4E}\right)^2 \frac{1}{\sin^4(\theta/2)} \quad (4.10)$$

where  $e^2 = 1.44$  MeV fm,  $E$  is the energy of the incident particle and  $\theta$  is the c.m. angle of the detector relative to the incident beam direction. The results for the intensities of the backscattered protons at different off-resonance energies and different angles are shown in figure 4.8. The solid curves reflect the energy and angular dependence given in equation 4.10. The strongest reaction which competes with Rutherford scattering is nuclear scattering at the resonance energies. The nuclear scattering yield is proportional to the strength of the resonance of interest, or  $\omega\gamma = \omega\Gamma_p^2/\Gamma$ . Assuming the two processes interfere constructively and  $\Gamma \approx \Gamma_p$ , the yield ratio of Rutherford scattering to nuclear scattering can be calculated for each of the resonances of interest. For example, the  $^{27}\text{Al} + p$  Rutherford scattering relative to resonance scattering has a yield ratio of  $\approx 300$  (or  $< 1\%$  effect on the yield resulting from Rutherford scattering). This value was determined with an upper limit for  $\Gamma$  [End90]. The results for all of the resonances of interest are listed in table 4.4. Examples of the yield of elastically scattered protons are shown in figure 4.9 for the  $E_R = 454$ -keV resonance in the  $^{26}\text{Mg}(p, \gamma)^{27}\text{Al}$  reaction and for the  $E_R = 406$ -keV resonance in the  $^{27}\text{Al}(p, \gamma)^{28}\text{Si}$  reaction. The solid line shows the Rutherford energy dependence normalized to the data, confirming that the elastic scattering is properly described by Ruther-



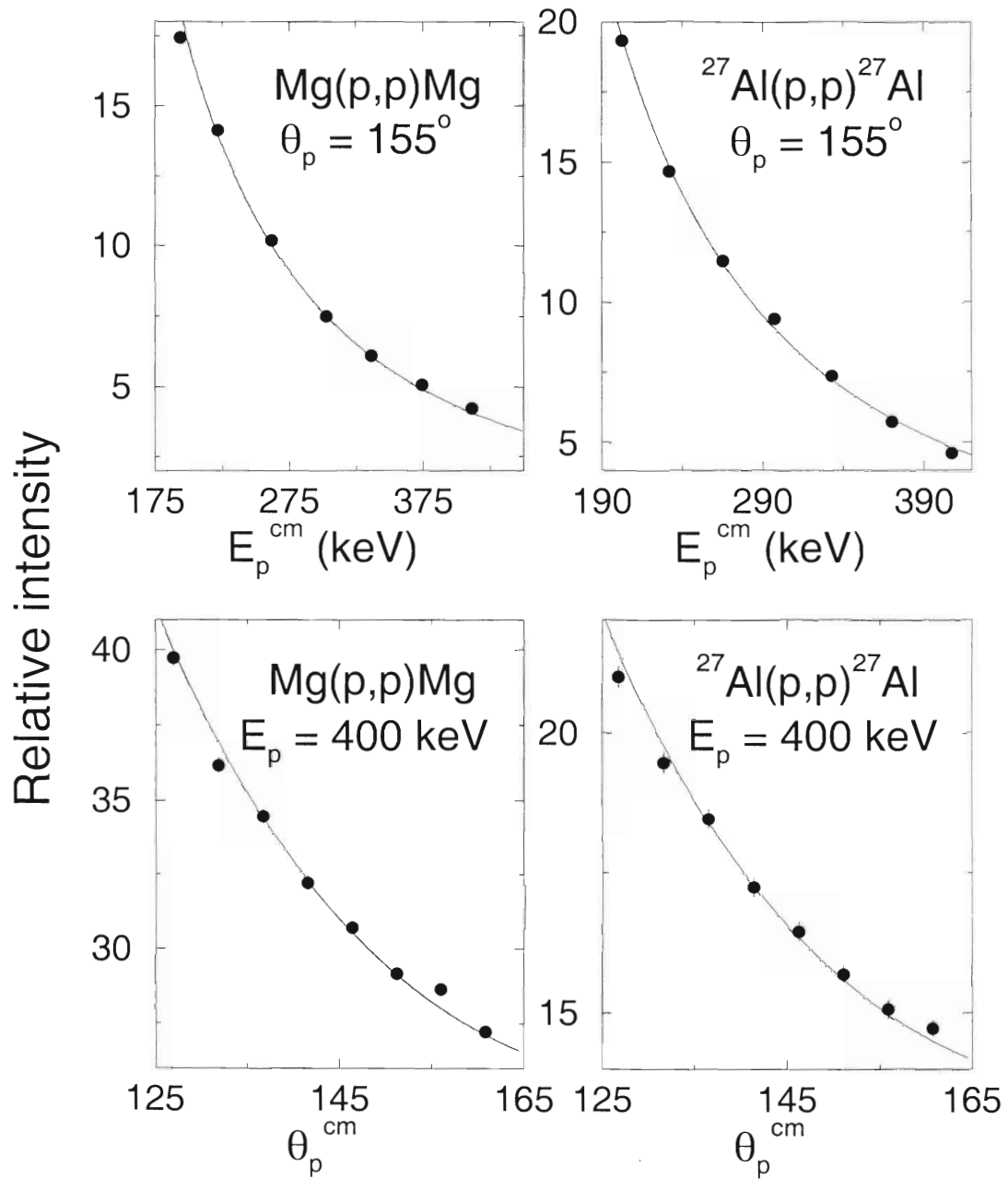


Figure 4.8: Elastic scattering of protons from Mg and Al. The intensity in the c.m. frame as a function of incident proton energy is shown on the left. On the right is the intensity of scattered protons as a function of the detector angle. The solid line shows the energy and angular dependence of the Rutherford cross section normalized to the data.

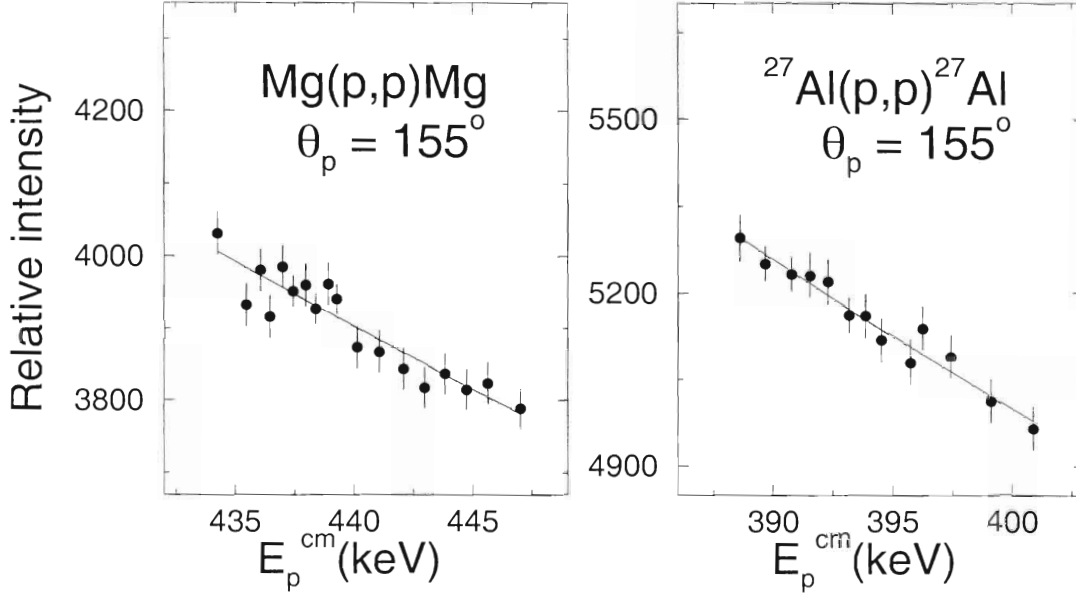


Figure 4.9: Elastic scattering of protons from Mg and Al at the energies of the  $E_R = 454$ -keV resonance in  $^{26}\text{Mg}(p, \gamma)^{27}\text{Al}$  and the  $E_R = 406$ -keV resonance in  $^{27}\text{Al}(p, \gamma)^{28}\text{Si}$ . The intensity in the c.m. frame is plotted as a function of the incident bombarding energy.

ford scattering.

Once the quantity  $N_\gamma(E)\sigma_{Ruth}(E)/N'_p(E)$  was determined from the data as a function of energy and  $N_\gamma$  was corrected for summing effects, the data were fit in order to determine the area under the curve (i.e. the integral part of equation 4.9). A yield-curve-generating routine YCURVE was adopted from U. Giesen [Gie92]. The basic premise behind the generation of a theoretical yield curve is described below. The yield from a reaction can be written as

$$Y(E) = \int_{E-\xi}^E \frac{\sigma(E)}{\epsilon(E)} dE \quad (4.11)$$

where  $\sigma$  is the  $(p, \gamma)$  cross section and  $\epsilon$  is the stopping power of the protons in the target. One way to include the effects of the beam is to write the yield in terms of  $g(E, E')$  and  $W(E, E', E'')$  which describe the beam spread and beam straggling, respectively [Gov59]

$$Y(E) = \int_{E-\xi}^E \int_0^\infty \int_0^\infty \frac{\sigma(E)}{\epsilon(E)} g(E, E') W(E, E', E'') dE dE' dE''. \quad (4.12)$$

### Rutherford versus Resonant Scattering

Reaction	$E_R$ (keV)	$Y_{Ruth}/Y_{pp}$
$^{24}\text{Mg}(p, \gamma)^{25}\text{Al}$	223	$1 \times 10^7$ <sup>a</sup>
$^{24}\text{Mg}(p, \gamma)^{25}\text{Al}$	419	$5 \times 10^4$ <sup>a</sup>
$^{25}\text{Mg}(p, \gamma)^{26}\text{Al}$	435	$2 \times 10^2$ <sup>b</sup>
$^{26}\text{Mg}(p, \gamma)^{27}\text{Al}$	338	$4 \times 10^4$ <sup>b</sup>
$^{26}\text{Mg}(p, \gamma)^{27}\text{Al}$	454	$2 \times 10^3$ <sup>b</sup>
$^{27}\text{Al}(p, \gamma)^{28}\text{Si}$	406	$3 \times 10^2$ <sup>b</sup>

Table 4.4: The ratio of the Rutherford backscattering yield  $Y_{Ruth}$  to the yield from resonance scattering  $Y_{pp}$ . <sup>a</sup>The  $Y_{pp}$  values were determined with the  $\Gamma_p$  and  $\Gamma$  values determined in this work. <sup>b</sup>The  $Y_{pp}$  values were determined assuming  $\Gamma \sim \Gamma_p$  where  $\Gamma$  was taken from [End90]. The  $E_R = 435$  keV resonance in  $^{25}\text{Mg}(p, \gamma)^{26}\text{Al}$  and the  $E_R = 406$ -keV resonance in  $^{27}\text{Al}(p, \gamma)^{28}\text{Si}$  were determined with upper limits.

The beam spread can be well described by a Gaussian distribution. The beam straggling has been described by the Bethe-Bloch theory [Mar69] as a Gaussian of width  $s$ , where  $s$  increases with the depth of penetration of the incident particles into the target. The program uses the approximation  $s = \sqrt{\text{const} \Delta E}$  where  $\Delta E$  is the energy loss of the incident particle at a given depth in the target.

The generation of the yield curve proceeds in three steps. The first step is to generate a rectangular yield curve which includes the width of the state, the height of the yield curve and the thickness of the target. The second step smears the rectangular yield curve using a Gaussian distribution to describe the beam spread. The third step is to further smear out the yield curve by increasing the width of the beam straggling as the projectile travels further into the target.

The quantity  $N_\gamma(E)/N_p'(E)$  was extracted from the spectra for each run at the different energies across the yield curve. The Rutherford cross section was calculated for the incident proton energy and the quantity  $N_\gamma(E) \sigma_R(E)/N_p'(E)$  was plotted as a function of proton energy as shown in figure 4.10. The values for the resonance energy, beam straggling, beam spread, height of the yield curve

and target thickness were determined via a  $\chi^2$  minimization of the yield curve to the data. The results of the yield curve fitting routine are shown in figure 4.10 as solid curves.

The output includes values for the height and area of the yield curve and the target thickness, as well as the uncertainties and correlations between the yield curve height and target thickness. The uncertainty in the area was determined as follows:

$$\sigma_A^2 = \xi^2 \sigma_{H_\gamma}^2 + H_\gamma^2 \sigma_\xi^2 + 2\xi H_\gamma \sigma_\xi \sigma_{H_\gamma} C \quad (4.13)$$

where  $\xi$  ( $\sigma_\xi$ ) is the target thickness (and its uncertainty),  $H_\gamma$  ( $\sigma_{H_\gamma}$ ) is the height of the yield curve (and its uncertainty), and  $C$  is the correlation between the height and target thickness.

A determination of the  $\gamma$ -ray branching ratios for the  $E_R = 223$ - and  $419$ -keV resonances in  $^{24}\text{Mg}(p, \gamma)^{25}\text{Al}$  and the  $E_R = 406$ -keV resonance in  $^{27}\text{Al}(p, \gamma)^{28}\text{Si}$  was necessary for the determination of resonance strengths. The procedure for determining branching ratios was outlined in section 4.1 and the results are shown in table 4.5. For the  $E_R = 435$ -keV resonance in  $^{25}\text{Mg}(p, \gamma)^{26}\text{Al}$  the values were taken from Endt *et al.* [End88]. For the  $E_R = 338$ -keV resonance in  $^{26}\text{Mg}(p, \gamma)^{26}\text{Al}$  the branching ratios were taken from Iliadis *et al.* [Ili90] and the  $E_R = 454$ -keV resonance branching ratios were taken from Maas *et al.* [Maa78].

The determination of the ratio  $\Omega_{cm}/\varepsilon_\gamma$  of the charged-particle efficiency to the HPGe detector efficiency via the  $^{19}\text{F}(p, \alpha_2\gamma)^{16}\text{O}$  reaction was described in section 3.2.1. For the determination of the yield curves the  $\gamma$ -rays listed in table 4.6 were used. If more than one  $\gamma$ -ray is listed, better statistics were found if the efficiency-corrected sum of the of the listed transitions were used. The final values for the resonance strengths are given in table 4.7 and are compared to the other literature values.

The dominant sources of error in the final resonance strength values were the following: area of yield curve  $\leq 3\%$ , branching ratios  $\leq 4\%$ , detector efficiency  $\leq 5\%$ , and summing corrections  $< 1\%$ . The measurement of the resonance

Branching Ratios (in %)				
Reaction	Transition	Present	Previous <sup>a</sup>	
<sup>24</sup> Mg( <i>p</i> , $\gamma$ ) <sup>25</sup> Al	R $\rightarrow$ 945	15.6 $\pm$ 1.0	19 $\pm$ 3	
	E <sub>R</sub> = 223 keV	R $\rightarrow$ 451	81.7 $\pm$ 2.7	
	E <sub>x</sub> = 2485 keV	R $\rightarrow$ 0	2.7 $\pm$ 0.3	
<sup>24</sup> Mg( <i>p</i> , $\gamma$ ) <sup>25</sup> Al	R $\rightarrow$ 1790	42.6 $\pm$ 0.8	30 $\pm$ 15	
	E <sub>R</sub> = 419 keV	R $\rightarrow$ 945	< 1	
	E <sub>x</sub> = 2674 keV	R $\rightarrow$ 451	31.2 $\pm$ 0.7	43 $\pm$ 15
		R $\rightarrow$ 0	25.2 $\pm$ 0.6	26 $\pm$ 3
<sup>27</sup> Al( <i>p</i> , $\gamma$ ) <sup>28</sup> Si	R $\rightarrow$ 10311	1.9 $\pm$ 1.2	1.2	
	E <sub>R</sub> = 406 keV	R $\rightarrow$ 9417	2.8 $\pm$ 0.3	
	E <sub>x</sub> = 1197 keV	R $\rightarrow$ 8589	5.7 $\pm$ 0.3	5.8
		R $\rightarrow$ 6888	12.2 $\pm$ 0.6	13
	R $\rightarrow$ 6879	2.3 $\pm$ 0.4	1.1	
	R $\rightarrow$ 6276	1.6 $\pm$ 0.3	1.0	
	R $\rightarrow$ 4618	71.2 $\pm$ 2.5	73	
	R $\rightarrow$ 1779	2.3 $\pm$ 0.2	2.6	

Table 4.5: Branching ratios for the E<sub>R</sub> = 223- and 419-keV resonances in <sup>24</sup>Mg(*p*,  $\gamma$ )<sup>25</sup>Al and the E<sub>R</sub> = 406-keV resonance in <sup>27</sup>Al(*p*,  $\gamma$ )<sup>28</sup>Si. <sup>a</sup>Previous branching ratios for the <sup>24</sup>Mg(*p*,  $\gamma$ )<sup>25</sup>Al reaction are taken from [End78] and for the <sup>27</sup>Al(*p*,  $\gamma$ )<sup>28</sup>Si reaction from [Mey75] where no errors were quoted.

strength relative to Rutherford scattering eliminated the need to know the total charge accumulated on target and the target stoichiometry and stopping powers. The use of the <sup>19</sup>F(*p*,  $\alpha_2\gamma$ )<sup>16</sup>O reaction eliminated the need to know the absolute efficiency of the charged-particle and the HPGe detectors. Therefore the present results listed in table 4.7 are more reliable than previous results.

There is excellent agreement between the present results and the resonance strengths values quoted in [Ili90, Buc80] for the E<sub>R</sub> = 338-keV resonance in <sup>26</sup>Mg(*p*,  $\gamma$ )<sup>27</sup>Al, [And80] for the E<sub>R</sub> = 435-keV resonance in the <sup>25</sup>Mg(*p*,  $\gamma$ )<sup>26</sup>Al

$E_R$ (keV)	Transition(s) (keV)
223	2485 $\rightarrow$ 451
419	2674 $\rightarrow$ 1790
	2674 $\rightarrow$ 452
	2674 $\rightarrow$ 0
435	6724 $\rightarrow$ 228
	6724 $\rightarrow$ 0
338	8598 $\rightarrow$ 6814
	8598 $\rightarrow$ 4055
	8598 $\rightarrow$ 3680
454	8709 $\rightarrow$ 844
406	11976 $\rightarrow$ 4618

Table 4.6: A list of the  $\gamma$ -ray transitions used to generate the yield curves for the determination of resonance strengths.

reaction, and [Seu88, Mey75, Lyo69] for the  $E_R = 406$ -keV resonance in the  $^{27}\text{Al}(p, \gamma)^{28}\text{Si}$  reaction. Note that the results of [Kei80] overpredict the resonance strength of the  $E_R = 435$ -keV resonance in  $^{25}\text{Mg}(p, \gamma)^{26}\text{Al}$  by a factor of two. The  $E_R = 454$ -keV resonance in  $^{26}\text{Mg}(p, \gamma)^{27}\text{Al}$  is also overpredicted by [Kei80]. The  $E_R = 223$ - and 419-keV resonances in  $^{24}\text{Mg}(p, \gamma)^{25}\text{Al}$  are approximately 30% greater than the values quoted for [Tra75b].

The standard  $(p, \gamma)$  resonance strengths ( $E_R \geq 0.5$  MeV) for reactions involving Mg and Al isotopes compiled by Sargood [Sar82] are mainly based on the measurements of the Melbourne/Caltech group [Pai79, And80, Lyo69]. Consequently, the excellent agreement of the present absolute strengths for the  $E_R = 435$ -keV resonance in  $^{25}\text{Mg}(p, \gamma)^{26}\text{Al}$  and the  $E_R = 406$ -keV resonance in  $^{27}\text{Al}(p, \gamma)^{28}\text{Si}$  with the relative values of [And80, Lyo69] suggest that our results can be used in order to extend the set of standard  $(p, \gamma)$  resonance strengths in

Reaction	$E_R$ (keV)	$J^\pi$	$\omega\gamma$ (meV)	
			Literature	Present
$^{24}\text{Mg}(p, \gamma)^{25}\text{Al}$	223	$1/2^+$	$9.5 \pm 2.0$ [Tra75b]	$12.7 \pm 0.9$
			$5.1 \pm 1.1$ [Dwo70]	
			$13.7 \pm 6.9$ [End67]	
$^{24}\text{Mg}(p, \gamma)^{25}\text{Al}$	419	$3/2^+$	$33 \pm 5$ [Tra75b]	$41.6 \pm 2.6$
			$15.8 \pm 3.2$ [Dwo70]	
$^{25}\text{Mg}(p, \gamma)^{26}\text{Al}$	435	$4^-$	$131 \pm 16$ [End67]	$94.2 \pm 6.5$
			$98 \pm 8$ [And80]	
			$192 \pm 17$ [Kei80]	
$^{26}\text{Mg}(p, \gamma)^{27}\text{Al}$	338	$3/2^-$	$250 \pm 30$ [Ili90]	$273 \pm 16$
			$700 \pm 15$ [Smi82]	
			$250 \pm 110$ [Buc80]	
$^{26}\text{Mg}(p, \gamma)^{27}\text{Al}$	454	$1/2^+$	$1100 \pm 100$ [Kei80]	$715 \pm 41$
			$460 \pm 70$ [End67]	
$^{27}\text{Al}(p, \gamma)^{28}\text{Si}$	406	$(3^-, 4^+)$	$7 \pm 2$ [Seu88]	$8.63 \pm 0.52$
			$8.3$ [Mey75]	
			$10 \pm 2$ [Lyo69]	

Table 4.7: The resonance strengths presented in the literature compared to the present results.

the sd-shell [Sar82] to energies below  $E_R = 0.5$  MeV.

### 4.3 Mean Lifetimes

A previous measurement of the mean lifetime of the  $E_x = 2485$ -keV state was made by Dworkin *et al.* [Dwo74]. The work was never published and contains potential sources of systematic uncertainties (described below) that motivated us to remeasure it. The Dworkin *et al.* measurement was performed with an

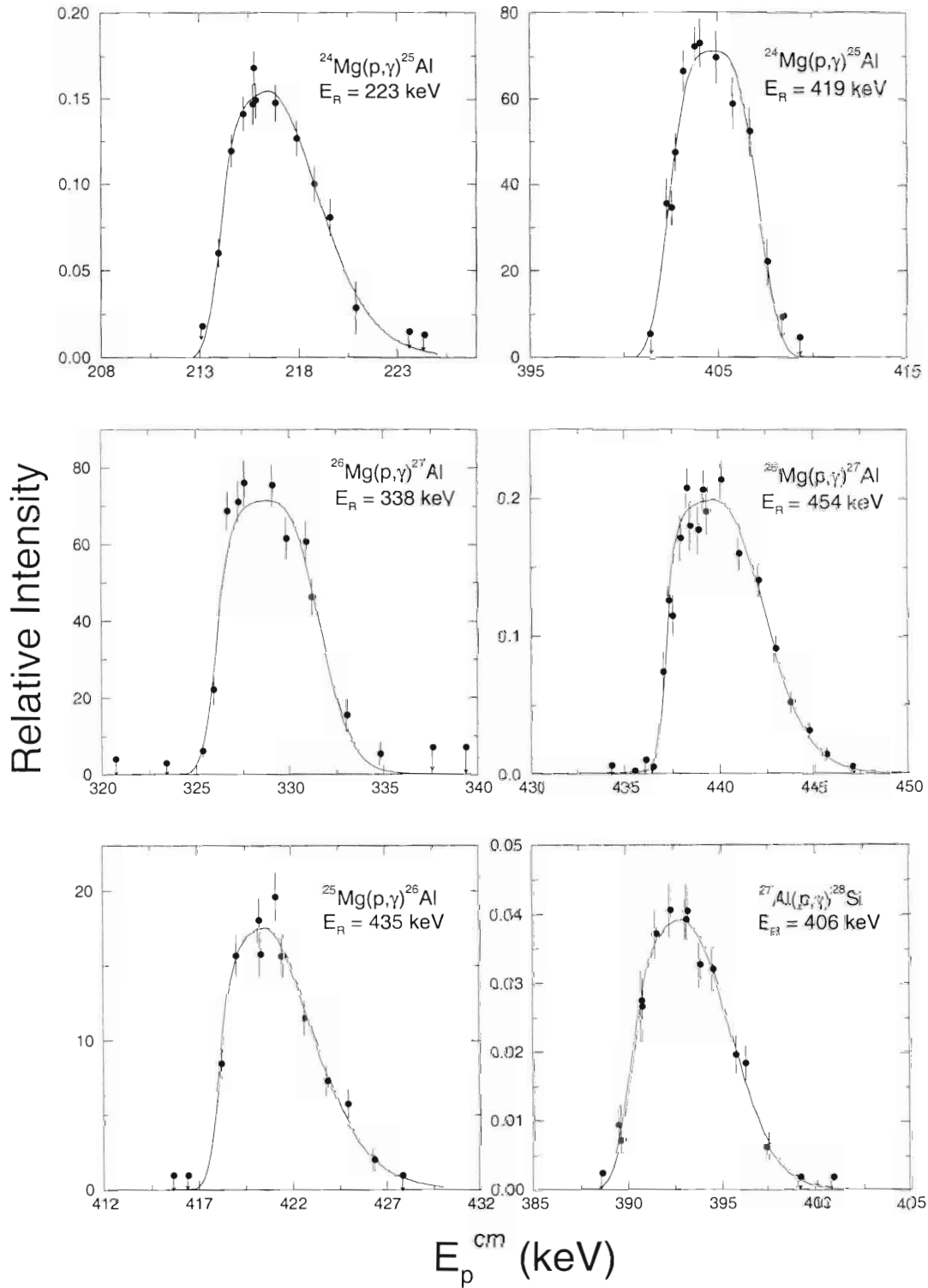


Figure 4.10: Yield curves obtained by normalization of the number of  $\gamma$ -rays to the number of backscattered protons multiplied by the Rutherford cross section. When more than one transition is used, relative efficiencies were also included in the yield curves. The solid line represents a least-squares fit to data from the yield curve fitting program.



evaporated Mg target, which also contained oxygen, which was not considered in their analysis. In addition, the determination of mean lifetimes of nuclei recoiling in a low- $Z$  material is less sensitive than for a high- $Z$  material for  $\tau \leq 10$  fs. Their measurement was performed at a bombarding energy of  $E_p = 223$  keV (much lower than the present  $E_p = 1620$  keV), yielding a slower recoil velocity, and therefore a smaller observed Doppler shift. Finally, the stopping powers calculated by Dworkin *et al.* have since been experimentally determined. All of these concerns are addressed in the present measurement.

The mean lifetime of a state is the average length of time the state exists before it decays. The mean lifetime is given as [Kra88]

$$\tau = \frac{\int_0^\infty t |dN/dt| dt}{\int_0^\infty |dN/dt| dt} \quad (4.14)$$

where  $t$  is time and  $N$  is the number of radioactive nuclei at time  $t$ . The number of radioactive nuclei at a time  $t$  is given by

$$N(t) = N_o e^{-\lambda t} \quad (4.15)$$

where  $N_o$  is the original number of nuclei prior to any decays and  $\lambda$  is the decay constant. Solving for  $\tau$  from equation 4.14 and 4.15 yields  $\tau = 1/\lambda$ . The time dependent wave function for a state that decays with a mean lifetime  $\tau$  is given by [Kra88]

$$\Psi(\vec{r}, t) = \Psi(\vec{r}) e^{-iE_R t/\hbar} e^{-t/2\tau}. \quad (4.16)$$

The probability of observing the state in an energy interval between  $E$  and  $E + dE$  is determined by squaring the amplitude of the Fourier transform of the time dependent part of equation 4.16 which yields

$$P(E)dE = \frac{dE}{(E - E_R)^2 + \hbar^2/4\tau^2}. \quad (4.17)$$

The probability distribution is Lorentzian with a maximum at  $E_R$  (the resonance energy) and with a full-width-half-maximum  $\Gamma$  where

$$\Gamma \equiv \hbar/\tau. \quad (4.18)$$

From this relation, the total width of the state is determined from the mean lifetime.

For an object moving with velocity  $v$  relative to an observer, from which a  $\gamma$ -ray is emitted with an energy  $E_o$ , the energy of the  $\gamma$ -ray (as seen by the observer) is given to first order in  $\beta$  as

$$E = E_o(1 + \beta \cos \theta) \quad (4.19)$$

where  $\beta = v/c$  and  $\theta$  is the angle between initial recoil direction and the observer.

The observed  $\gamma$ -ray energy is strongly correlated with the velocity of the recoiling nucleus. In our experiments, the nuclei recoil in the target and are slowed via interactions with the target and backing atoms. The slowing process of nuclei interacting with other particles is described by two processes, electronic and nuclear interactions [Zie80]. The electronic stopping power corresponds to the energy transferred by the recoiling ion to the electrons in the slowing medium, producing a gradual slowing of the recoil nuclei. The nuclear stopping power describes the energy lost by the recoiling nuclei as a result of Coulomb scattering with the target nuclei. In addition to a gradual slowing of the recoiling nuclei, the nuclear component can also change its direction of motion. The total stopping power is the sum of the electronic and nuclear stopping powers.

The quantity  $F(\tau)$  is defined as the average Doppler shift relative to the full Doppler shift. A full Doppler shift occurs when the moving object decays with its initial recoil velocity and no Doppler shift occurs when the object is at rest, corresponding to values of  $F(\tau) = 1$  and  $0$ , respectively. The equation for  $F(\tau)$  is given by

$$F(\tau) = \frac{\int_{\phi}^{\phi_{\text{cos}}} e^{-t/\tau} v \cos \phi dt}{v_o \tau} \quad (4.20)$$

where  $\phi$  is the angle of divergence of the recoil nuclei from the original direction of motion. The calculation of  $F(\tau)$  for a range of lifetimes is described in detail later in this chapter.

In order to experimentally determine the value for  $F(\tau)$ , one can measure the

average  $\gamma$ -ray energy, and use

$$E = E_o[1 + \beta_o F(\tau) \cos \theta] \quad (4.21)$$

where  $\beta_o = v_o/c$ . When designing the experiment it is important to use a material that slows the recoiling nuclei on a time scale comparable to the mean lifetime of the state. This is the basic premise behind the Doppler-shift-attenuation method (DSAM) [Dev55, Dev56, Bun56]. The experimentally determined  $F(\tau)$  value can be compared to a calculated  $F(\tau)$  curve to extract the mean lifetime of the state of interest.

The mean lifetime of the  $E_x = 2485$ -keV state was determined from protons incident at the  $E_R = 1616$ -keV resonance, which subsequently decayed to the state of interest. The total width of the  $E_x = 3823$ -keV state (corresponding to the  $E_R = 1616$ -keV resonance) is 36 keV [End90] which yields a mean lifetime  $\tau \sim 10^{-5}$  fs, and therefore has a negligible influence on the determination of the mean lifetime of the  $E_x = 2485$ -keV state. The higher incident proton energy (as compared to [Dwo74]) implies a higher  $^{25}\text{Al}$  recoil velocity, leading to a larger shift between the observed  $\gamma$ -ray energies at the different detector angles. The mean lifetime of the  $E_x = 2674$ -keV state is determined from the capture of protons incident at the  $E_R = 1654$ -keV resonance, which subsequently decays to the state of interest. The total width of the  $E_x = 3859$ -keV state, corresponding to the  $E_R = 1654$ -keV resonance, is 100 eV [End90], which indicates a mean lifetime of the order  $10^{-3}$  fs, which again has a negligible impact on our extracted lifetime value.

The decision to implant Mg into Ta (see section 3.1.2) resulted from the need to determine lifetimes on the order of 10 fs. The existence of Ta in the Mg target causes the recoiling nuclei to slow on a quicker time scale relative to that for a pure Mg target, as a result of the higher  $Z$  material. A faster slowing medium provides greater sensitivity to smaller lifetime values. A balance must be reached between the number of Mg ions relative to Ta atoms so that both a reasonable

count rate and proper slowing are achieved.

Portions of the spectra for the 2°, 90° and 141° detectors used to determine the  $F(\tau)$  value of the  $E_x = 2485$ -keV state are shown in figure 4.11. The spectra include the 2034-keV  $\gamma$ -ray that results from the decay of the  $E_x = 2485$ -keV state to the first-excited state in  $^{25}\text{Al}$ . The resolution was less than 2.5 keV at  $E_\gamma = 1332$  keV for the detectors and the dispersion was  $\sim 0.5$  keV/channel in each of the spectra. In order to determine the energies of peaks in the spectra, their centroids had to be determined as accurately as possible. The shapes of the Doppler shifted  $\gamma$ -rays vary as a function of their lifetimes and the detector position, and therefore, no assumption regarding the shapes of the  $\gamma$ -rays were assumed in the determination of centroids. A program [Bru94] was used to fit a linear background through a user-defined region and from the resulting counts the centroid and corresponding error were determined. The observed  $\gamma$ -ray energy could then be determined via the energy calibration described in section 3.2.2. In addition, angular distribution effects on the observed centroid of a  $\gamma$ -ray were considered, and proved to be negligible.

The detectors are not point-like, thus corrections had to be made for the sampling of the  $\gamma$ -ray energies over a range of angles. Equation 4.21 would have the following substitution

$$\cos \theta \equiv Q \cos \theta_{\alpha=0} \quad (4.22)$$

where  $Q$  is the attenuation factor [Ros53] resulting from the solid angle of the detector and  $\theta_{\alpha=0}$  is the angle corresponding to the center of the detector. The attenuation  $Q$  was determined from a numerical integration using the formalism of Rose [Ros53]

$$Q = \frac{\int_0^{\alpha_{max}} \cos \alpha \epsilon(\alpha) \sin \alpha d\alpha}{\int_0^{\alpha_{max}} \epsilon(\alpha) \sin \alpha d\alpha} \quad (4.23)$$

where  $\alpha$  is the angle between the point source of emitted  $\gamma$ -rays incident at the center of the detector to  $\gamma$ -rays incident off center,  $\cos \alpha$  is the angular dependence of the energy of the emitted  $\gamma$ -rays (see equation 4.21) and  $\epsilon(\alpha)$  is the efficiency of the detector at the angle  $\alpha$ . The program EGS4 [Nel85] was used to determine

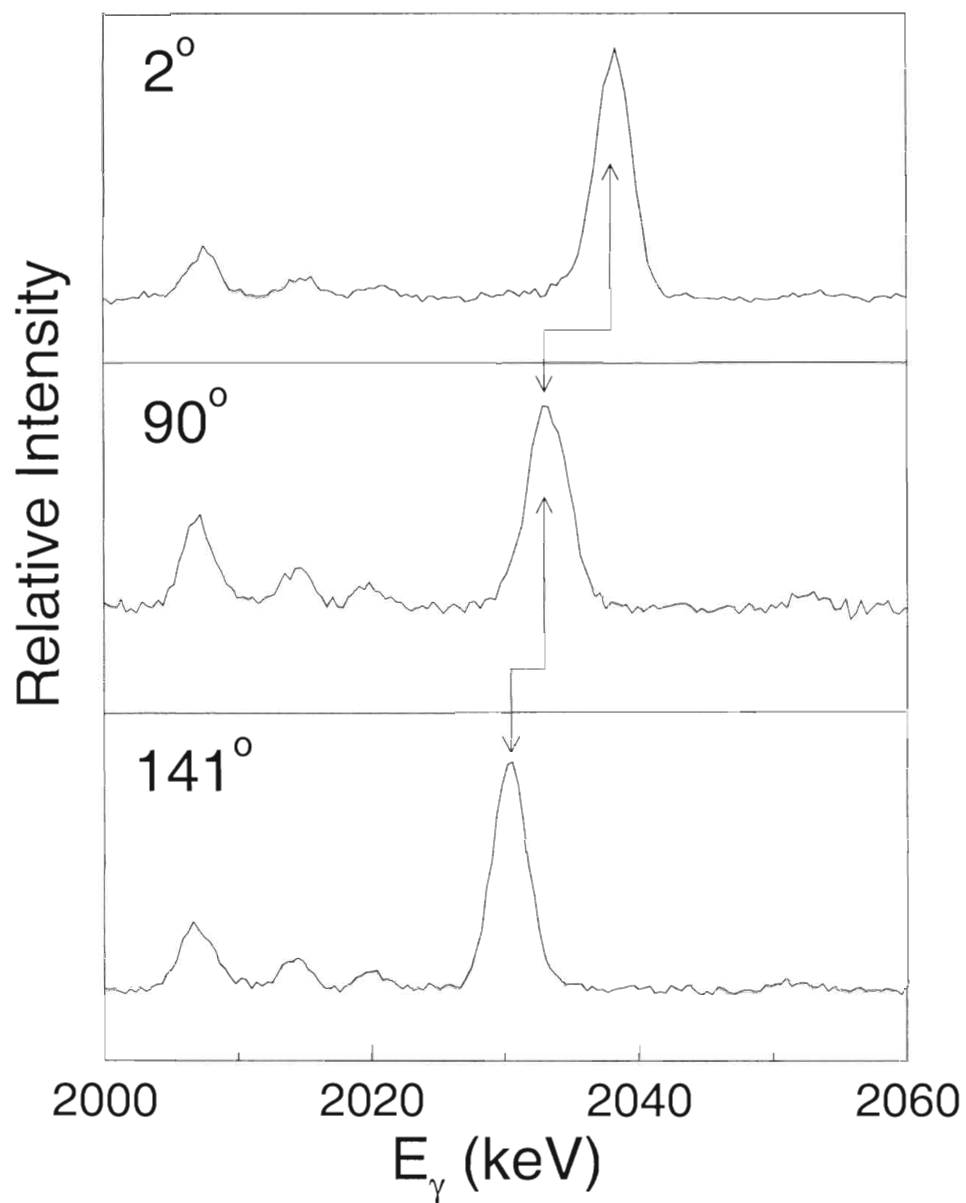


Figure 4.11: The  $\gamma$ -ray resulting from the decay of the  $E_x = 2435$ -keV state to the first excited state in  $^{25}\text{Al}$  for detectors at angles of  $2^\circ$  (*top*),  $90^\circ$  (*center*) and  $141^\circ$  (*bottom*).

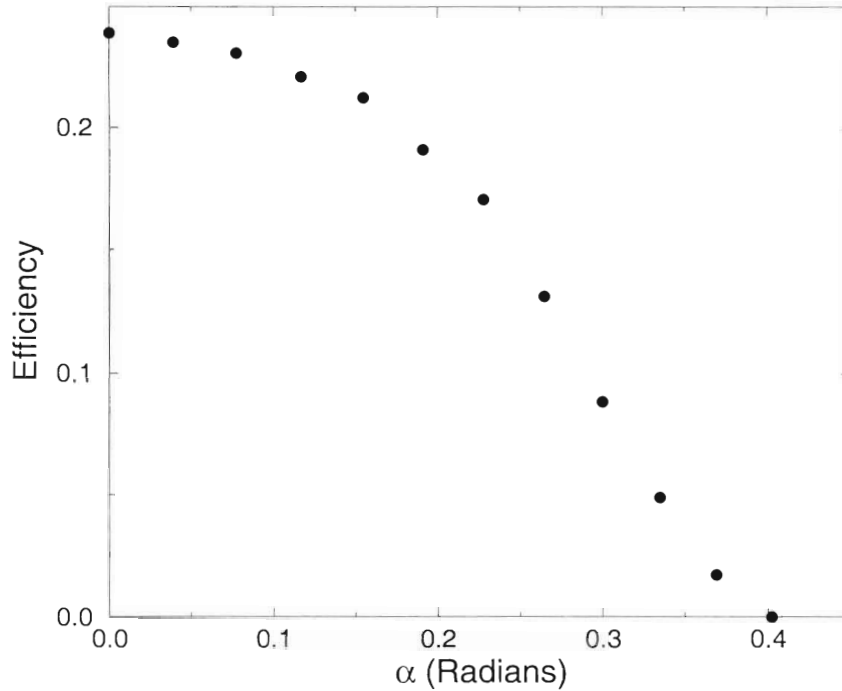


Figure 4.12: The efficiency across the front face of a 60% HPGe detector at a distance of 8.1 cm for a 2-MeV  $\gamma$ -ray.

the efficiency of the HPGe detector for  $\gamma$ -rays incident across the front face of the detector for a given geometry. A sample efficiency curve as a function of the angle  $\alpha$  across the front face of the crystal for a 2-MeV  $\gamma$ -ray with a target-to-detector distance of 8.1 cm and a crystal radius of 3.45 cm is shown in figure 4.12. Corrections for the effect of attenuation for the angular dependence of the energy of the  $\gamma$ -ray were always less than 3% ( $Q > 0.97$ ).

A program, FITFTAU, used to determine the  $F(\tau)$  value from a given mean lifetime was adopted from E. F. Moore and modified for our purposes. The determination of the velocity of the particle using the Blaugrund approximation (discussed later in this chapter) was properly incorporated into the program and the format of the output was modified to generate  $F(\tau)$  curves. An outline of the program is given in figure A.1. In general, the program numerically integrates the following

$$F(\tau) = \frac{\int_0^\infty e^{-t/\tau} \overline{v \cos \phi} dt}{v_o \tau}. \quad (4.24)$$

Knowledge of the velocity of the particle requires an accurate determination of the stopping powers for Al nuclei in the target. The program was set up to incorporate TRIM stopping powers as taken from the Ziegler formalism [Zie80]. The electronic stopping power of Al recoiling in Ta resulting from TRIM had the correct energy dependence but needed to be renormalized by a factor of  $2.12 \pm 0.10$  in order to match the experimentally determined values [Ars90]. The nuclear stopping power has also been established [Tik91, Ant82] and the TRIM nuclear stopping powers were renormalized by a factor of  $0.67 \pm 0.05$ . The electronic and nuclear stopping power normalizations for Al recoiling in Mg were taken from reference [Kei83], where the electronic stopping power was normalized by a factor of  $1.0 \pm 0.2$  and the nuclear stopping power was normalized by a factor of  $1.00 \pm 0.18$ . The resulting electronic and nuclear components of the stopping power are shown in figure 4.13.

The FITFTAU program uses what is known as the Blaugrund approximation, where  $\overline{v/c \cos \phi} \approx \overline{v/c} \overline{\cos \phi}$  [Bla66], which has already been incorporated in equation 4.24. The reliability of the Blaugrund approximation was tested by Currie via comparison with the results of a Monte Carlo calculation. The Blaugrund approximation results were in agreement to better than 10% with the Monte Carlo calculations [Cur69]. Since the average divergence of the recoiling nucleus results from the nuclear part of the stopping power, which dominates at lower velocities, the Blaugrund approximation plays more of a role for the larger lifetimes. For the states of interest ( $\tau \sim 5$  fs) the errors in the  $F(\tau)$  curve resulting from the Blaugrund approximation are less than 1%. The components necessary for the calculation of the  $F(\tau)$  curve for a mean lifetime of  $\tau = 5$  fs and  $E_p = 1620$  keV are shown in figure 4.14. The final errors in the calculated  $F(\tau)$  curves resulted from the uncertainty in the stoichiometry of the target (see section 3.1.2) and uncertainties in the normalizations used for the stopping powers.

The  $F(\tau)$  value for the  $E_x = 3823 \rightarrow 945$ -keV transition was determined from

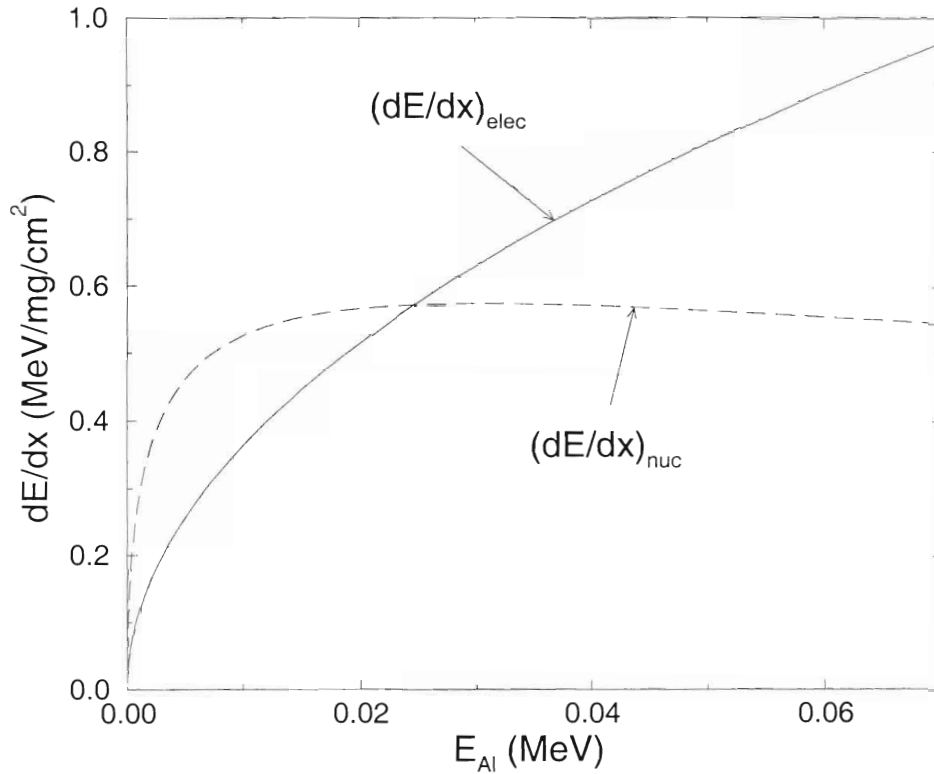


Figure 4.13: The electronic and nuclear components of the stopping power (from TRIM) after proper renormalization.

the data through the use of equation 4.21 and resulted in  $F(\tau) = 0.97 \pm 0.03$ , consistent with  $F(\tau) = 1$ , as expected based on a lifetime of  $\tau \sim 10^{-5}$  fs. The experimental value for the  $E_x = 2485 \rightarrow 945$ -keV transition is  $F(\tau) = 0.93 \pm 0.04$  and for the  $E_x = 2485 \rightarrow 451$ -keV transition  $F(\tau) = 0.91 \pm 0.03$ , resulting in a weighted average of  $F(\tau) = 0.92 \pm 0.03$ . The  $F(\tau)$  values for the  $E_x = 2485$ -keV state are shown in figure 4.15.

The  $F(\tau)$  values for the  $E_x = 3859$ - and  $2674$ -keV states were extracted from the data taken at the  $E_R = 1654$ -keV resonance. The value for the  $E_x = 3859 \rightarrow 1616$ -keV transition is  $F(\tau) = 0.95 \pm 0.03$  and the value for the  $E_x = 3859 \rightarrow 1790$ -keV transition is  $F(\tau) = 0.98 \pm 0.03$ . The mean lifetime of the  $E_x = 3859$ -keV state is on the order of  $10^{-3}$ , implying  $F(\tau) = 1$ . The value for the  $E_x = 2674$ -keV state resulting from the  $\gamma$ -ray transition to the  $E_x = 1790$ -keV state



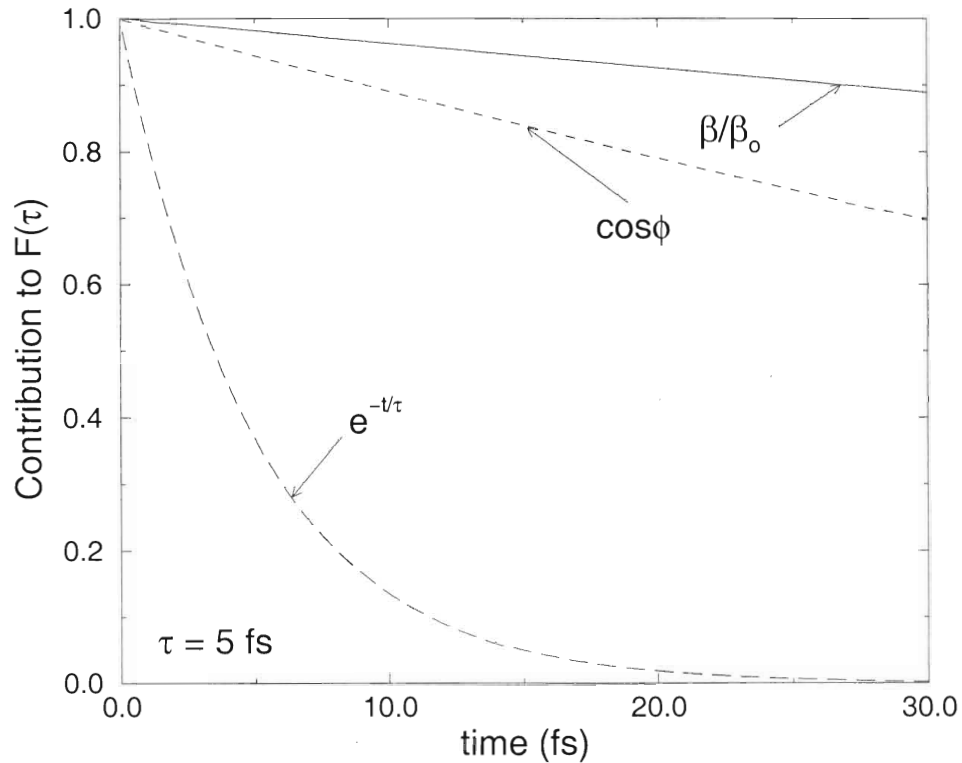


Figure 4.14: The contributions of the different components to the value of  $F(\tau)$  for a mean lifetime of 5 fs at  $E_p = 1620$  keV.

(shown in figure 4.16) is  $F(\tau) = 0.91 \pm 0.05$ . The larger error is the result of poorer statistics in the  $\gamma$ -ray spectra.

The smooth curve in figure 4.17 represents the calculated  $F(\tau)$  curve (and the corresponding errors) from the FITFTAU program for protons incident on the implanted Mg target with an energy of 1620 keV. The mean lifetime was extracted from the curve and the experimental  $F(\tau)$  value of the  $E_x = 2485$ -keV state, and resulted in  $\tau = 5.3 \pm \frac{2.9}{2.4}$  fs. The  $F(\tau)$  curve for a proton energy of  $E_p = 1654$  keV is shown in figure 4.18. The  $F(\tau)$  value of the  $E_x = 2674$ -keV state is shown and is consistent with a mean lifetime of  $\tau = 6.1 \pm \frac{4.8}{3.7}$  fs. The results are summarized in table 4.8. The  $90^\circ$  data contained a systematic offset, the source of which was never identified. One possible source for the offset was the absorption of  $\gamma$ -rays in the target holder and backing. The  $90^\circ$  detector does

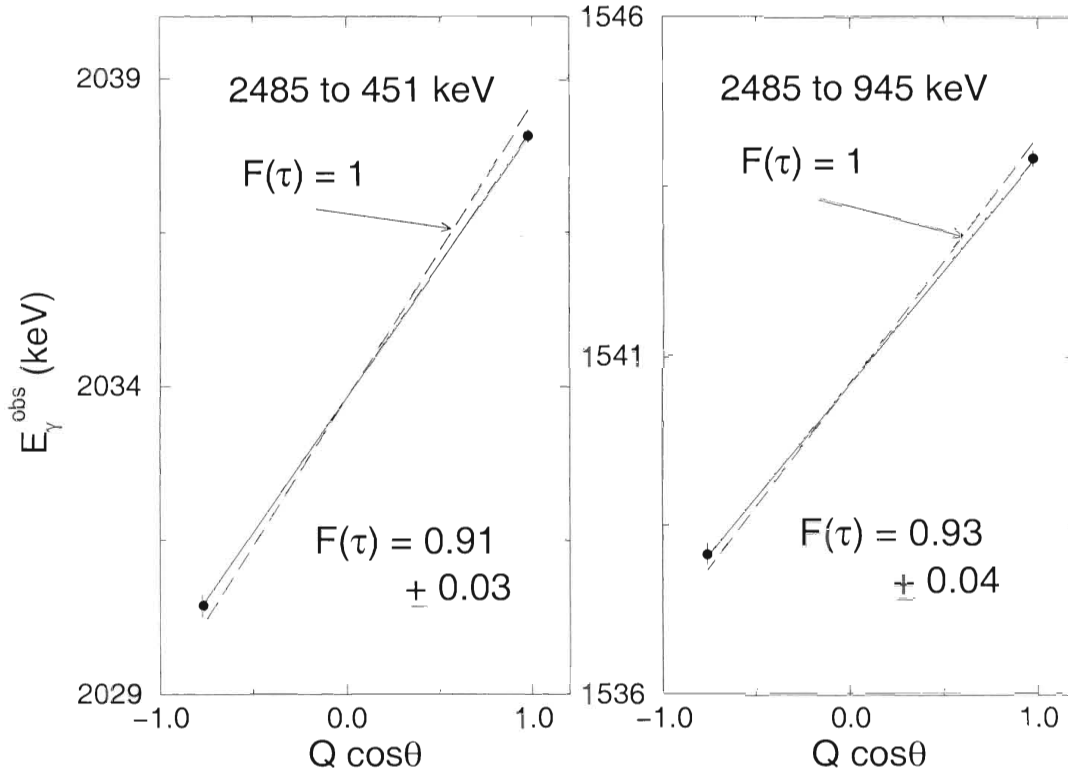


Figure 4.15: The observed  $\gamma$ -ray energy (incorporating the uncertainty in the position of the detector) as a function of  $Q \cos \theta$ , where  $Q$  is the correction for the solid angle of the detector and  $\theta$  is the angle between the detector and the incident proton beam. The solid line represents the  $F(\tau)$  value resulting from the data and the dashed line corresponds to an  $F(\tau) = 1$ .

not play a significant role in the determination of the slopes of the lines in the  $Q \cos \theta$  versus  $E_{\gamma}^{obs}$  plots, or the  $F(\tau)$  values, and was therefore not used in the determination of  $F(\tau)$ .

The previous results found in the literature for the total width of the  $E_x = 2485$ - and  $2674$ -keV states in  $^{25}\text{Al}$  are  $<32$  eV and  $<44$  eV [Uhr85], respectively. These results were obtained from the slope of the front edge of a yield curve. The lifetime values quoted in table 4.8 for the  $E_x = 3823$ - and  $3859$ -keV states result from the total widths given in [End90]. The present results are shown in table 4.8 and are in agreement with the previous results. In addition, the value of  $\tau = 8.4 \pm 3.0$  fs obtained in the unpublished lifetime measurement of [Dwo74]

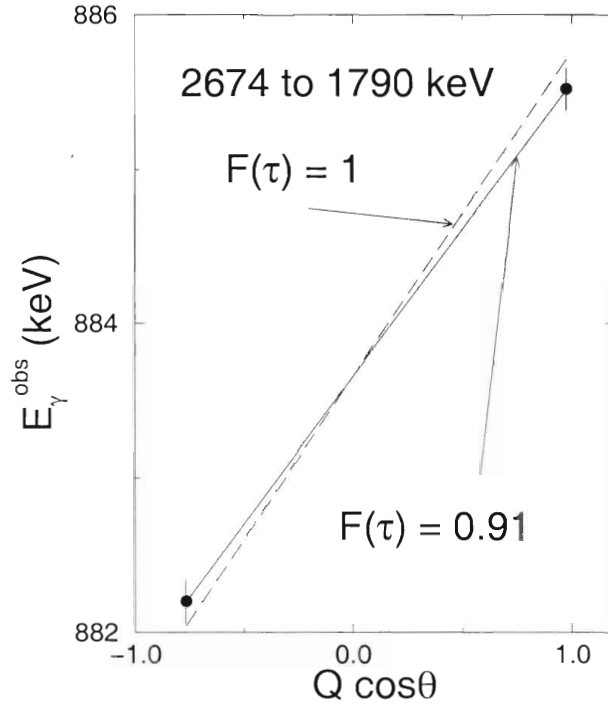


Figure 4.16: The observed  $\gamma$ -ray energy (incorporating the uncertainty in the position of the detector) as a function of  $Q \cos \theta$ , where  $Q$  is the correction for the solid angle of the detector and  $\theta$  is the angle between the detector and the incident proton beam.

Lifetime values			
$E_x$ (keV)	$F(\tau)$	$\tau$ (fs) present	$\tau$ (fs) previous
2485	$0.92 \pm 0.03$	$5.3 \pm \begin{smallmatrix} 2.9 \\ 2.4 \end{smallmatrix}$	$> 0.02$ [Uhr85]
2674	$0.91 \pm 0.05$	$6.1 \pm \begin{smallmatrix} 4.8 \\ 3.7 \end{smallmatrix}$	$> 0.01$ [Uhr85]
3823	$0.97 \pm 0.03$	$< 4$	$(1.8 \pm 0.3) \times 10^{-5}$ [End90]
3859	$0.97 \pm 0.03$	$< 5$	$6.6 \times 10^{-3}$ [End90]

Table 4.8: The lifetime values of the present work and previous values.

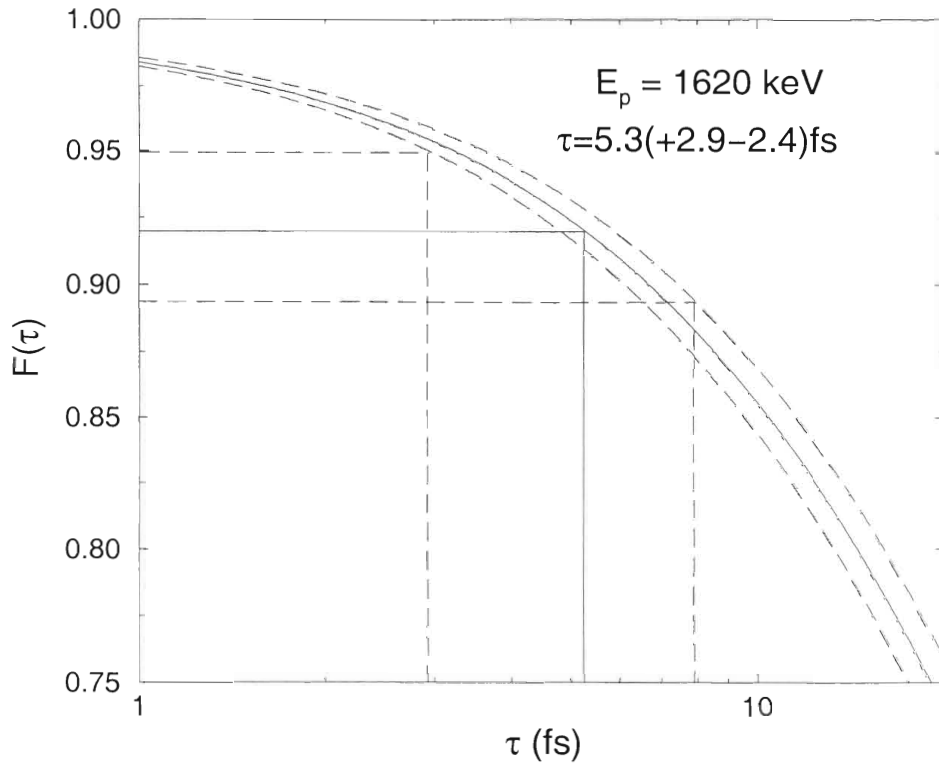


Figure 4.17: The  $F(\tau)$  curve obtained from the FITFTAU program for  $E_p = 1620 \text{ keV}$  on the  $^{24}\text{Mg}$  implanted into Ta target. The  $F(\tau)$  value for the  $E_x = 2485\text{-keV}$  state is shown and the mean lifetime  $\tau$  is interpolated from the curve.

is consistent with the present results, despite the potentially large systematic errors.

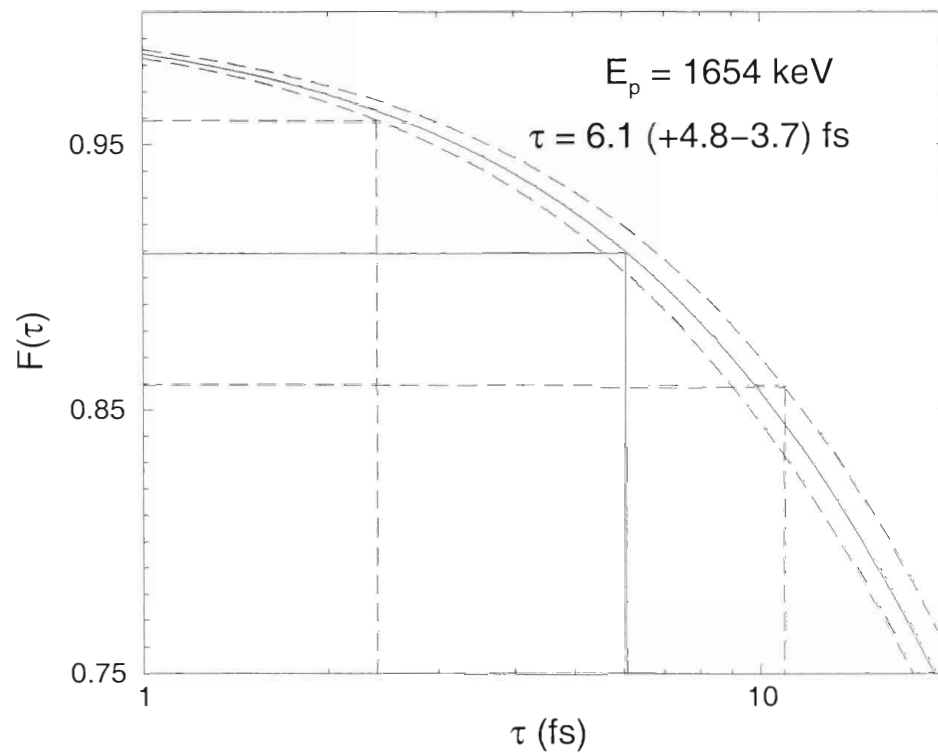


Figure 4.18: The  $F(\tau)$  curve obtained from the FITFTAU program for  $E_p = 1654 \text{ keV}$  on the  $^{24}\text{Mg}$  implanted into Ta target. The  $F(\tau)$  value for the  $E_x = 2674\text{-keV}$  state is shown and the mean lifetime  $\tau$  is interpolated from the curve.



## Chapter 5

# Nuclear and Astrophysical Implications

The experimentally determined values for the resonance strengths,  $\gamma$ -ray branching ratios and the lifetime measurement are summarized in table 5.1. The total width for the  $E_x = 2485$ -keV state resulting from the resonance strength and branching ratio measurements is  $\Gamma = 155 \pm 48$  meV. The lifetime measurement results in a total width  $\Gamma = 125 \pm_{44}^{103}$  meV. The asymmetric errors resulting from the lifetime measurement were symmetrized via the following [Aud97]

$$(X) \pm_b^a \rightarrow \left( X + \frac{a-b}{2} \right) \pm \left( \frac{a+b}{2} \right) \quad (5.1)$$

resulting in a total width  $\Gamma = 154 \pm 74$  meV. The error weighted average of the two determinations is  $\Gamma = 155 \pm 40$  meV.

The total width for the  $E_x = 2674$ -keV state resulting from the resonance strength and branching ratio measurements is  $\Gamma = 190 \pm 15$  meV. The lifetime measurement yields a total width  $\Gamma = 108 \pm_{48}^{166}$  meV and, after symmetrizing,  $\Gamma = 166 \pm 107$  meV. The error-weighted average of the two determinations is  $\Gamma = 190 \pm 15$  meV.

The focus of this chapter is the determination of proton partial widths,  $\gamma$ -ray partial widths, and total widths for the  $E_R = 223$ - and 419-keV resonances in  $^{24}\text{Mg}(p, \gamma)^{25}\text{Al}$  resulting from the experimentally determined values. In addition,

$E_R$ (keV)	Parameter	Value	$\Gamma$ (meV)
223	$\Gamma_\gamma/\Gamma$	$0.91 \pm 0.03$	$155 \pm 48$
	$\omega_\gamma$	$12.7 \pm 0.9$ meV	
	$\tau$	$5.3 \pm_{2.4}^{2.9}$ fs	
419	$\Gamma_\gamma/\Gamma$	$0.125 \pm 0.008$	$190 \pm 15$
	$\omega_\gamma$	$41.6 \pm 2.6$ meV	
	$\tau$	$6.1 \pm_{3.7}^{4.8}$ fs	

Table 5.1: Summary of experimental results and individual  $\Gamma$  values.

$E_R$	$\Gamma_p$ (meV)	$\Gamma_\gamma$ (meV)	$\Gamma$ (meV)
223	$14 \pm 1$	$141 \pm 47$	$155 \pm 40$
419	$166 \pm 15$	$24 \pm 2$	$190 \pm 15$

Table 5.2: The proton,  $\gamma$ -ray and total widths that result from the present measurements.

proton spectroscopic factors were determined for the  $E_x = 2485$ - and  $2674$ -keV states and compared to previous values. Implications for direct capture models are also discussed. The rate for  $^{24}\text{Mg}(p, \gamma)^{25}\text{Al}$  resulting from the present work is presented for temperatures of  $T_9 = 0.02 - 2$  and a comparison is made of the present reaction rate to the previously determined rate compiled by Caughlan and Fowler [Cau88]. In addition, the implications for the production of Al and destruction of  $^{24}\text{Mg}$  in M13 red giant branch stars are addressed.

## 5.1 Nuclear Structure

The resonance strength and branching ratio measurements allow for the determination of partial widths and proton spectroscopic factors. The proton and  $\gamma$ -ray partial widths can be calculated directly from the resonance strength and  $\gamma$ -ray branching ratio values. The  $E_x = 2485$ -keV state has a proton partial width  $\Gamma_p = 14 \pm 1$  meV and a  $\gamma$ -ray partial width  $\Gamma_\gamma = 141 \pm 47$  meV. The  $E_x$



= 2674-keV state has a proton partial width  $\Gamma_p = 166 \pm 15$  meV and a  $\gamma$ -ray partial width  $\Gamma_\gamma = 24 \pm 2$  meV. The  $E_x = 2674$ -keV partial widths have been determined previously [Dwo72] via a  $\Gamma_\gamma/\Gamma$  and  $\omega\gamma$  measurement and resulted in  $\Gamma_p = 74 \pm 18$  meV and  $\Gamma_\gamma = 8.8 \pm 2.5$  meV. The discrepancy results from the disagreement between the resonance strengths as seen in table 4.7. The present partial and total widths are shown in table 5.2.

The proton spectroscopic factor  $S$  is calculated from the proton partial width via the following equation [Ili97]

$$\Gamma_p = 2 \frac{\hbar^2}{\mu a^2} P_l C^2 S \theta_{sp}^2 \quad (5.2)$$

where  $C$  is the isospin Clebsch-Gordon coefficient ( $C^2 = 1$ ) and the other quantities in equation 5.2 were defined in chapter 2. The spectroscopic factor is a measure of how much the states in  $^{25}\text{Al}$  resembles a  $^{24}\text{Mg}$  core plus a proton.

The resulting spectroscopic factors for the  $E_x = 2485$ - and  $2674$ -keV states are listed in table 5.3 in addition to the spectroscopic factors for the bound states in  $^{25}\text{Al}$ . There is excellent agreement between the values resulting from proton stripping reactions ( $^3\text{He}, d$ ), neutron spectroscopic factors from the  $^{24}\text{Mg}(d, p)^{25}\text{Mg}$  reaction, shell-model (SM) calculations and the present results. However, there is a discrepancy between the spectroscopic factors listed in table 5.3 and the direct capture values of Trautvetter and Rolfs [Tra75a]. This discrepancy probably results from the square-well potential with radius parameter  $r_0 = 1.36$  fm used to calculate the direct capture cross section. Column 5 lists the spectroscopic factors resulting from the direct capture cross section calculation described in chapter 2 after normalization of the experimentally determined cross section [Tra75a] to the theoretically determined cross section at  $E_p = 823$  keV via the following equation

$$\sigma_{exp} = \sum_{l_f} C^2 S(l_f) \sigma_{theo}(l_f). \quad (5.3)$$

The resulting direct capture to bound-state spectroscopic factors are in better agreement with the other spectroscopic factors listed in table 5.3. The direct

Spectroscopic Factor S						
$E_x$ (keV)	Present	$(^3\text{He},d)$ [Pet75]	DC [Tra75a]	DC Present Analysis	$(d,p)$ [Ber77] [Meu75]	SM [Meu76]
0		0.25	$0.10 \pm 0.03$	$0.30 \pm 0.08$	0.38	0.32
452		0.37	$0.43 \pm 0.09$	$0.44 \pm 0.09$	0.42	0.44
945		0.32	$0.11 \pm 0.03$	$0.32 \pm 0.08$	0.29	0.22
1613		<0.005				
1790		0.052			0.09	0.08
2485	$0.15 \pm 0.01$	0.14	$0.08 \pm 0.02$	$0.06 \pm 0.01$	0.15	0.16
2674	$0.29 \pm 0.03$	0.34			0.32	0.27

Table 5.3: The spectroscopic factors that result from the data and previous results from different types of measurements.

capture cross sections to the unbound 2485- and 2674-keV states were determined from calculations of the cross sections to a range of bound-state energies and extrapolated to the unbound energies of interest. The extrapolation using the bound-state formalism for unbound states is not in good agreement with the spectroscopic factors determined from the other measurements, and therefore should not be used for the determination of spectroscopic factors or cross sections.

## 5.2 Determination of $S(E)$

For a stellar environment at  $T_9 = 0.04$ , the energy at which the S-factor (or the cross section) needs to be determined is  $E_0 = 75 \pm 40$  keV (as described in chapter 2). The direct capture S-factor as a function of incident proton energy to each of the bound states in  $^{25}\text{Al}$  was calculated using the same procedure outlined in chapter 2 and normalized to the experimentally determined cross section of [Tra75a] at  $E_p = 823$  keV. The direct capture cross sections to the unbound 2485- and 3062-keV states are negligible relative to direct capture to

$E_{xf}$ (keV)	$l_i$	$l_f$	SM orbit
0	1,3	2	1d
451	1	0	2s
945	1,3	2	1d

Table 5.4: Input parameters used in the determination of the direct capture S-factor. The notation SM denotes Shell Model.

the 451-keV state, and therefore are not used in the determination of the total S-factor. A list of some of the parameters used in the calculation of the direct capture cross section is shown in table 5.4. The components of the S-factor from direct capture to each of the final bound states (where  $l_i$  is the initial orbital angular momentum) and the total direct capture S-factor are shown in figure 5.1. The present S-factor at  $E = 0$  is  $S(0) \approx 25$  keV b, whereas [Tra75a] quote a value of  $S(0) \approx 30$  keV b. Since the spectroscopic factors of the present direct capture calculations are more consistent with the spectroscopic factors determined with other experimental techniques, the present energy dependence of the direct capture cross section is assumed to be more reliable.

The  $E_R = 223$ -keV resonance is treated as a broad resonance in the determination of the reaction rate (see the discussion in chapter 2). A list of some of the parameters used for the determination of the  $E_R = 223$ -keV resonance S-factor for each of the final states is given in table 5.5. In addition, the values for  $\Gamma_p(E_R)$ ,  $\Gamma_\gamma(E_R)$ ,  $\Gamma(E_R)$ ,  $l_i$  and  $l_f$  are also needed. Figure 5.2 shows the  $E_R = 223$ -keV resonance S-factor to each of the final states, as well as the total, as a function of incident bombarding energy. For comparison, figure 5.3 also shows the total S-factor resulting from direct capture and the  $E_R = 223$ -keV resonance.

The remaining resonances between  $E_R = 419$  and 2409 keV ( $E_R \geq 419$  keV) are treated with the narrow-resonance approximation (see equation 2.17). The parameters needed for the narrow-resonance contributions to the reaction rate are given in table 5.6. The resonance strength values given in table 5.6 are taken

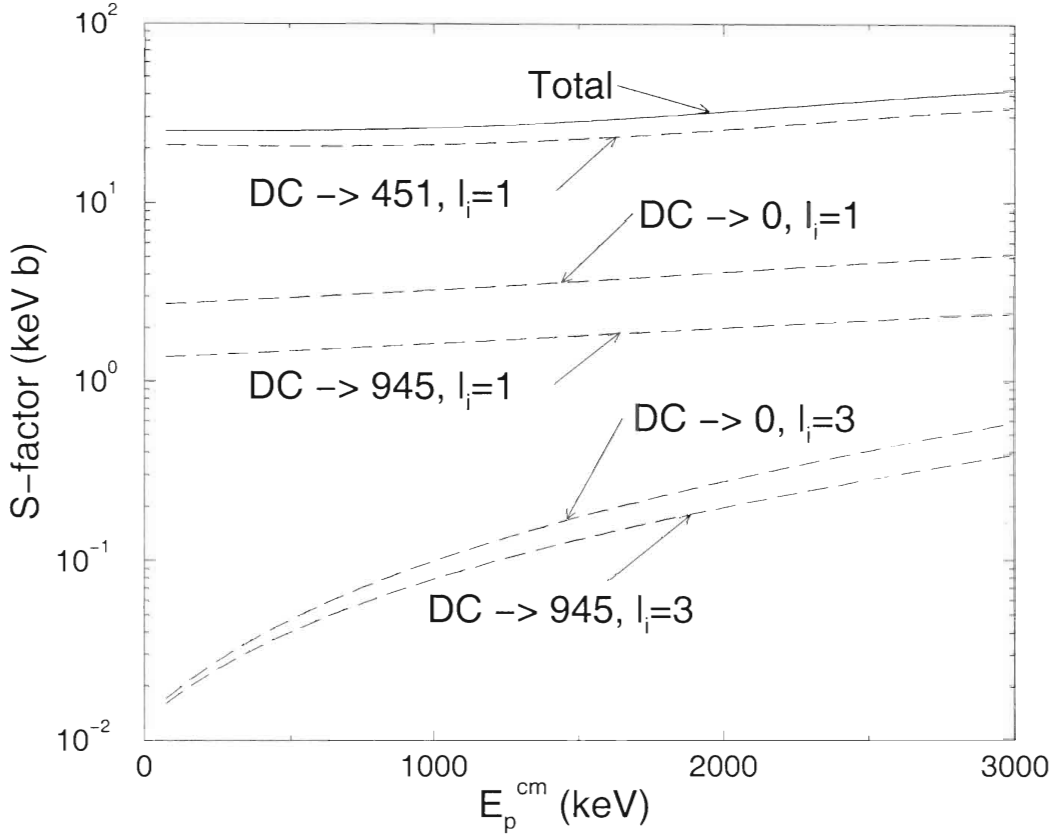


Figure 5.1: The S-factor resulting from direct capture to the labeled bound states in  $^{25}\text{Al}$  for the given initial orbital angular momentum (dashed lines) and the sum of all of the components (solid line).

$E_{x_i}$ (keV) ( $J^\pi$ )	$E_{x_f}$ (keV) ( $J^\pi$ )	$\pi L$
2485 (1/2 <sup>+</sup> )	0 (5/2 <sup>+</sup> )	E2
	451 (1/2 <sup>+</sup> )	M1
	945 (3/2 <sup>+</sup> )	M1/E2

Table 5.5: Input parameters used in the determination of the resonance capture S-factor.

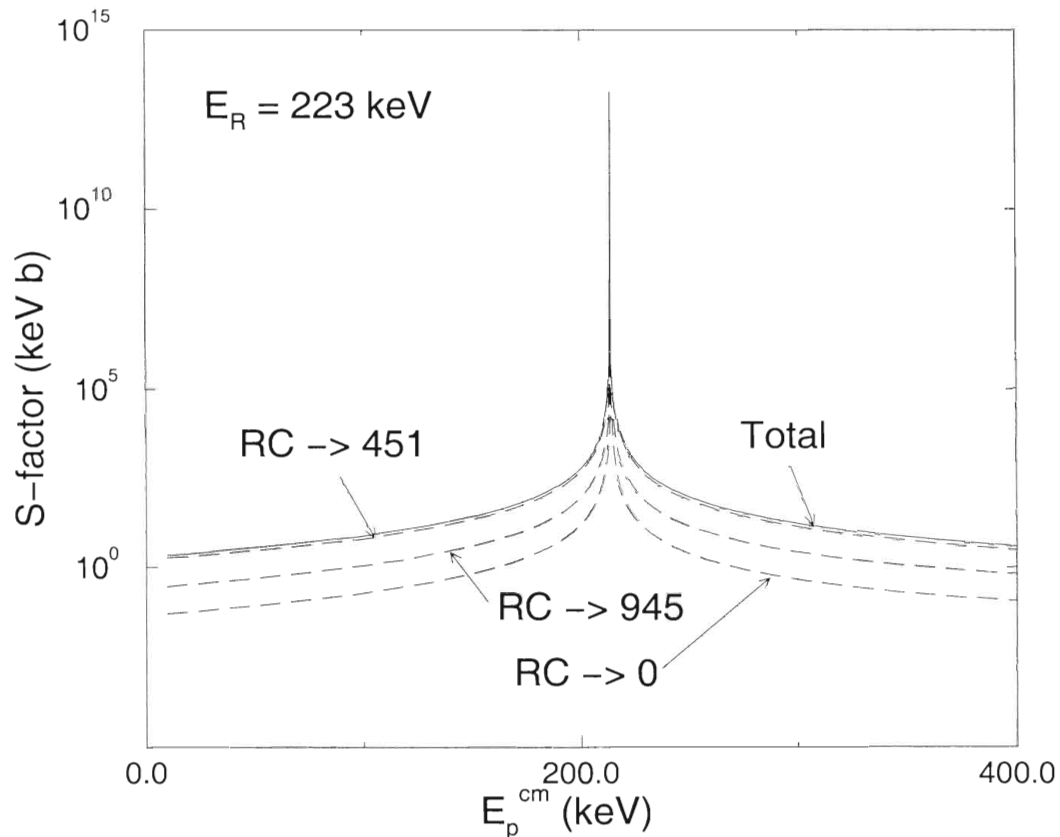


Figure 5.2: The S-factor resulting from resonance capture at  $E_R = 223$ -keV to the labeled final states in  $^{25}\text{Al}$  (dashed lines) and the sum of all of the components (solid line).

from the present and previous work [Lit56, End78, Tra75b]. The values from [End78, Tra75b] were renormalized to the present strength values determined for the  $E_R = 223$ - and 419-keV resonances. The narrow-resonance assumption is verified in section 5.4. The  $E_R = 468$ -keV resonance has not been observed via proton capture. The mean lifetime  $\tau = 310 \pm 40$  fs [End98] implies a total width  $\Gamma = 2 \times 10^{-3}$  eV. Assuming a spectroscopic factor  $S \leq 0.1$  implies a proton partial width  $\Gamma_p \leq 1 \times 10^{-4}$  eV and a resonance strength  $\omega\gamma \leq 0.4$  meV. This strength of this resonance is small in comparison with the other resonances listed in table 5.6 and is therefore not considered in the determination of the total reaction rates.

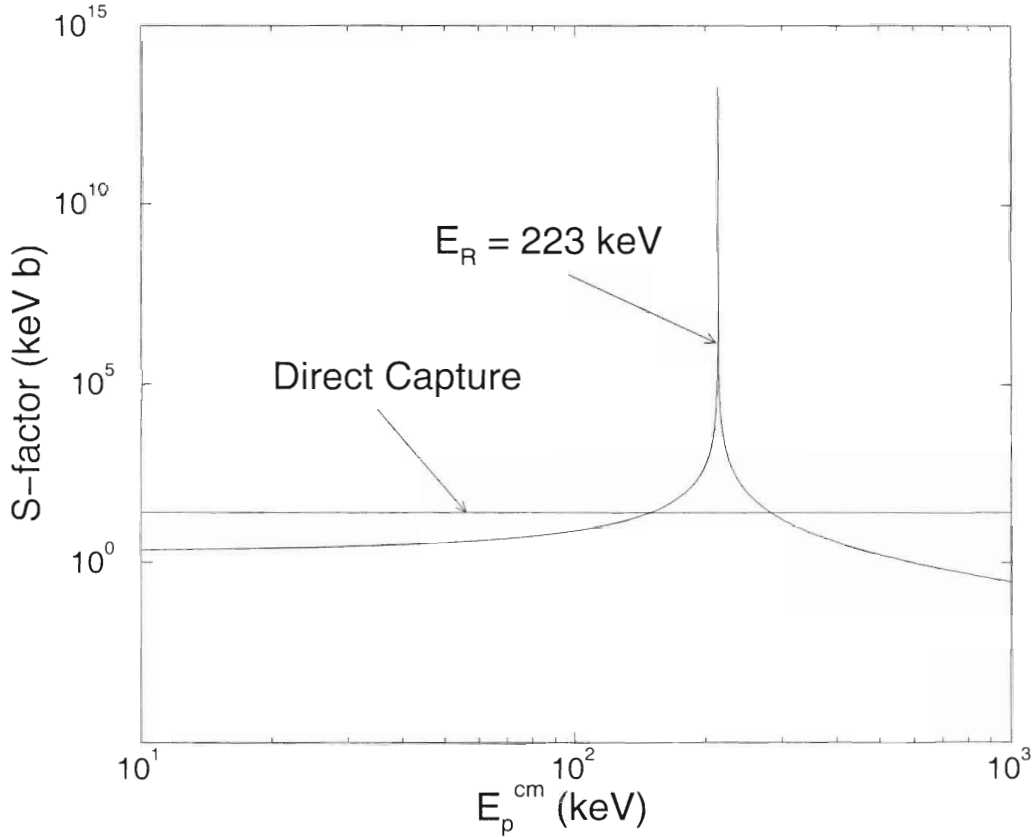


Figure 5.3: S-factor for the  $E_R = 223$ -keV resonance and direct capture in the  $^{24}\text{Mg}(p, \gamma)^{25}\text{Al}$  reaction.

### 5.3 Determination of $N_A \langle \sigma v \rangle$

A numerical integration of the reaction rate resulting from direct capture and the broad  $E_R = 223$ -keV resonance was carried out for temperatures  $T_9 = 0.02 - 2$ . At temperatures below  $T_9 = 0.02$  the mean lifetime of  $^{24}\text{Mg}$  from destruction via proton capture is significantly larger than the age of the universe (for  $X_H = 1$  and  $\rho \leq 10^6 \text{g/cm}^3$ ), and above  $T_9 = 2$  the experimental cross section resulting from resonances becomes highly uncertain. The  $E_R \geq 419$ -keV resonance contributions to the reaction rate were then added to the reaction rate describing direct capture and the  $E_R = 223$ -keV resonance. The total reaction rate, shown in figure 5.4, highlights the components that contribute significantly at the temperatures of interest. Notice that for temperatures below  $T_9 = 0.05$

$E_x$ (keV)	$E_R$ (keV)	$J^\pi$	$\omega\gamma$ (meV)	Reference
$2485.3 \pm 0.8$	$222.9 \pm 1.0$	$1/2^+$	$12.7 \pm 0.9$	Present
$2673.5 \pm 0.6$	$418.9 \pm 0.9$	$3/2^+$	$41.6 \pm 2.6$	Present
$3061.7 \pm 0.6$	$823.3 \pm 0.9$	$3/2^-$	$640 \pm 90$	[Tra75b]
$3424.3 \pm 0.5$	$1201.0 \pm 0.8$	$9/2^+(5/2^+)$	$28 \pm 6$	[Lit56]
$3695.7 \pm 0.5$	$1483.7 \pm 0.8$	$7/2^-$	$180 \pm 30$	[Tra75b]
$3823.0 \pm 1.6$	$1616.3 \pm 1.8$	$1/2^-$	$910 \pm 130$	[Tra75b]
$3858.8 \pm 0.8$	$1653.6 \pm 1.0$	$5/2^+$	$250 \pm 40$	[Tra75b]
$4026 \pm 2$	$1827.8 \pm 2.0$	$(5/2,9/2)^+$	$\sim 5$	[End78]
$4196 \pm 3$	$2005 \pm 3$	$3/2^+$	$680 \pm 100$	[Tra75b]
$4514 \pm 5$	$2336 \pm 5$	$(5/2-9/2)$	$< 0.5$	[End78]
$4583 \pm 4$	$2408 \pm 4$	$5/2^+$	$180 \pm 40$	[Lit56]

Table 5.6: The resonance energies and strengths used for the determination of the narrow-resonance reaction rate. The resonance strength values are taken from the present and previous work [Tra75b, Lit56, End78]. The values from [Tra75b, End78] were renormalized to the present, more accurate, resonance strength values of the  $E_R = 223$ - and  $419$ -keV resonances.

the reaction rate is dominated by direct capture (with a 15% contribution from the tail of the  $E_R = 223$ -keV resonance) and for temperatures above  $T_9 = 0.05$  the reaction rate is dominated by the  $E_R = 223$ -keV resonance. At  $T_9 = 1$  the  $E_R = 419$ - and  $823$ -keV resonances also contribute to the total reaction rate. Table 5.7 is a list of the reaction rates for the  $E_R = 223$ -keV resonance, the narrow resonances, the direct capture component, the total, and the previous values from Caughlan and Fowler [Cau88]. The reaction rate can be written as the following

$$\begin{aligned}
N_A \langle \sigma v \rangle = & \sum_i \frac{A_i}{T_9^{3/2}} \exp(-B_i/T_9) \\
& + C/T_9^{2/3} \exp(-D/T_9^{1/3}) \text{ cm}^3 \text{ mole}^{-1} \text{ s}^{-1}
\end{aligned} \tag{5.4}$$

where the first term describes the resonance contributions and the second term describes the direct capture contribution. The reaction rate resulting from the

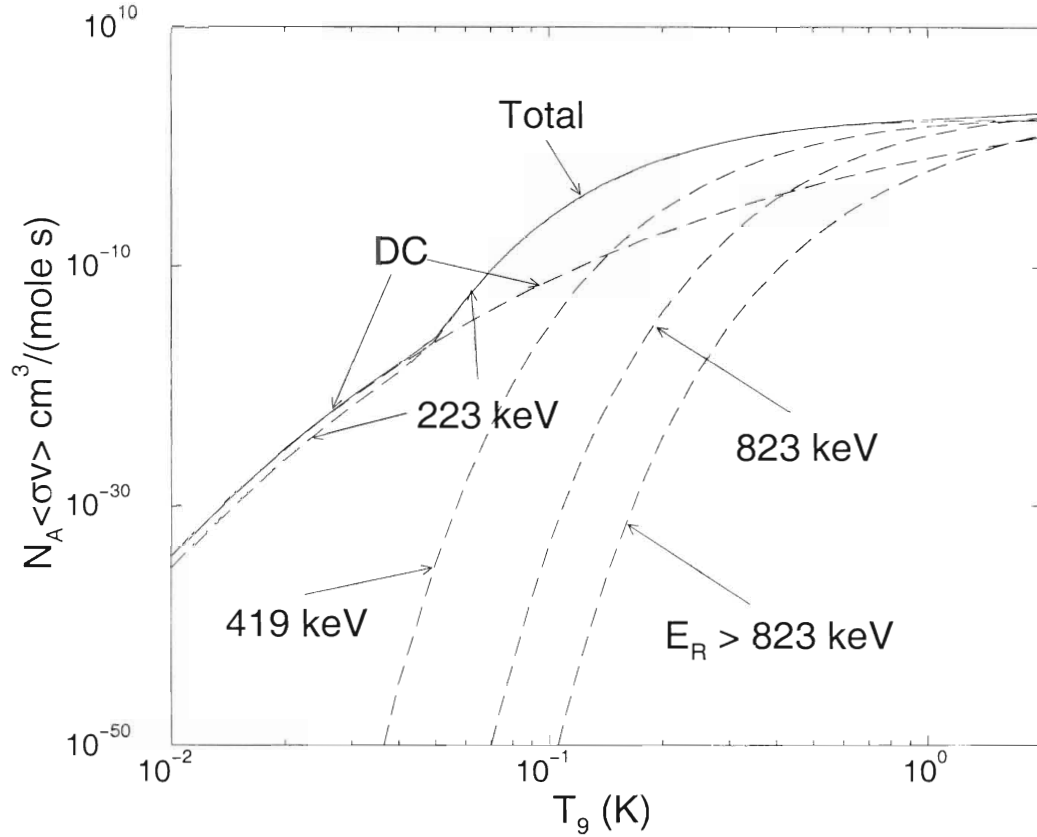


Figure 5.4: The reaction rate from direct capture and resonance capture for the  $E_R = 223, 419, 823$  and sum of all higher resonances (dashed lines) as well as the total reaction rate (solid line).

parameters given in table 5.8 are in agreement with the values listed in table 5.7 at temperatures of  $T_9 = 0.02 - 2$  to better than 10%. A plot of the ratio of the present results relative to [Cau88] is shown in figure 5.5. The present results increase the reaction rate between 18 and 45% in the temperature range of interest. The 18% increase at  $T_9 \leq 0.04$  primarily results from the tail contribution of the  $E_R = 223$ -keV resonance. This tail contribution is discussed in section 5.4. The increase for  $T_9 \geq 0.04$  results from the increase in the present resonance strength values relative to the values of [Tra75b].



$T_9$	$E_R = 223 \text{ keV}$	$E_R \geq 419 \text{ keV}$	DC	Total	[Cau88]
0.02	$6.36 \times 10^{-27}$	$1.08 \times 10^{-95}$	$4.63 \times 10^{-26}$	$5.27 \times 10^{-26}$	$4.45 \times 10^{-26}$
0.03	$1.68 \times 10^{-22}$	$3.57 \times 10^{-62}$	$9.73 \times 10^{-22}$	$1.14 \times 10^{-21}$	$9.61 \times 10^{-22}$
0.04	$1.11 \times 10^{-19}$	$1.80 \times 10^{-45}$	$5.15 \times 10^{-19}$	$6.26 \times 10^{-19}$	$5.16 \times 10^{-19}$
0.05	$6.18 \times 10^{-17}$	$1.76 \times 10^{-35}$	$4.44 \times 10^{-17}$	$1.06 \times 10^{-16}$	$7.99 \times 10^{-17}$
0.06	$1.50 \times 10^{-13}$	$7.65 \times 10^{-29}$	$1.33 \times 10^{-15}$	$1.51 \times 10^{-13}$	$1.07 \times 10^{-13}$
0.07	$4.41 \times 10^{-11}$	$4.07 \times 10^{-24}$	$1.98 \times 10^{-14}$	$4.41 \times 10^{-11}$	$3.10 \times 10^{-11}$
0.08	$3.05 \times 10^{-9}$	$1.39 \times 10^{-20}$	$1.85 \times 10^{-13}$	$3.05 \times 10^{-9}$	$2.14 \times 10^{-9}$
0.09	$8.04 \times 10^{-8}$	$7.60 \times 10^{-18}$	$1.21 \times 10^{-12}$	$8.04 \times 10^{-8}$	$5.65 \times 10^{-8}$
0.1	$1.09 \times 10^{-6}$	$1.16 \times 10^{-15}$	$6.16 \times 10^{-12}$	$1.09 \times 10^{-6}$	$7.63 \times 10^{-7}$
0.15	$2.33 \times 10^{-3}$	$3.60 \times 10^{-9}$	$1.86 \times 10^{-9}$	$2.33 \times 10^{-3}$	$1.64 \times 10^{-3}$
0.2	$9.52 \times 10^{-2}$	$5.59 \times 10^{-6}$	$6.67 \times 10^{-8}$	$9.52 \times 10^{-2}$	$6.68 \times 10^{-2}$
0.3	$3.25 \times 10^0$	$7.27 \times 10^{-3}$	$5.87 \times 10^{-6}$	$3.25 \times 10^0$	$2.29 \times 10^0$
0.4	$1.68 \times 10^1$	$2.31 \times 10^{-1}$	$9.72 \times 10^{-5}$	$1.70 \times 10^1$	$1.19 \times 10^1$
0.5	$4.15 \times 10^1$	$1.71 \times 10^0$	$7.11 \times 10^{-4}$	$4.32 \times 10^1$	$3.01 \times 10^1$
0.6	$7.23 \times 10^1$	$6.20 \times 10^0$	$3.22 \times 10^{-3}$	$7.85 \times 10^1$	$5.45 \times 10^1$
0.7	$1.04 \times 10^2$	$1.52 \times 10^1$	$1.07 \times 10^{-2}$	$1.19 \times 10^2$	$8.29 \times 10^1$
0.8	$1.32 \times 10^2$	$2.94 \times 10^1$	$2.89 \times 10^{-2}$	$1.61 \times 10^2$	$1.14 \times 10^2$
0.9	$1.56 \times 10^2$	$4.93 \times 10^1$	$6.68 \times 10^{-2}$	$2.05 \times 10^2$	$1.48 \times 10^2$
1.0	$1.76 \times 10^2$	$7.50 \times 10^1$	$1.37 \times 10^{-1}$	$2.51 \times 10^2$	$1.85 \times 10^2$
1.5	$2.19 \times 10^2$	$2.93 \times 10^2$	$1.73 \times 10^0$	$5.14 \times 10^2$	$4.02 \times 10^2$
2.0	$2.16 \times 10^2$	$6.25 \times 10^2$	$8.53 \times 10^0$	$8.50 \times 10^2$	$6.51 \times 10^2$

Table 5.7: The reaction rates in  $\text{cm}^3/(\text{mole s})$  from the  $E_R = 223\text{-keV}$  resonance, all the higher lying resonances and direct capture are summed into column 5 and compared to the previous values (column 6).

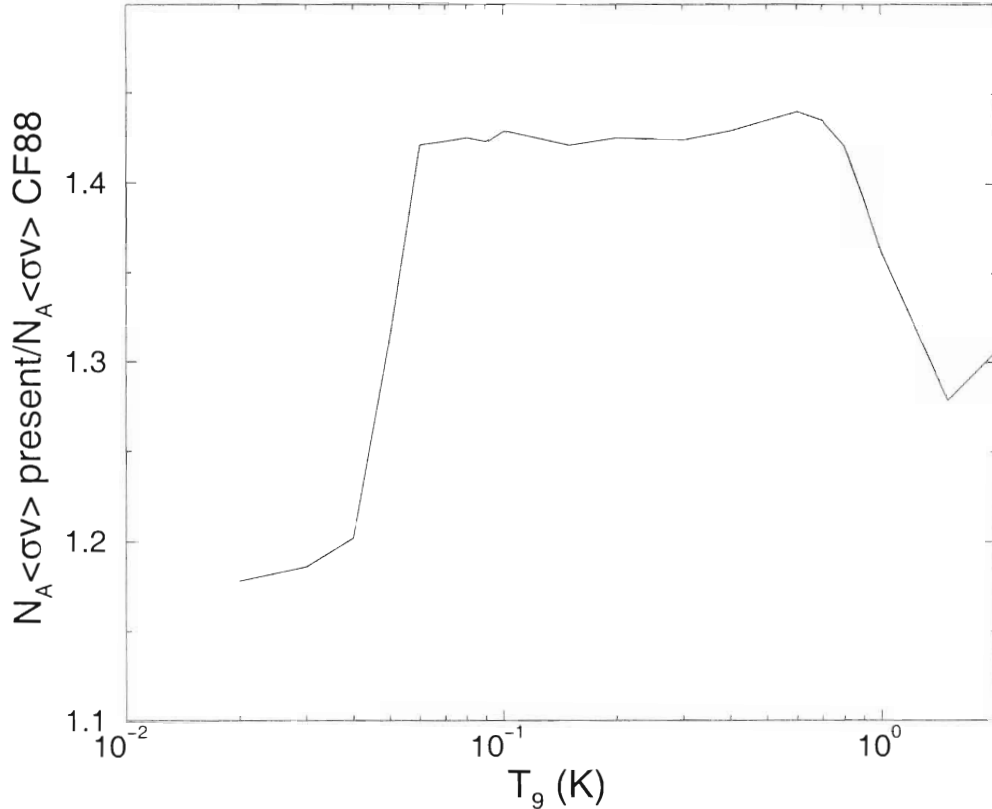


Figure 5.5: The present results for the reaction rate normalized to the previous results of Caughlan and Fowler (CF88) [Cau88].

## 5.4 Reaction Rate Uncertainties

### 5.4.1 Statistical Uncertainties

Among the possible sources of error in the reaction rates is the uncertainty in the experimentally determined values, for example, the direct capture cross section [Tra75a], the  $E_R = 223$ -keV resonance energy, strength  $\omega\gamma$  and total width  $\Gamma$ . By allowing each of these parameters to vary independently by one standard deviation, the following implications for the total reaction rate were estimated: The uncertainty in the direct capture cross section ( $\sim 17\%$ ) leads to uncertainty of  $\sim 17\%$  in the reaction rate for temperatures lower than  $T_9 = 0.05$ . The uncertainty (1 keV) in the energy of the  $E_R = 223$ -keV resonance leads to

$A_i$	$B_i$	$C$	$D$
2148	2.485	$4.52 \times 10^8$	21.92
$3.18 \times 10^4$	6.0		

Table 5.8: Reaction rate fit parameters for use in equation 5.4 for  $T_9 = 0.02 - 2$ . The agreement between the fit and the actual value is better than 10% at all temperatures.

an uncertainty ranging from 10 to 20% for  $T_9 = 0.05 - 0.2$ . The uncertainty in the resonance strength ( $\sim 7\%$  with  $\Gamma$  fixed at 155 meV) leads to less than an 8% uncertainty between  $T_9 = 0.06 - 1.0$ . Finally, the uncertainty in the total width ( $\sim 26\%$  with  $\omega\gamma$  fixed at 12.7 meV) has less than a 2% effect on the reaction rate.

### 5.4.2 Systematic Uncertainties

Several sources of systematic uncertainties may contribute to uncertainties in the total reaction rate. Uncertainties resulting from competing resonance  $\gamma$ -ray decay modes, interferences between direct and resonance capture, the narrow-resonance approximation, an improper extrapolation of the tail of the  $E_R = 223$ -keV resonance, contributions from subthreshold states and the existence of an unobserved resonance are discussed.

The uncertainty of how a resonance may decay, *i.e.* via competing E2 and/or M1 transitions, may lead to uncertainties in the total reaction rate. The  $\gamma$ -ray decay plays a role in the extrapolation of  $\Gamma_\gamma$  since this quantity depends on the multipolarity  $L$  of the  $\gamma$ -ray (see equation 2.16). Since it is not clear how much of each transition may contribute, the effect on the S-factor resulting from the two types of decay was calculated. The candidate for competing E2 and M1 transitions is the  $E_x = 2485 \rightarrow 945$ -keV transition. Since the S-factor is dominated at the temperatures of interest by direct capture and the  $E_x = 2485 \rightarrow 451$ -keV transition, the uncertainty in the decay multipolarity had less than

a 1% effect on the total reaction rate.

The channel radius  $a$  is given by  $a = a_0(A_t^{1/3} + A_p^{1/3})$  where  $a_0 = 1.25$  fm (or  $a = 4.86$  fm) and is necessary for calculation of the penetration factor and the dimensionless single-particle reduced width used to determine of the resonance capture cross section. Changing the channel radius by 20% (to  $a = 5.83$  fm) leads to at most a 4% change in the  $E_R = 223$ -keV resonance capture cross section, and therefore has a negligible effect on the total reaction rate.

Interference effects between resonances and between direct and resonant capture can shift the energy dependence of the S-factor, and therefore affect the reaction rate. In order for resonances to interfere with one another they must share the same  $J^\pi$ . The only resonances that contribute significantly to the reaction rate in the temperature range of interest are the  $E_R = 223$ -keV ( $1/2^+$ ), 419-keV ( $3/2^+$ ) and the 823-keV ( $3/2^-$ ) resonances which cannot interfere in the total cross section with one another. From inspection of figure 5.4, it is apparent that in the temperature range of interest, the only location where direct capture and resonance capture are comparable and significantly contribute to the reaction rate is at  $T_9 \sim 0.05$ . The determination of the magnitude of the effect of interferences on the S-factor between direct capture and the  $E_R = 223$ -keV resonance can be determined from an evaluation of equation 2.4. The value for the Racah coefficient, given by  $W(l_R L_R J_1 J_3; l_f J_2)$  in equation 2.8, for  $l_R = 0$  and  $L_R = 1$  and  $l_f = 0$  or 2 is zero. Therefore  $W_{R,D}^{int}(\theta)$  is zero at all angles and the interference term in equation 2.4 is zero. If the resonance capture to the ground state proceeds via E2 decay, then  $W(l_R L_R J_1 J_3; l_f J_2) \neq 0$ , but  $\bar{Z}(l_R L_R L_D L_D; l_f m) = 0$  and therefore, all interference effects are negligible in this reaction for the temperatures presented in the present work.

Upon evaluation of figure 5.4, one might notice that the reaction rate resulting from a narrow resonance drops off smoothly at the lower temperature, whereas the reaction rate resulting from the numerical integration (the  $E_R = 223$ -keV resonance) is enhanced at the lower temperatures. The reaction rate resulting

from the narrow-resonance approximation and the numerical integration of the S-factor for the  $E_R = 223$ -keV resonance is shown in figure 5.6. The enhancement at the lower temperatures is what is referred to in this thesis as the tailing effect. The narrow-resonance approximation assumes that the dominant contribution to the reaction rate comes from the product of the Gamow peak with the S-factor near the resonance energy, which is why the plots are consistent at  $T_9 \geq 0.05$ . At the lower temperatures the largest contribution to the reaction rate may result from the product of the Gamow peak and the S-factor near  $E_0$ , and an enhancement in the reaction rate relative to the narrow-resonance approximation (see figure 5.6). This tailing effect can be ignored for all resonances above  $E_R = 223$  keV because the contribution of the tails to the total reaction rate is insignificant relative to direct capture. The narrow-resonance approximation cannot be used for the  $E_R = 223$ -keV resonance because the total reaction rate at  $T_9 < 0.05$  is enhanced by  $\sim 15\%$  as a result of the tail of the  $E_R = 223$ -keV resonance.

An additional source of uncertainty may result from the extrapolation of the Breit-Wigner cross section over a *million* total widths ( $\sim 200 \rightarrow 75$  keV) to astrophysically interesting energies. An indication of the quality of the Breit-Wigner extrapolation over  $10^6$  total widths can be estimated from the data of Rolfs and Winkler [Rol74]. They measured the  $^{20}\text{Ne}(p, \gamma)^{21}\text{Na}$  cross section for  $E_p = 0.5 - 1.5$  MeV, and determined the contribution from the subthreshold resonance corresponding to the 2425-keV excited state in  $^{21}\text{Na}$ . The total width of the 2425-keV state was determined from a DSAM measurement and implies  $\Gamma_\gamma = 170$  meV [Ant77]. The spectroscopic factor was determined from a  $^{20}\text{Ne}(d, n)^{21}\text{Na}$  experiment and yielded  $C^2S = 0.96$  [Ter93], which allows for calculation of the proton partial width via equation 5.2. A comparison of the calculated cross section using the parameters mentioned above and the experimental data presented in reference [Rol74] shows that extrapolation of the Breit-Wigner cross section to energies  $10^7$  total widths from the resonance energy is in agreement to better

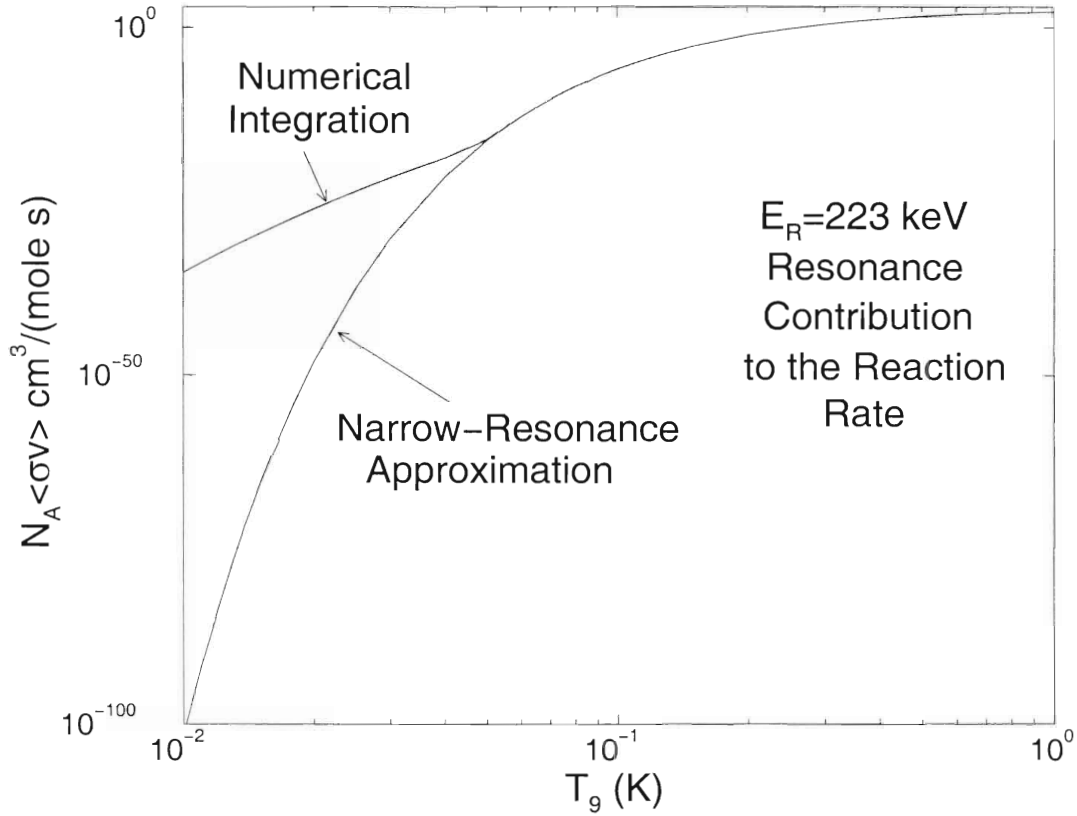


Figure 5.6: The reaction rate for the  $E_R = 223$ -keV resonance resulting from the numerical integration and the narrow-resonance approximation.

than 30%.

The effect of an uncertainty in the extrapolation of the Breit-Wigner cross section for the present work was investigated by varying the total width of the  $E_R = 223$ -keV resonance. If the present value of the total width is increased by a factor of 2 (10), this leads to a factor of 2 (10) increase in the S-factor for this resonance at  $E_0 = 75$  keV, but an increase in the reaction rate by less than a factor of 1.2 (3) for  $T_9 \leq 0.05$ . The Breit-Wigner extrapolation has been shown to properly predict the cross section at energies far from the resonance and the rate for  $^{24}\text{Mg}(p, \gamma)^{25}\text{Al}$  reaction is also not very sensitive to large enhancements in the  $E_R = 223$ -keV S-factor at the temperatures of interest. Therefore, the extrapolation procedure is believed to have an insignificant effect on the overall

reaction rate. One way to test the accuracy of the extrapolation is to measure the cross section on the low-energy wing of the  $E_R = 223$ -keV resonance. A direct measurement of the  $\gamma$ -ray yield at  $E_0 = 75$  keV (at the Gamow energy for  $T_9 = 0.04$ ) with a 10-keV-thick Mg target and 1 mA of beam implies approximately one count every 100 years. For an incident bombarding energy of  $E_p = 150$  (200) keV a  $\gamma$ -ray yield of  $\sim 9$  (4000) per day is expected, and could be a reasonable test of the extrapolation procedure.

Contributions from subthreshold states to the reaction rate is expected to be dominated by capture to the  $E_x = 1790$ -keV state ( $5/2^+$ ). The other bound states are either narrow, have a high centrifugal barrier, and/or have very small spectroscopic factors. The  $E_x = 1790$ -keV state is bound by 481 keV and would proceed via  $l_i = 2$ , or d-wave capture, with a  $\gamma$ -ray partial width  $\Gamma_\gamma \approx \Gamma = 1.2 \times 10^{-3}$  eV calculated from the mean lifetime [End90], and the proton spectroscopic factor of  $S = 0.052$  from table 5.3. The S-factor at the low bombarding energies, corresponding to the reaction rate at the lowest temperatures, resulting from the subthreshold resonance is negligible in comparison with the contribution from direct capture.

It was suggested by Denissenkov *et al.* [Den98] that an undetected low-energy resonance in the  $^{24}\text{Mg}(p, \gamma)^{25}\text{Al}$  reaction could also lead to an enhancement in the total reaction rate. Calculations of the enhancement in the reaction rate were performed assuming that the resonance strength of the undetected state is given by

$$\omega\gamma = 2 \frac{\hbar^2}{\mu a^2} P_l(E_R) \theta_{sp}^2(E_R) \quad (5.5)$$

where  $C^2S \equiv 1$  and the resonance is formed via s-wave capture. For a given temperature, the maximum enhancement in the reaction rate was determined from a range of resonance energies. The maximum enhancement in the reaction rate relative to the values presented in table 5.7 for  $T_9 = 0.02 - 0.2$  are shown in figure 5.7. The largest possible enhancement ( $\sim 10^7$ ) corresponds to a resonance at  $E_R \sim 60$  keV. In an attempt to rule out significant contributions to the

reaction rate from a low energy resonance,  $({}^3\text{He},d)$  measurements were considered. The  $({}^3\text{He},d)$  experiments would need to yield spectroscopic factors on the order of  $10^{-5}$ – $10^{-6}$  in order to eliminate the possibility of contributions from an undetected state. This level of sensitivity does not seem feasible.

Although there is no way to absolutely rule out the contribution of an undetected state corresponding to a proton energy  $E_p < 223$  keV, it is *extremely unlikely*. The  ${}^{25}\text{Al}$  excitation energy range of interest has been studied extensively in  $\gamma$ -ray spectroscopy, particle-transfer and  $\beta$ -decay experiments [End90]. From the available experimental data a one-to-one correspondence between observed  ${}^{25}\text{Al}$ - ${}^{25}\text{Mg}$  mirror states has been established up to an excitation energy of  $E_x = 5$  MeV [End90]. In addition, the structure of  ${}^{25}\text{Al}$  and  ${}^{25}\text{Mg}$  has been successfully interpreted in the framework of the collective model [Lit58] and the shell model [End98]. Neither experimental data nor theoretical calculations predict the existence of a new state below an energy of  $E_x = 5$  MeV.

## 5.5 Implications of the Reaction Rate

Cavallo *et al.* [Cav98] explored the abundance profiles of the Mg and Al isotopes using the most up-to-date reaction rates and compared the calculations with the observations of Shetrone [She96]. The calculations show that the initial enhancement in Al results from proton capture on  ${}^{25}\text{Mg}$  and  ${}^{26}\text{Mg}$  (see figure 5.8). The  ${}^{24}\text{Mg}(p,\gamma){}^{25}\text{Al}$  reaction is the source of any further enhancement in Al, which is required in order to match the observed 1.0 dex increase in Al (where 1.0 dex equals a factor of 10). If the temperature in the shell is hot enough to allow the  ${}^{24}\text{Mg}(p,\gamma){}^{25}\text{Al}$  reaction to produce Al, but constrained by the model to be  $< 0.055$  GK, then the  ${}^{23}\text{Na}(p,\gamma){}^{24}\text{Mg}$  reaction will lead to an enhancement in the abundance of  ${}^{24}\text{Mg}$  (see figure 5.8). Therefore, enhancements in Al should be correlated with  ${}^{24}\text{Mg}$ , in contradiction to the observations of Shetrone [She96].

Cavallo *et al.* also examined nuclear uncertainties in the MgAl region that



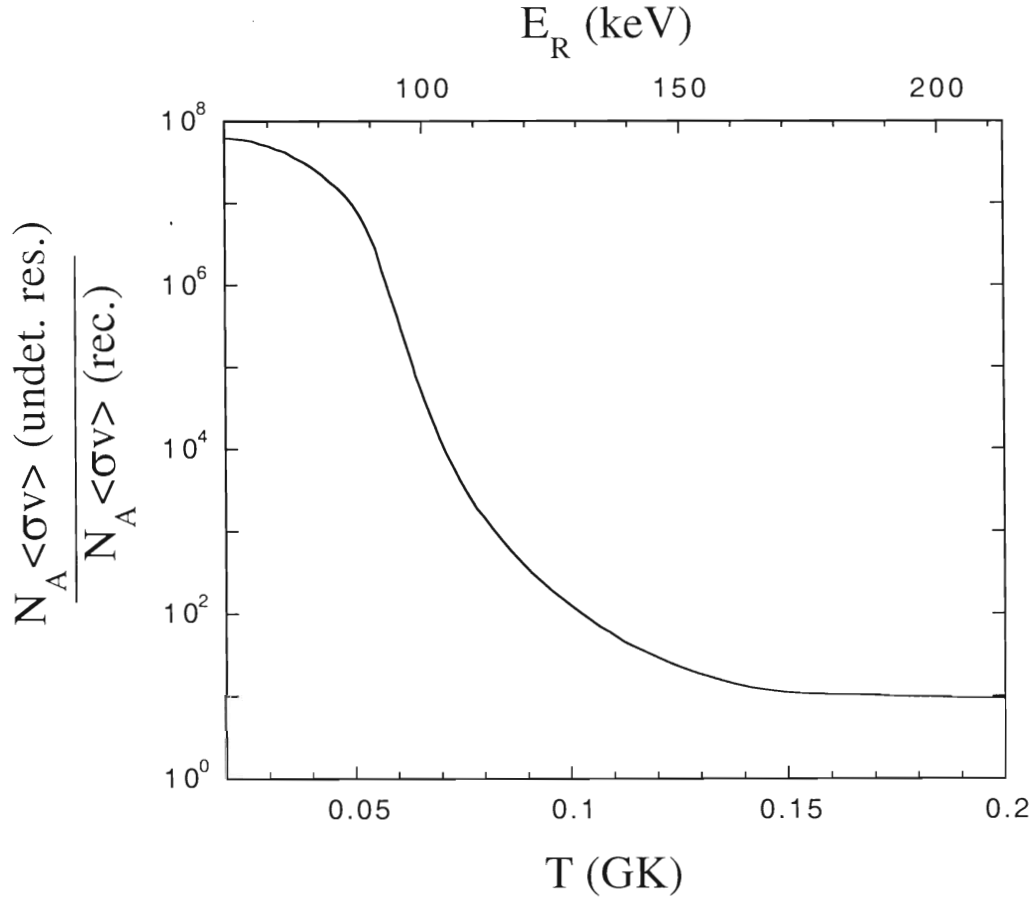


Figure 5.7: The maximum enhancement of the reaction rate permitted from an undetected resonance at  $E_R < 223$  keV for temperatures between  $T_9 = 0.02 - 0.2$ .

could affect the production and destruction of  $^{24}\text{Mg}$  in an attempt to understand the observations of Shetrone [She96]. The uncertainties in the  $^{25}\text{Mg}(p, \gamma)$ ,  $^{26}\text{Mg}(p, \gamma)$ ,  $^{23}\text{Na}(p, \gamma)^{24}\text{Mg}$ , and  $^{27}\text{Al}(p, \alpha)^{24}\text{Mg}$  reactions, in addition to the total elimination of the  $^{23}\text{Na}(p, \gamma)^{24}\text{Mg}$  and the  $^{27}\text{Al}(p, \alpha)^{24}\text{Mg}$  reactions (producers of  $^{24}\text{Mg}$ ), could not account for the 0.4 dex depletion ( $0.4 \text{ dex} = 10^{0.4} = 2.5$ ) in  $^{24}\text{Mg}$  observed by Shetrone. If the  $^{24}\text{Mg}(p, \gamma)^{25}\text{Al}$  reaction was the source of discrepancy between the observations and calculations, Cavallo *et al.* claimed the  $^{24}\text{Mg}(p, \gamma)^{25}\text{Al}$  reaction rate would have to be increased by at least a factor of 35.

The total width of the  $E_R = 223$ -keV resonance previously allowed for an

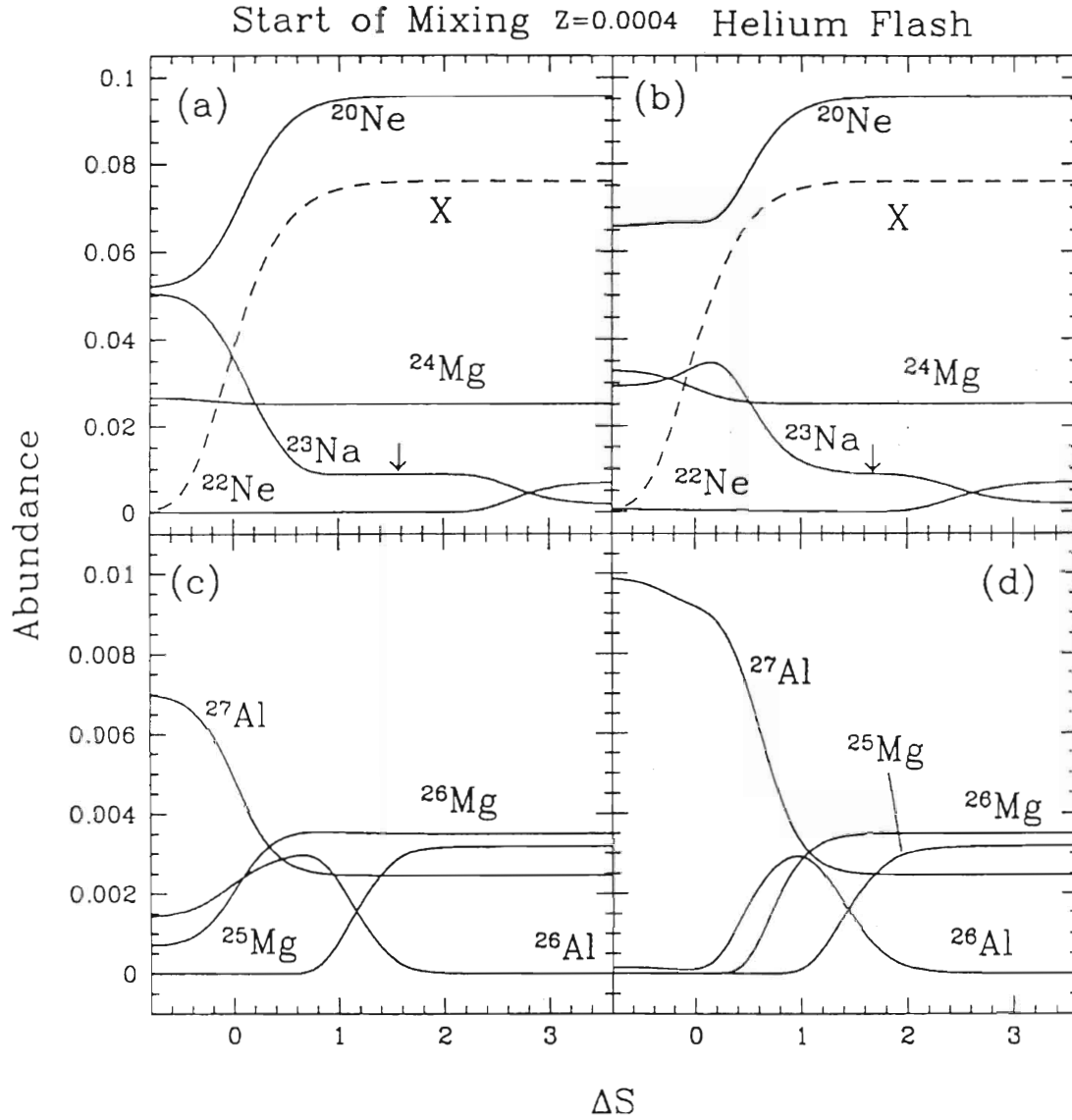


Figure 5.8: The NeNa and MgAl mass regions for a  $Z = 0.0004$  metallicity star at the start of mixing (*left*) and at the tip of the red giant branch (*right*) [Cav98]. The dashed line is the hydrogen-mass fraction scaled by a factor of 10. The horizontal axis  $\Delta S$  is the mass difference between any point and the center of the H shell divided by the H-shell thickness.

increase in the reaction rate of up to a factor of 32 at  $T_9 = 0.04$  [Zai97]. The present reaction rate has been established in the temperature range  $T_9 = 0.02 - 2$ , with statistical uncertainties less than 20%. The largest potential source of systematic uncertainty in the reaction rate at the temperatures of interest results from the possibility of an undetected low energy resonance. Based on the current experimental and theoretical understanding of the  $^{25}\text{Al}$  level structure, this possibility appears *extremely unlikely*. The present results increase the total  $^{24}\text{Mg}(p, \gamma)^{25}\text{Al}$  reaction rate by at most a factor of 1.5, and therefore the discrepancy between the models and the observations are not nuclear in origin.

There exist a number of areas of concern outside the realm of nuclear physics that need to be addressed. For example, how does one model the deep mixing process in a realistic way? In addition, what is the source of the abundance variations, primordial or evolutionary, or a combination of the two? If, for example, observations could be made lower on the red giant branch, the source of the elemental variations could be determined. In addition, the  $^{24}\text{Mg}$  versus Al observations result from one study of a small number of stars in a single cluster. It would be beneficial if observations of the Mg isotopes in other globular clusters, or for a larger number of stars, could be obtained to verify the work of Shetrone.

The anticorrelation of Al with Mg has been supported by a number of observations. From the calculations of [Cav98] (see figure 5.8 where  $\Delta S \sim 0.5-1$ ), the only time when Na is enhanced, O is depleted, Mg is depleted and Al is enhanced (following the trends of the observations) is when the depletion in Mg results from the destruction of  $^{25}\text{Mg}$  and  $^{26}\text{Mg}$ . If one were to have faith in the nuclear physics and believe that the astronomical observation trends (excluding Shetrone) were the result of deep mixing at  $T_9 < 0.055$  and primordial abundance variations, one possible solution to the discrepancy between the models and the observation would be to significantly enhance the red giant branch stars in  $^{25}\text{Mg}$  and  $^{26}\text{Mg}$  relative to  $^{24}\text{Mg}$  [Smi96]. Since this enhancement cannot occur from nuclear pro-

cesses in a previous stage of the stars evolution, the enhancement would have to be primordial in origin. One source of enhancement in  $^{25}\text{Mg}$  and  $^{26}\text{Mg}$  was suggested by Smith and Kraft [Smi96] to originate from material ejected from O-Ne-Mg novae, and has not been ruled out as a possibility [Lan95, Smi96].

Another possible explanation for the observations results from the possibility that the temperature exceeds  $T_9 = 0.055$ , allowing the  $^{24}\text{Mg}(p, \gamma)^{25}\text{Al}$  reaction to proceed at a higher rate. This scenario was postulated by Langer *et al.* [Lan95] and requires hydrogen flashes, or thermal instabilities in the star. An average temperature of  $T_9 = 0.07$  allows for the proper prediction of the Na and Al enhancements, the Mg and  $^{24}\text{Mg}$  depletions, and  $[(^{25}\text{Mg}+^{26}\text{Mg})/^{24}\text{Mg}]$  ratio. It has been argued by Rudloff *et al.* [Rud88] that the probability for these instabilities decreases as the star evolves along the red giant branch. However Rudloff *et al.* admit that the stability is marginal and instabilities could be more likely if rotation is taken into account.

In the present work, it has been shown that the uncertainty in the total width  $\Gamma$  of the  $E_R = 223\text{-keV}$  resonance in  $^{24}\text{Mg}(p, \gamma)^{25}\text{Al}$  has a negligible effect on the reaction rate at  $T_9 = 0.02 - 2$ . Therefore, it is no longer a potential source of the discrepancy between the observations and calculations. After an in-depth investigation of the NeNa and MgAl mass regions for  $T_9 \leq 0.055$ , Cavallo *et al.* have shown that the discrepancy between the observations and the theory cannot be explained by uncertainties in the nuclear physics [Cav98]. Therefore, the solution must originate from new observations or from a better understanding of the stellar environment where the nuclear reactions take place.

# Appendix A

## $F(\tau)$ Program

### A.1 Execution Commands

The following is the sequence of commands to execute the FITFTAU.FOR program:

```
>run fitftau
```

Name the input file:

```
>almgta.inp
```

Input the initial lifetime value and the lifetime of the feeding state in (fs):

```
>1.0,0.001
```

Would you like to generate an  $F(\tau)$  curve (or determine  $F(\tau)$  only for the lifetime given above)?

```
>Y
```

Input the final lifetime value (fs) for the  $F(\tau)$  curve.

```
>20
```

Warning: It takes a while, so be patient. The output file (fitftau.out) contains two columns containing the lifetime and its corresponding  $F(\tau)$  value. It is also recommended, for the consideration of other computer users, to run the program in batch mode.

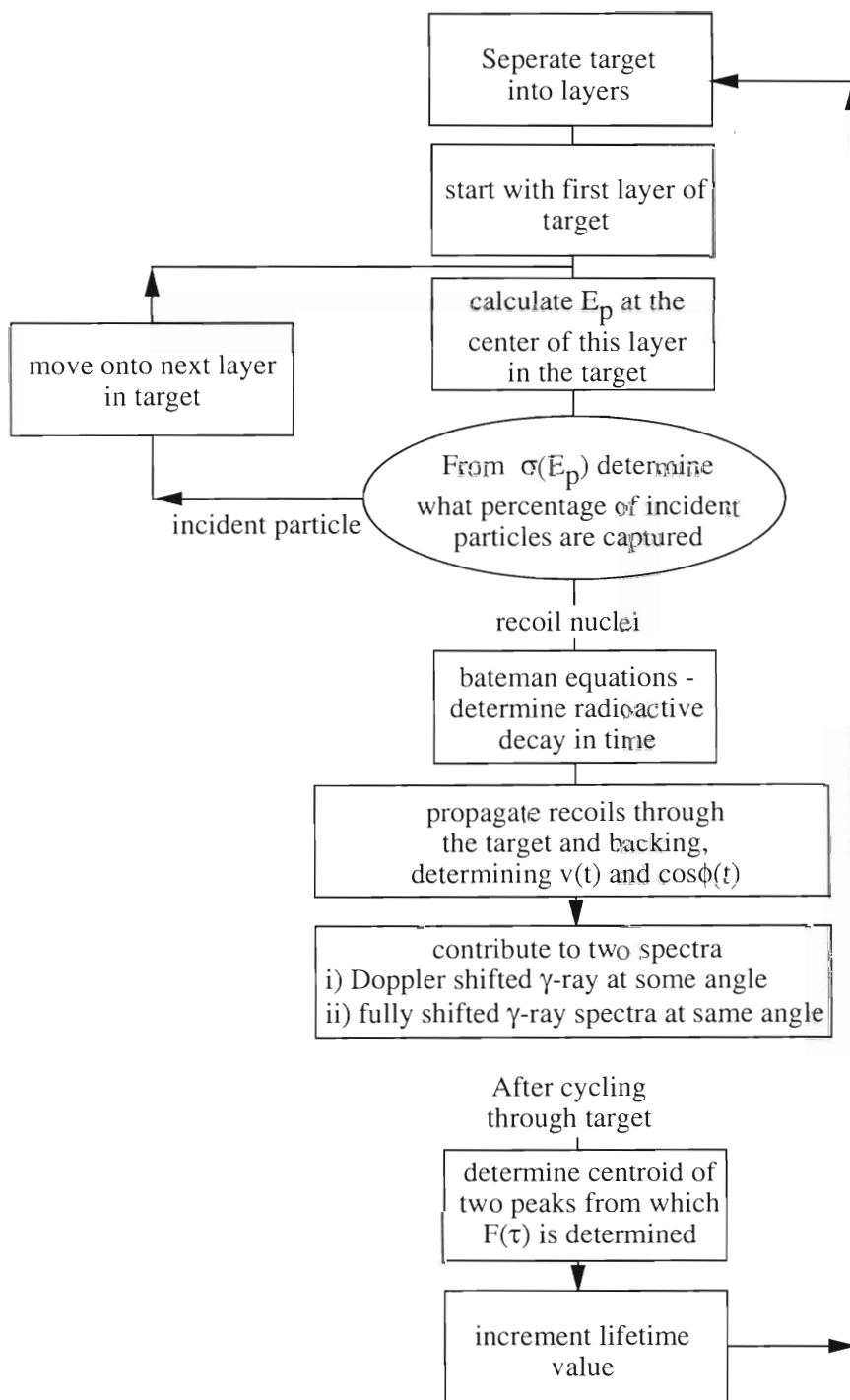


Figure A.1: An outline of the FITFTAU program adopted from E. Frank Moore and modified to properly handle low energy reactions and to create  $F(\tau)$  curves.

## A.2 Input Files

A sample input file with comments is given below.

### SAMPLE INPUT FILE FOR FITFTAU PROGRAM

25Al in a Mg and Ta target            $\Leftarrow$  descriptive title  
stopA.stp                            $\Leftarrow$  file from which to read the data  
13, 25                                $\Leftarrow$  recoil Z, A

### SAMPLE DATA INPUT FILE FOR FITFTAU PROGRAM

<sup>25</sup>Al in a Mg and Ta target - TRIM stopping  $\Leftarrow$  descriptive title  
1, 1.62                                $\Leftarrow$  projectile mass, energy (MeV)  
12, 24, 73, 181                    $\Leftarrow$  target Z, A; backing Z, A  
13, 25, 1, .05                    $\Leftarrow$  recoil Z, A; Blaugrund flags  
1.0, 14                               $\Leftarrow$  projectile stopping power  
                                      normalization and number of  
                                      entries to read  
0.6500E+00, 0.08255                $\Leftarrow$  projectile energy (MeV),  
0.7000E+00, 0.08017               (dE/dx)<sub>tot</sub> (MeV/mg/cm<sup>2</sup>) taken  
0.8000E+00, 0.07591               from TRIM  
.  
.  
.  
0.1700E+01, 0.05335  
5, 0.010, 4600., 1.                $\Leftarrow$  number of layers to subdivide  
                                      target into, target thickness in  
                                      mg/cm<sup>2</sup>, target density in mg/cm<sup>3</sup>,  
                                      normalization for target  
                                      stopping power  
1.0, 1.0                              $\Leftarrow$  relative normalizations for

1, 20., 16600.	for $(dE/dx)_{elec}$ , $(dE/dx)_{nuc}$ $\Leftarrow$ number of backing layers, thickness of backing in $mg/cm^2$ , density of backing in $mg/cm^3$
2.12, 0.67, 1.0	$\Leftarrow$ relative normalizations for $(dE/dx)_{elec}$ , $(dE/dx)_{nuc}$ , $(dE/dx)_{tot}$ for each layer in backing as given by TRIM
128	$\Leftarrow$ number of tabulated stopping powers to read for target
0.1000E-05, 0.00366, 0.00617	$\Leftarrow$ energy (MeV), $(dE/dx)_{elec}$ ,
0.1100E-05, 0.00384, 0.00657	$(dE/dx)_{nuc}$ for recoil in target
0.1200E-05, 0.00401, 0.00698	material ( $MeV/mg/cm^2$ ) as given
0.1300E-05, 0.00414, 0.00735	by TRIM
.	
.	
.	
0.7000E-01, 0.96388, 0.54455	
129	$\Leftarrow$ number of tabulated stopping powers to read for backing
0.0000E-00, 0.00010, 0.00010	$\Leftarrow$ energy (MeV), $(dE/dx)_{elec}$ ,
0.1000E-05, 0.00062, 0.00176	$(dE/dx)_{nuc}$ for recoil in backing
0.1100E-05, 0.00065, 0.00188	layer ( $MeV/mg/cm^2$ ) as given
0.1200E-05, 0.00068, 0.00200	by TRIM
.	
.	
.	
0.7000E-01, 0.16321, 0.25170	
5	$\Leftarrow$ number of entries of $\sigma(E)$



	table. Use if production
	cross section varies across
	the target thickness
1.65, 1.635, 1.62, 1.605, 1.590	⇐ max to min beam energy
	tabulated in MeV
0., 50., 100., 50., 0.	⇐ RELATIVE cross section (in %)
	for the above mentioned energies
1	⇐ start the calculation



# REFERENCES

- [And80] M. R. Anderson, S. R. Kennett, L. W. Mitchell, and D. G. Sargood, Nucl. Phys. **A349**, 154 (1980).
- [Ant77] A. Anttila, J. Keinonen, and M. Bister, J. Phys. G **3**, 1241 (1977).
- [Ant82] A. Anttila, M. Bister, and A. Luukkainen, Nucl. Phys. **A385**, 194 (1982).
- [Ars90] K. Arstila, J. Keinonen, and P. Tikkanen, Phys. Rev. B **41**, 6117 (1990).
- [Aud95] G. Audi and A. H. Wapstra, Nucl. Phys. **A595**, 409 (1995).
- [Aud97] G. Audi, O. Bersillon, J. Blackot, and A. H. Wapstra, Nucl. Phys. **A624**, 1 (1997).
- [Bec82] H. W. Becker, W. E. Kieser, C. Rolfs, H. P. Trautvetter, and M. Wiescher, Z. Phys. **A305**, 319 (1982).
- [Ber77] G. P. A. Berg, R. Das, S. K. Datta, and P. A. Quin, Nucl. Phys. **A289**, 15 (1977).
- [Bev92] P. R. Bevington and D. K. Robinson, *Data Reduction and Error Analysis for the Physical Sciences*, McGraw-Hill, 1992.
- [Bie53] L. C. Biedenharn and M. E. Rose, Rev. Mod. Phys. **25**, 729 (1953).
- [Bla66] A. E. Blaugrund, Nucl. Phys. **88**, 501 (1966).
- [Bla93] T. C. Black, B. E. Hendrix, E. R. Crosson, K. A. Fletcher, H. J. Karwowski, and E. J. Ludwig, Nucl. Instr. Meth. **A333**, 239 (1993).
- [Bre36] G. Breit and E. Wigner, Phys. Rev. **49**, 519 (1936).
- [Bri94] M. M. Briley, R. A. Bell, J. E. Hesser, and G. H. Smith, Can. J. Phys. **72**, 772 (1994).
- [Bru94] C. R. Brune, Ph.D. thesis, California Institute of Technology, 1994.
- [Buc80] L. Buchmann, H. W. Becker, K. U. Kettner, W. E. Kieser, P. Schmalbrock, and C. Rolfs, Z. Phys. **A296**, 273 (1980).

- [Bun56] D. S. P. Bunbury et al., Proc. Phys. Soc. **A69**, 165 (1956).
- [Bur57] E. M. Burbidge, G. R. Burbidge, W. A. Fowler, and F. Hoyle, Rev. of Mod. Phys. **29**, 547 (1957).
- [Cau88] G. R. Caughlan and W. A. Fowler, At. Data Nucl. Data Tables **40**, 283 (1988).
- [Cav98] R. M. Cavallo, A. V. Sweigart, and R. A. Bell, Astrophys. J. **492**, 575 (1998).
- [Chu78] W. Chu, J. W. Mayer, and M. Nicolet, *Backscattering Spectrometry*, Academic Press, 1978.
- [Cro91] S. Croft, Nucl. Instr. Meth. **A307**, 353 (1991).
- [Cur69] W. M. Currie, Nucl. Instr. Meth. **73**, 173 (1969).
- [Deb88] K. Debertin and R. G. Helmer, *Gamma- and X-ray Spectrometry with Semiconductor Detectors*, Elsevier Science Publishing Company, Inc., 52 Vanderbilt Ave., New York, NY 10017, 1988.
- [Den98] P. A. Denissenkov, G. S. D. Costa, J. E. Norris, and A. Weiss, Astron. Astrophys. **333**, 926 (1998).
- [Dev49] S. Devons and M. G. N. Hine, Proc. Roy. Soc. **A199**, 73 (1949).
- [Dev55] S. Devons et al., Proc. Phys. Soc. **A68**, 18 (1955).
- [Dev56] S. Devons et al., Proc. Phys. Soc. **A69**, 173 (1956).
- [Dwo70] P. B. Dworkin et al., Bull. Amer. Phys. Soc. **12**, 15 (1970).
- [Dwo72] P. B. Dworkin and A. E. Litherland, Bull. Amer. Phys. Soc. **17**, 532 (1972).
- [Dwo74] P. B. Dworkin-Charlesworth, Ph.D. thesis, University of Toronto (unpublished), 1974.
- [End67] P. M. Endt and C. V. der Leun, Nucl. Phys. **A105** (1967).
- [End78] P. M. Endt and C. V. der Leun, Nucl. Phys. **A310**, 1 (1978).
- [End88] P. M. Endt, P. de. Wit, and C. Alderliesten, Nucl. Phys. **A476**, 333 (1988).

- [End90] P. M. Endt, Nucl. Phys. **A521**, 1 (1990).
- [End98] P. M. Endt, Nucl. Phys. **A633**, 1 (1998).
- [Fer65] A. J. Ferguson, *Angular Correlations in Gamma-Ray Spectroscopy*, North-Holland, Amsterdam, 1965.
- [Gie92] U. Giesen, Ph.D. thesis, University of Notre Dame, 1992.
- [Gov59] H. E. Gove, in *Nuclear Reactions I*, ed. P. M. Endt and M. Demeur, North-Holland, New York, 1959.
- [Ibe70] I. Iben, Sci. Amer., 114 (July 1970).
- [Ili90] C. Iliadis, T. Schange, C. Rolfs, U. Schroder, E. Somorjai, H. P. Trautvetter, K. Wolke, P. M. Endt, S. W. Kikstra, A. E. Champagne, M. Arnould, and G. Paulus, Nucl. Phys. **A512**, 509 (1990).
- [Ili97] C. Iliadis, Nucl. Phys. **A618**, 166 (1997).
- [Kei80] J. Keinonen and S. Brandenburg, Nucl. Phys. **A341**, 345 (1980).
- [Kei83] J. Keinonen, A. Luukkainen, A. Anttila, and M. Erola, Nucl. Instr. Meth. **216**, 249 (1983).
- [Kra88] K. S. Krane, *Introductory Nuclear Physics*, John Wiley and Sons, 1988.
- [Kra93] R. P. Kraft, C. Sneden, G. E. Langer, and M. D. Shetrone, Astron. J. **106**, 1490 (1993).
- [Kra94] R. P. Kraft, Pub. Astron. Soc. Pac. **106**, 553 (1994).
- [Lan93] G. E. Langer, R. Hoffman, and C. Sneden, Pub. Astron. Soc. Pac. **105**, 301 (1993).
- [Lan95] G. E. Langer and R. Hoffman, Pub. Astron. Soc. Pac. **107**, 1177 (1995).
- [Lan97] G. E. Langer, R. Hoffman, and C. Zaidens, Pub. Astron. Soc. Pac. **109**, 244 (1997).
- [Lit56] A. E. Litherland, E. B. Paul, G. A. Bartholomew, and H. E. Gove, Nucl. Phys. **102**, 208 (1956).
- [Lit58] A. E. Litherland, H. McManus, E. B. Paul, D. A. Bromley, and H. E. Gove, Can. J. Phys. **36**, 378 (1958).

- [Lyo69] P. B. Lyons et al., Nucl. Phys. **A130**, 1 (1969).
- [Maa78] J. W. Maas, A. J. C. D. Holvast, A. Baghus, H. J. M. Aarts, and P. M. Endt, Nucl. Phys. **A301**, 237 (1978).
- [Mar69] P. Marmier and E. Sheldon, *Physics of Nuclei and Particles*, Academic Press, 1969.
- [Max67] S. H. Maxman, Nucl. Instr. Meth. **50**, 53 (1967).
- [Meu75] F. Meurders and D. de Korte, Nucl. Phys. **A249**, 205 (1975).
- [Meu76] F. Meurders, P. W. M. Glaudemans, J. F. A. van Hienen, and G. A. Timmer, Z. Phys. **A276**, 113 (1976).
- [Mey75] M. A. Meyer, I. Venter, and D. Reitmann, Nucl. Phys. **A250**, 235 (1975).
- [Moh93] P. Mohr, H. Abele, R. Zwiebel, and G. Staudt, Phys. Rev. C **48**, 1420 (1993).
- [Mug79] A. H. F. Muggleton, J. Phys. E. Sci. Instrum. **12**, 780 (1979).
- [Nel85] W. R. Nelson, H. Hirayama, and D. W. G. Rodgers, *The EGS4 Code System*, SLAC-Report-265, 1985.
- [Pai79] B. M. Paine and D. G. Sargood, Nucl. Phys. **A331**, 389 (1979).
- [Pet75] R. J. Peterson and R. A. Ristinen, Nucl. Phys. **A246**, 402 (1975).
- [Pii72] M. Piiparinen, Z. Phys. **252**, 206 (1972).
- [Pow98] D. C. Powell, C. Iliadis, A. E. Champagne, S. E. Hale, V. Y. Hansper, R. A. Surman, and K. D. Veal, Nucl. Phys. **A644**, 263 (1998).
- [Rad89] D. C. Radford, *GELIFT Reference Manual*, Argonne National Laboratory, 1989.
- [Ree69] R. J. van Reenen et al., Z. Phys. **227**, 326 (1969).
- [Rol73] C. Rolfs, Nucl. Phys. **A217**, 29 (1973).
- [Rol74] C. Rolfs and H. Winkler, Phys. Lett. **52B**, 317 (1974).
- [Rol88] C. E. Rolfs and W. S. Rodney, *Cauldrons in the Cosmos*, University of Chicago Press, 1988.

- [Ros53] M. E. Rose, *Phys. Rev.* **91**, 610 (1953).
- [Rud88] I. R. V. Rudloff et al., *Astrophys. J.* **324**, 840 (1988).
- [Sar82] D. G. Sargood, *Phys. Rep.* **93**, 61 (1982).
- [Seu88] S. Seuthe, H. W. Becker, C. Rolfs, S. Schmidt, H. P. Trautvetter, R. W. Kavanagh, and F. B. Waanders, *Nucl. Instr. Meth.* **A272**, 814 (1988).
- [She96] M. D. Shetrone, *Astron. J.* **112**, 2639 (1996).
- [Smi82] J. J. A. Smit et al., *Nucl. Phys.* **A377**, 15 (1982).
- [Smi96] G. H. Smith and R. P. Kraft, *Pub. Astron. Soc. Pac.* **108**, 344 (1996).
- [Sod87] J. P. Soderstrum, M. A. Boyd, C. R. Gould, and N. R. Roberson, *XSYS Reference Manual*, Triangle Universities Nuclear Laboratory, Durham, NC, sixth edition, 1987.
- [Swe79] A. V. Sweigart and J. G. Mengel, *Astrophys. J.* **229**, 624 (1979).
- [Tak66] S. Takayanagi, M. Katsuta, K. Katori, and R. Chiba, *Nucl. Instr. Meth.* **45**, 345 (1966).
- [Ter93] A. Terakawa et al., *Phys. Rev. C* **48**, No. 6, 2775 (1993).
- [Tik91] P. Tikkanen, J. Keinonen, A. Kangasmaki, Z. Fulop, A. Z. Kiss, and E. Somorjai, *Phys. Rev. C* **43**, No. 5, 2162 (1991).
- [Tra75a] H. P. Trautvetter and C. Rolfs, *Nucl. Phys.* **A242**, 519 (1975).
- [Tra75b] H. P. Trautvetter, *Nucl. Phys.* **A243**, 37 (1975).
- [Uhr85] M. Uhrmacher, K. Pampus, F. J. Bergmeister, D. Purschke, and K. P. Lieb, *Nucl. Instr. Meth.* **B9**, 234 (1985).
- [Van41] J. A. V. Allen and N. M. Smith, *Phys. Rev.* **59**, 501 (1941).
- [Wan88] G. Wang, E. K. Warburton, and D. E. Alburger, *Nucl. Instr. Meth.* **A272**, 791 (1988).
- [Wes87] C. R. Westerfeldt et al., *The TUNL High Resolution Laboratory System and Operating Procedures*, Triangle Universities Nuclear Laboratory, Durham, NC second edition, 1987.
- [Wes88] C. R. Westerfeldt, R. O. Nelson, E. G. Bilpach, and G. E. Mitchell, *Nucl. Instr. Meth.* **A270**, 467 (1988).

- [Zai97] C. S. Zaidins and G. E. Langer, *Pub. Astron. Soc. Pac.* **109**, 252 (1997).
- [Zie80] J. Ziegler, *The Stopping and Range of Ions in Matter*, vol 2-6, Pergamon Press, 1977-1980.